Identification of hadronic τ decays using the τ lepton flight path and reconstruction and identification of jets with a low transverse energy at intermediate luminosities with an application to the search for the Higgs boson in vector boson fusion with the ATLAS experiment at the LHC

Dissertation
zur
Erlangung des Doktorgrades (Dr. rer. nat.)
der
Mathematisch-Naturwissenschaftlichen Fakultät
der
Rheinischen Friedrich-Wilhelms-Universität Bonn

vorgelegt von
Christoph Ruwiedel
aus
Bonn

Bonn 2010

Angefertigt mit Genehmigung der Mathematisch-Naturwissenschaftlichen Fakultät der Rheinischen Friedrich-Wilhelms-Universität Bonn

1. Gutachter:	Prof. Dr. N. Wermes
2. Gutachter:	Prof. Dr. H. Ströher
Tag der Promotion:	22.6.2010
Erscheinungsjahr:	2010

Contents

Introduction

The Large Hadron Collider (LHC) at CERN[1] has been operated for a short period of time in 2008 during which no controlled proton-proton collisions have taken place. Operation has resumed after a year-long shutdown with first collisions in November 2009. The LHC will allow the exploration of an energy scale that is expected to yield insight into the electroweak symmetry breaking of the Standard Model of particle physics. Despite detailed searches at earlier particle colliders such as LEP[2] and the Tevatron, no direct evidence of the mechanism that may explain electroweak symmetry breaking has yet been found.

The prospects for the search for the Standard Model Higgs boson in the vector boson fusion process at small and intermediate Higgs boson masses with the ATLAS experiment using a fast simulation of the detector were studied and summarized in [1]. Recently, the estimates have been updated using a detailed simulation of the detector [2]. The results indicate that a discovery of the Standard Model Higgs boson with a mass close to the LEP limit produced in vector boson fusion and decaying into a $\tau^+\tau^-$ lepton pair will be possible with an integrated luminosity of approximately $30\,\mathrm{fb}^{-1}$. The data will be taken during the initial years of operation when the luminosity will be increased gradually to the nominal value.

The lepton-hadron final state has a larger branching ratio than the lepton-lepton final state and was found to have a larger expected signal significance. The analysis in the lepton-hadron mode requires the identification of the hadronic τ lepton decay. At the LHC, τ leptons in Standard Model weak boson production processes are expected to have an average transverse flight distance of approximately 2 mm. This flight distance allows the reconstruction of the impact parameter in 1-prong τ decays and of the transverse flight distance in multi-prong τ decays. In chapter 3, a study of the performance of the ATLAS Inner Detector for the reconstruction of those observables and the expected increase of the rejection of light jets is presented.

The operation of the LHC has started at a low luminosity and center of mass energy. Both the center of mass energy and the luminosity will be increased over time with the aim to achieve 14 TeV and 10^{34} cm^{-2} s^{-1} after several years. At the nominal luminosity, approximately 23 minimum bias interactions are expected to take place on average in each bunch crossing. The dataset that will allow the first discovery of a Standard Model Higgs boson with a small mass in the vector boson fusion process will be composed of data taken at different luminosities and with varying numbers of additional minimum bias interactions superimposed on the triggered event. The effects of these additional interactions taking place close in time to the triggered event, which are commonly referred to as pileup, have not been taken into account in previous estimates of the signal significance.

In the vector boson fusion analysis, a veto against jets in the central region of the detector is applied. This central jet veto is one of several elements of the vector boson fusion analysis sensitive to pileup from additional minimum bias interactions. In the presence of pileup, jets not originating from the primary proton-proton interaction are reconstructed in the calorimeter which leads to a reduced efficiency of the jet veto. A method for associating jets reconstructed in the central detector region with the primary vertex of the primary proton-proton interaction is described in chapter 4. The method is used to remove jets that

[1] Conseil Europèen pour la Recherche Nuclèaire, European Laboratory for Particle Physics near Geneva, Switzerland

[2] Large electron positron collider

are not part of the primary interaction before applying the central jet veto.

In the design of the ATLAS calorimeter, pileup has been taken into account in a way that minimizes the dependence of the average cell energy in randomly triggered events on the luminosity. The intrinsic pileup cancellation that ensures vanishing average cell energies independent of the luminosity is incomplete for a bunch spacing different from the nominal bunch spacing. In such configurations, a bias is observed in some regions of the calorimeter or the whole calorimeter depending on the configuration. An additional bias is introduced by the cluster formation. These effects are discussed in chapter 5 and a modification of the clustering procedure that reduces the observed biases is presented and tested.

The physics background for the search for the Standard Model Higgs boson in the vector boson fusion process is briefly reviewed in chapter 1. An overview of the ATLAS detector is given in chapter 2. In chapter 3, the study of the impact parameter and transverse flight path reconstruction and their use for the identification of hadronic τ lepton decays is presented. The method developed for the jet-vertex association and its use for the central jet veto are detailed in chapter 4. The study of the effect of pileup on the calorimeter reconstruction and cluster formation is discussed in chapter 5.

Chapter 1

Theory

The current Standard Model of particle physics [3, 4] is a relativistic quantum field theory with interactions introduced by the requirement of local gauge invariance. The model describes spin 1/2 fermions and the interactions between them mediated by the spin 1 gauge bosons. The gauge symmetry is broken spontaneously by the introduction of a scalar field called the Higgs field.

The fermion content of the Standard Model is listed in table 1.1. There are two categories of fermions, quarks and leptons. The particles are arranged in 3 generations with each generation of particles having identical properties except for their interactions with the Higgs field.

The gauge group of the Standard Model is $SU(3) \times SU(2) \times U(1)$. It describes three of the four known fundamental forces, the strong interaction, the electromagnetic interaction and the weak interaction. Gravity is not yet included in the model. At the energies studied at current particle collider experiments gravity is weak and has no effect on experimental observations.

The theory of the $SU(3)$ part of the gauge group describes the strong interaction and is called quantum chromodynamics. It contains 8 gauge bosons called gluons. Quarks transform under the fundamental 3 representation, antiquarks under the fundamental $\bar{3}$ representation of $SU(3)$. Leptons do not interact strongly.

The $SU(2) \times U(1)$ part of the gauge group describes the electroweak interaction [5, 6, 7]. The $SU(2)$ and $U(1)$ quantum numbers are called weak isospin and weak hypercharge, respectively. Left-handed and right-handed particles have different electroweak quantum numbers. In particular, only left-handed particles interact via the $SU(2)$ gauge bosons. Left-handed particles are assigned to weak isospin

	Generation			
	1	2	3	Charge
Leptons	$\begin{pmatrix} \nu_e \\ e \end{pmatrix}_L$	$\begin{pmatrix} \nu_\mu \\ \mu \end{pmatrix}_L$	$\begin{pmatrix} \nu_\tau \\ \tau \end{pmatrix}_L$	0 -1
	e_R	μ_R	τ_R	-1
Quarks	$\begin{pmatrix} u \\ d \end{pmatrix}_L$	$\begin{pmatrix} c \\ s \end{pmatrix}_L$	$\begin{pmatrix} t \\ b \end{pmatrix}_L$	$2/3$ $-1/3$
	u_R	c_R	t_R	$2/3$
	d_R	s_R	b_R	$-1/3$

Table 1.1: Fermion content of the Standard Model of particle physics. The particles are arranged in weak isospin multiplets. The indices R and L refer to the chirality of the particle.

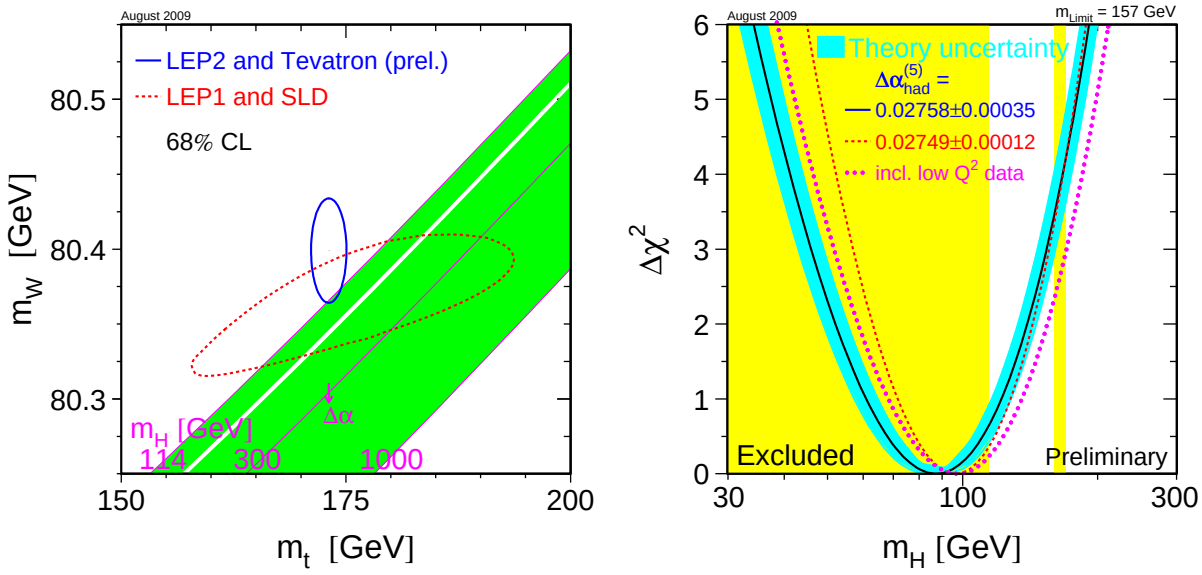

Figure 1.1: Contours at 68% confidence level in the plane spanned by the W boson and top quark masses and lines of constant Standard Model Higgs boson mass (*left*). Contours are shown for direct measurements at LEP2 and the Tevatron (*blue, solid line*) and for indirect measurements at LEP1 and SLC (*red, dashed line*). Direct exclusion limits for the Standard Model Higgs boson (*yellow areas*) and $\Delta\chi^2$ of a fit to electroweak precision observables as a function of the Higgs boson mass (*right*). [8]

doublets, right-handed particles to weak isospin singlets. The weak isospin 0 gauge boson of $SU(2)$ and the $U(1)$ gauge boson mix by the Weinberg angle θ_W to form the Z and the γ.

The electroweak symmetry is known to be broken since the weak bosons are observed to have non-zero masses. In the description of electroweak symmetry breaking adopted in the Standard Model a scalar weak isospin doublet field, the Higgs field, is introduced. The potential of the Higgs field is chosen in a way such that the vacuum state is not invariant under gauge transformations. The Lagrangian remains invariant under the full gauge group and the renormalizability of the theory is ensured, however the electroweak $SU(2) \times U(1)$ symmetry is broken spontaneously to the $U(1)$ symmetry of electromagnetism. The weak bosons $W^{\pm}$ and Z acquire a mass while the photon remains massless. Fermion mass terms are added to the Lagrangian by introducing interaction terms between the fermion fields and the Higgs field. After the symmetry breaking, the theory contains a single scalar boson, the Higgs boson. The Higgs boson couples to the fermions of the theory by coupling terms analogous to the mass terms and to the weak bosons with couplings in each case proportional to the mass of the fermion or gauge boson.

The description of electroweak symmetry breaking adopted in the Standard Model is not unique. The Higgs sector may be extended by additional fields and particles, as required by supersymmetric theories, or there may be no fundamental scalar fields, as in technicolor theories.

So far, no direct evidence of the electroweak symmetry breaking sector in the form of a discovery of a particle has been obtained. The search for the Standard Model Higgs boson at LEP has resulted in a lower limit for its mass of 114.4 GeV at 95% confidence level [8]. The mass range between 163 GeV and 166 GeV has been excluded at 95% confidence level by the Tevatron experiments CDF and D0 [9]. An estimate of the Standard Model Higgs boson mass can be obtained from measurements of electroweak

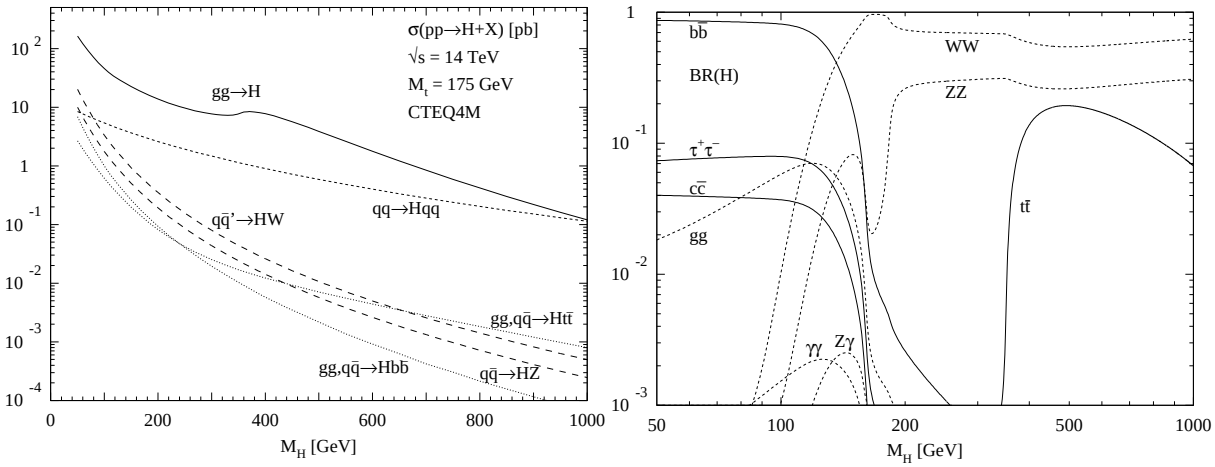

Figure 1.2: Cross section at NLO QCD for the production of a Standard Model Higgs boson in proton-proton collisions at $\sqrt{s} = 14$ TeV as a function of the Higgs boson mass (*left*) and branching ratios of the Standard Model Higgs boson as a function of the Higgs boson mass (*right*). The cross sections for the production of a Higgs boson in association with a $b\bar{b}$ or a $t\bar{t}$ quark pair are shown at LO. [10]

precision observables which are sensitive to the Higgs boson mass through loop corrections. Figure 1.1 shows contours at 68% confidence level in the plane spanned by the W boson and top quark masses and lines of constant mass of a Standard Model Higgs boson. A second plot shows the $\Delta\chi^2$ of a fit to electroweak precision measurements by the LEP experiments, SLD, CDF and D0. Both figures indicate a preference for small Higgs boson masses. From the fit, an upper limit at 95% confidence level for the mass of the Standard Model Higgs boson of 157 GeV is obtained. The upper limit from the fit is increased to 186 GeV if the lower limit from direct searches at LEP is taken into account.

1.1 Standard Model Higgs Boson Signatures at the LHC

Figure 1.2 shows the expected cross section for the production of a Standard Model Higgs boson in proton-proton collisions at a center of mass energy of 14 TeV. The process with the largest cross section is the fusion of two gluons to a Higgs boson. Since this is a QCD process it shows a jet activity similar to the most important background processes which are also QCD processes. The largest background rejection is obtained from the signature of the Higgs boson decay products. At large Higgs boson masses, the decay to a pair of Z bosons which allows the direct reconstruction of the Higgs boson mass dominates. The decay to a pair of W bosons has a larger branching ratio, as can be seen from the second plot in figure 1.2, however the Higgs boson mass cannot be directly reconstructed due the neutrinos in the final state. This decay channel nevertheless dominates the discovery potential around the WW pair production threshold. At small Higgs boson masses, the decay to a $\gamma\gamma$ pair has been studied. This decay has a clear signature if the invariant mass of the photon pair can be reconstructed with a good precision. The branching ratio for the decay is rather small, hence the large cross section of the gluon fusion process is needed for an observation in this channel.

The process with the second largest cross section is vector boson fusion in which the Higgs boson couples to a weak boson that is exchanged between two quarks. The two quarks acquire a significant transverse momentum and are typically scattered at relatively small angles to the beam direction. The resulting jets can be used to identify the event. Since no color is exchanged between the quarks, additional jet activity is expected only in the forward direction between the tagging jets and the beam. Due to the

small branching ratio, the decay to $\gamma\gamma$ is not significant in this process, however the jet signature allows the observation of a signal at small Higgs boson masses in the $\tau^+\tau^-$ final state. At larger Higgs boson masses the same decays into pairs of weak gauge bosons as for the gluon fusion process are the most promising ones.

At small Higgs boson masses, the production of a Standard Model Higgs boson in association with a $t\bar{t}$ quark pair has been studied. In this process, the decay to a $b\bar{b}$ quark pair is considered due to the large branching ratio. However, the hadronic Higgs boson decay and the small cross section make the identification of this process challenging and an observation is expected to require a larger dataset than for other processes. The production of a Higgs boson in association with a weak gauge boson, which was the dominant search mode at LEP, is also studied at small Higgs boson masses. Current results for the Higgs boson decaying to a $b\bar{b}$ pair indicate that this channel may contribute to a discovery at small Higgs boson masses [11].

Chapter 2

The ATLAS Experiment at the LHC

2.1 The LHC

The LHC [12] is a proton-proton collider designed for beams with a proton energy of 7 TeV and a center-of-mass energy of 14 TeV. It has been constructed in the 27 km long tunnel originally used for LEP. As in the case of LEP, the achievable beam energy is limited by the radius of the accelerator. However, unlike LEP which was a positron-electron collider the achievable beam energy in the LHC is limited mainly by the strength of the magnetic field of the bending magnets rather than by radiative energy losses. The LHC magnets are cooled using superfluid helium and operate in the superconducting state at a temperature of 1.9 K. Their magnetic field has a strength of 8.33 T at the nominal beam energy.

A nominal LHC fill consists of 2808 bunches. The nominal bunch spacing time is 25 ns. At the design luminosity of 10^{34} cm^{-2} s^{-1}, 23 inelastic proton-proton interactions are expected to take place on average in each bunch crossing. A large luminosity is required due to the small expected cross sections for typical signal processes. Pileup of several interactions per bunch crossings cannot easily be avoided due to the large range of cross sections from the order of a picobarn for Higgs boson production processes to approximately 60 mb for inelastic, non single diffractive proton-proton interactions. Pileup was one of the constraints that had to be taken into account in the design of the experiments at the LHC. In general, detectors must have a fast response and small readout time and a fine spatial granularity to keep the occupancy low. In addition, detectors and readout electronics, especially close to the interaction point, must be radiation hard.

Four large experiments have been constructed at the LHC. The experiments ALICE and LHCb are dedicated to the study of B-physics and heavy ion collisions, respectively. For the ALICE experiment the LHC will be operated as a lead ion collider. The other two large experiments, ATLAS [13] and CMS[1] [14], were designed as multi-purpose experiments. Both experiments contain a silicon pixel detector as the innermost part of the tracking system. The pixel detectors are enclosed by silicon strip detectors. The CMS silicon detector extends to the calorimeter while the ATLAS Inner Detector contains a third component, a straw tube detector with particle identification capability using transition radiation. The ATLAS calorimeter consists of a liquid argon (LAr) calorimeter at small radius and a plastic scintillator tile calorimeter at large radius. The electromagnetic calorimeter of CMS consists of lead tungstate crystals which in comparison with the ATLAS LAr calorimeter lack a longitudinal segmentation but have an excellent energy resolution. At larger radius a tile calorimeter is used also in CMS. Due to space constraints imposed by the CMS solenoid the thickness of the calorimeter is limited and a tail catcher had to be added outside the solenoid leading to a reduced precision of the energy measurement in the hadronic calorimeter compared to the ATLAS tile calorimeter.

[1] Compact muon solenoid

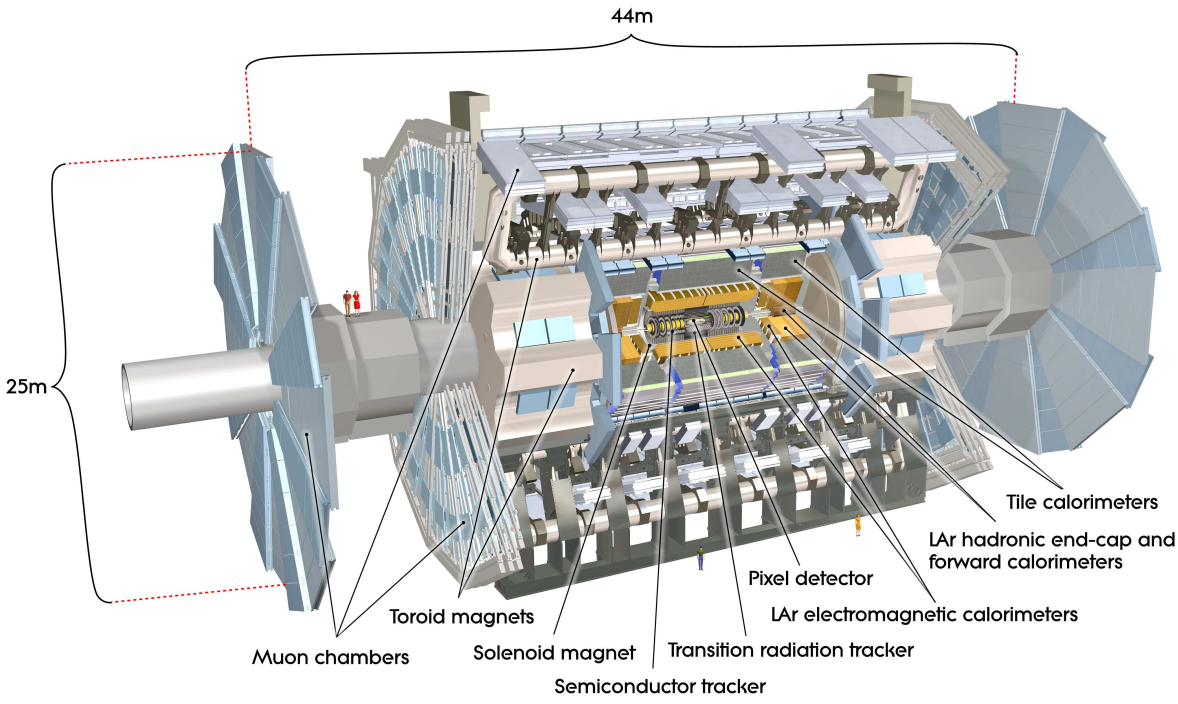

Figure 2.1: Cut-away view of the ATLAS detector. [13]

ATLAS has two separate magnet systems, a solenoid surrounding the Inner Detector and a large toroid for the muon spectrometer. CMS instead has a single large solenoid with a strong magnetic field that encloses the calorimeter and is used both for the inner tracking system and the muon system. This choice has led to a more compact design for CMS. The CMS solenoid is embedded in an iron return yoke instrumented with muon stations. In ATLAS the tile calorimeter serves as the return yoke for the solenoid. For the toroid no return yoke is needed and the ATLAS muon spectrometer covers a large volume with a relatively small amount of material.

2.2 The ATLAS Detector

Figure 2.1 shows a cut-away view of the ATLAS detector. The detector has a length of 44 m and a height of 25 m. The largest fraction of its volume is occupied by the muon spectrometer followed by the calorimeter and the Inner Detector at the center.

A right-handed coordinate system is used with the x axis pointing towards the center of the LHC ring. The y axis points upwards and the z axis is parallel to the beam at the interaction point with the direction defined by the right-handedness of the coordinate system. Coordinates are often expressed in a cylindrical system as the z coordinate, the radius r given by the distance from from the z axis and the pseudorapidity η. The pseudorapidity $\eta = -\ln\tan\left(\frac{\theta}{2}\right)$ is a measure of the angle θ with respect to the beam direction. For highly relativistic particles it is a good approximation for the rapidity in the z direction. Differences in the rapidity are invariant under boosts in the z direction and hence are well-defined physical observables at a hadron collider.

The components of the ATLAS detector are described in this chapter.

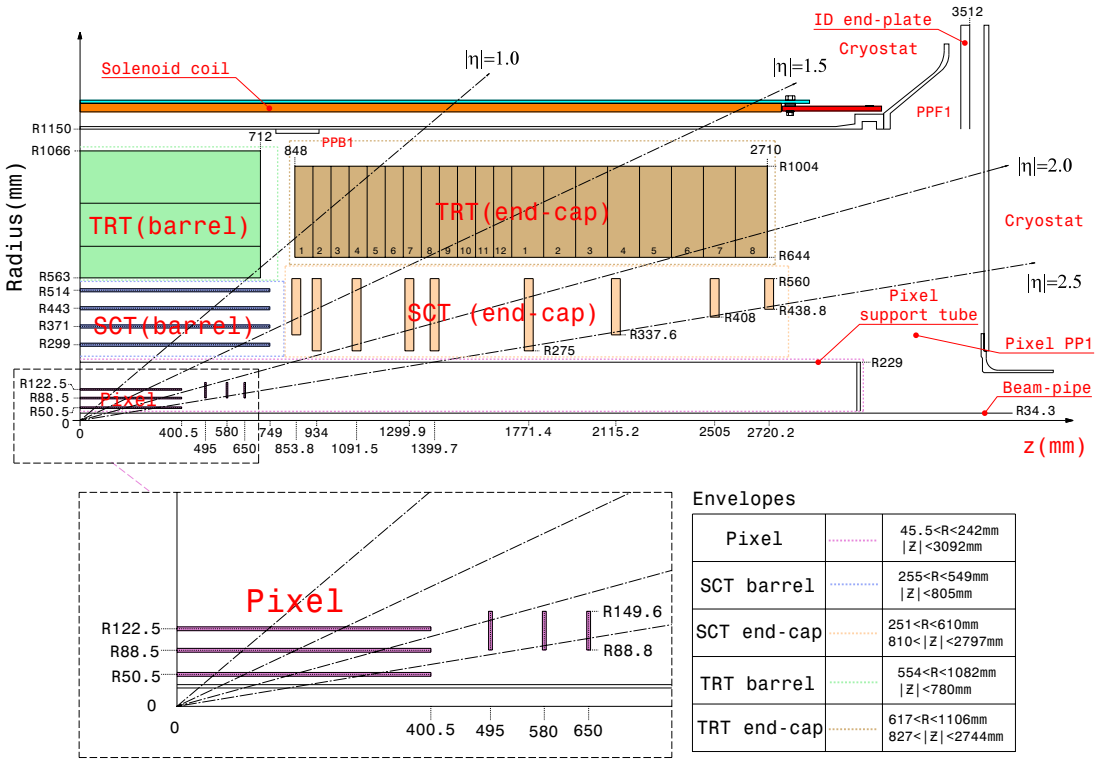

Figure 2.2: View of a section of the Inner Detector (*top*) and a magnified view of a section of the Pixel Detector (*bottom*) including dimensions and envelopes of the components. [13]

2.3 Inner Detector

The Inner Detector is composed of three different subsystems. A silicon pixel detector is used at the center of the Inner Detector detector to resolve tracks in the region of the largest particle density and to provide a precision measurement of the track origin in the interaction region. At larger radii a silicon strip detector provides further three-dimensional pattern recognition and precision measurements in the ϕ direction. Between the silicon detectors and the solenoid a straw-tube tracking detector with particle identification capability from transition radiation provides a large number of measurements in the ϕ direction. The Inner Detector provides track reconstruction capability in the range $|\eta| < 2.5$ with the transition radiation tracker covering approximately the range $|\eta| < 1.9$.

2.3.1 Pixel Detector

The innermost component of the ATLAS detector is a silicon pixel detector. The use of silicon pixel technology ensures an occupancy below 10^{-3} at the nominal luminosity and it allows the measurement of the z coordinate of tracks with sufficient precision to discriminate between tracks from the primary interaction and tracks from additional minimum bias interactions. Due to the small distance to the interaction region, the radiation level in the Pixel Detector will be high and achieving radiation hardness of the sensor and electronics was a significant challenge during the design of the detector.

The Pixel Detector has been constructed around the central section of the ATLAS beam pipe. The central section of the beam pipe has an inner radius of 29 mm and a thickness of 0.8 mm. It consists of beryllium to minimize the amount of material passed by the particles from the interaction region.

The layout of the Pixel Detector is is illustrated in figure 2.2. It consists of 3 barrel layers at average

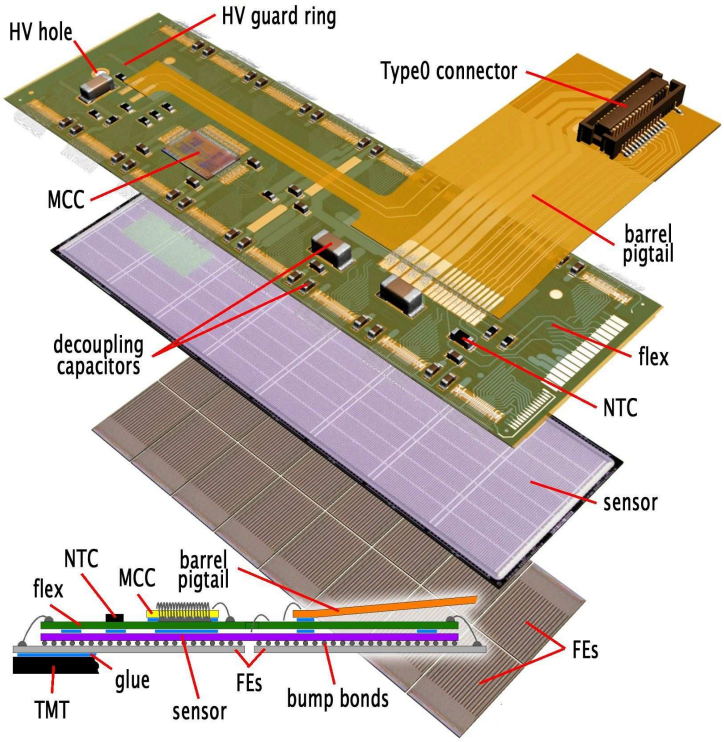

Figure 2.3: Structure of a module of the Pixel Detector. [13]

radii of 50.5 mm, 88.5 mm and 122.5 mm and two endcaps made of 3 disks each. The detector contains 1744 identical modules with 1456 modules in the barrel and 144 modules in each endcap. Each module consists of a silicon sensor connected by bump bonds to 16 front-end readout chips arranged in two rows. Each front-end chip has 2880 readout channels arranged in 18 columns and 160 rows. The nominal pixel size is $(50 \times 400)\,\mu\text{m}^2$ in the ϕ and z directions, respectively. To bridge the gap between front-end chips one column on each side of a front-end chip near the edge is connected to pixels with a size of $(50 \times 600)\,\mu\text{m}^2$. In the middle of a module where the two rows of front-end chips meet, each column of pixels contains 4 ganged pixels that are connected to the same readout channel as another pixel. Thus, each sensor has 47232 pixels and each module has 46080 readout channels. The Pixel Detector has approximately 80 million readout channels.

The noise in the Pixel Detector was found to be dominated by fixed pattern noise. After masking a fraction of approximately 0.02% of pixels showing a noise occupancy above 10^{-5} per read-out bunch crossing an occupancy from noise hits of approximately 10^{-10} was observed during a cosmics data taking period in autumn 2008. With a readout of one bunch crossing for each triggered event this occupancy corresponds to an average rate of 0.008 noise hits per event, making it negligible for the track reconstruction.

The front-end chips perform signal discrimination and provide a measurement of the deposited charge through the time-over-threshold. For pixel clusters with a size of at least 2 pixels the charge information can be used to improve the precision of the cluster position estimate.

The intrinsic measurement accuracies are $10\,\mu$m in the ϕ direction and $115\,\mu$m in the z direction.

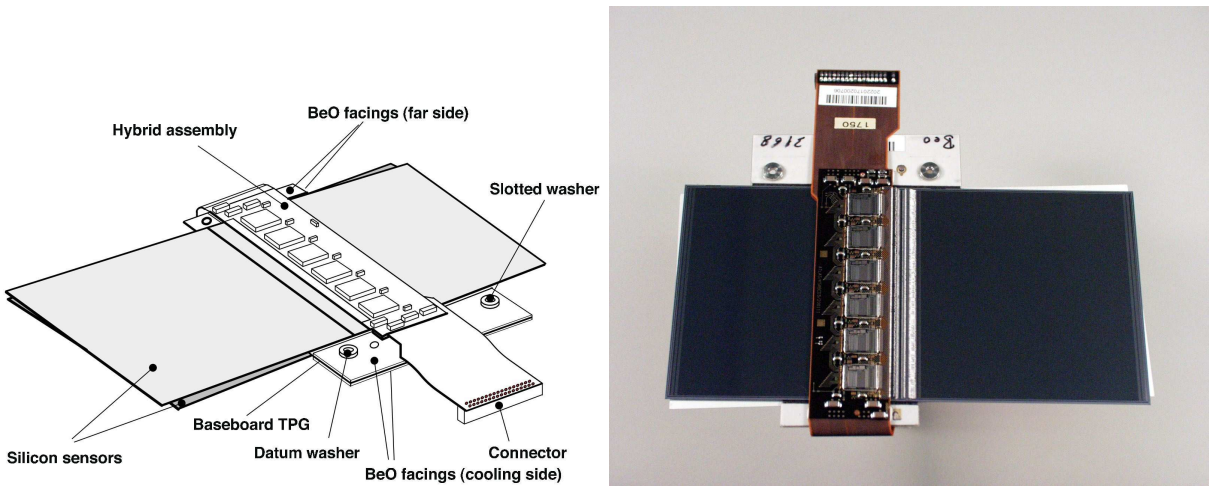

Figure 2.4: Drawing (*left*) and photograph (*right*) of a barrel module of the SCT. [13]

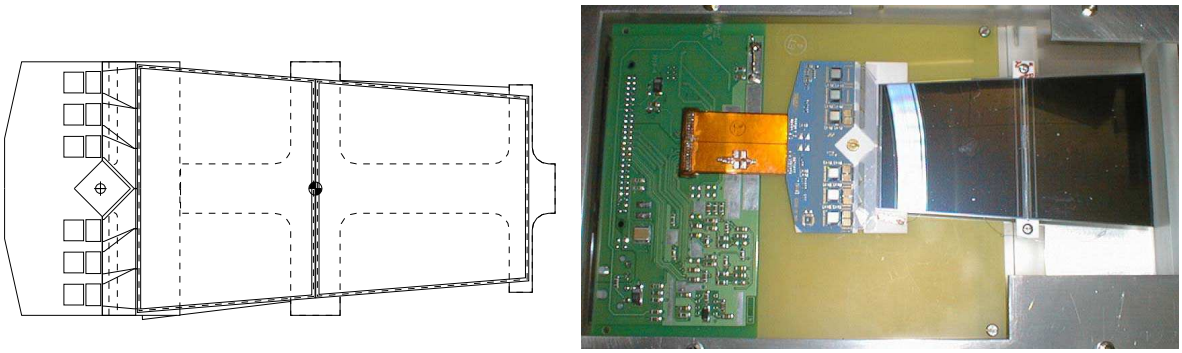

Figure 2.5: Drawing (*left*) and photograph (*right*) of an endcap module of the SCT [15].

2.3.2 Semiconductor Tracker (SCT)

The Semiconductor Tracker is a silicon strip detector located next to the Pixel Detector in the radial direction. The reduced charged particle density and radiation level in that region allow the use of silicon strips which have a coarser overall granularity while still providing an excellent measurement accuracy in the ϕ direction. The use of silicon strips rather than pixels allows to cover a large area at a reasonable cost and with acceptable requirements on the readout chain. The accuracy of the measurement of the z coordinate must be sufficient to allow an association of silicon strip hits to tracks with little ambiguity. In addition, it contributes to the precision of the η coordinate measurement at the calorimeter entrance since the transition radiation tracker provides no precision measurement of the η coordinate.

The SCT consists of 4 layers in the barrel region located at radii between 299 mm and 514 mm and of 2 endcaps with 9 disks each. The layout of the detector is shown in figure 2.2. The SCT modules in the barrel region and most modules in the endcaps consist of two pairs of silicon sensors mounted back-to-back with a stereo angle of 40 mrad. In the barrel region the sensors have a size of 6.40 cm $\times$ 6.36 cm. Each sensor contains 768 active strips with a strip pitch of 80 μm. On each side of a module two sensors are mounted with the strips connected in the middle of the module. Thus, each strip has a length of 12.8 cm. Figure 2.4 shows a barrel module of the SCT. The modules in the endcaps of the SCT have a trapezoidal shape. The strip pitch in those modules increases with the distance from the center of

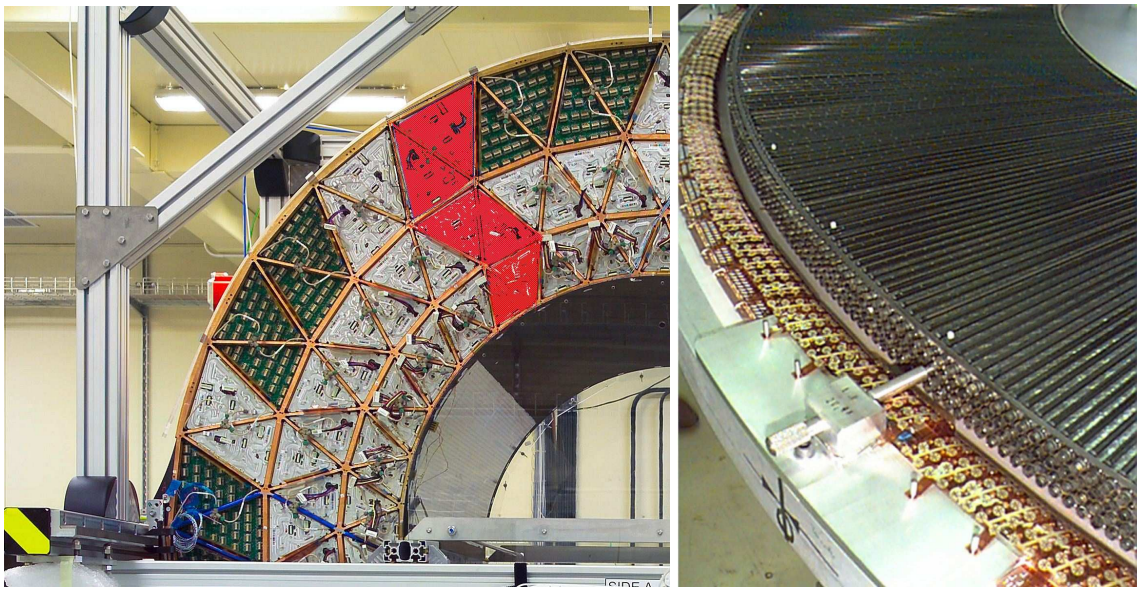

Figure 2.6: Photographs of a section of the TRT barrel (*left*) and of a section of the TRT endcap(*right*). [13]

the detector. Figure 2.5 shows an endcap module of the SCT. The SCT contains 4088 modules in total. It has approximately 6.3 million readout channels. The average noise occupancy is of the order $5 \cdot 10^{-5}$.

The readout of the SCT is binary and no information on the deposited charge is available. Clusters are created separately for each side of a module and the individual clusters are used for a track fit. For the pattern recognition, however, three-dimensional space points are formed using the information from both sides of a module [16].

The intrinsic accuracy in the ϕ direction is $17\,\mu$m. Due to the stereo angle an intrinsic accuracy in the z direction in the barrel and in the r direction in the endcaps of approximately 6 mm is achieved.

2.3.3 Transition Radiation Tracker (TRT)

The Transition Radiation Tracker is a straw tube tracking detector that surrounds the SCT in the radial direction. The detector consists of a barrel section with axially aligned straw tubes with a length of 144 cm and two endcap sections with radially aligned straw tubes with a length of 37 cm. The TRT covers a range of pseudorapidity of approximately $|\eta| < 1.9$. The detector was originally designed to extend to the full range of the Inner Detector of up to $|\eta| = 2.5$ [15], however the outer endcap segments are not present in the final layout. The layout of the detector is illustrated in figure 2.2. Photographs of a section of the barrel and a section of an endcap are shown in figure 2.6.

The detector contains approximately 300,000 straw tubes made of polyimide with gold-plated tungsten anode wires. The straw tubes have a diameter of 4 mm and are filled with a gas mixture of 70% Xenon, 27% CO_2 and 3% O_2. Each particle traverses approximately 36 straw tubes on average. The ambiguity of the sign of the distance between the track and the wire in the ϕ direction is resolved during the track reconstruction. The intrinsic accuracy using the drift time information and after ambiguity resolution in the ϕ direction is $130\,\mu$m. The TRT provides no precision measurement of the η coordinate, however limited information on the η coordinate is available from the z position of the last straw traversed in the endcaps. The noise occupancy is approximately 2%.

In the barrel region the straw tubes are embedded in polypropylene fibers used to induce transition

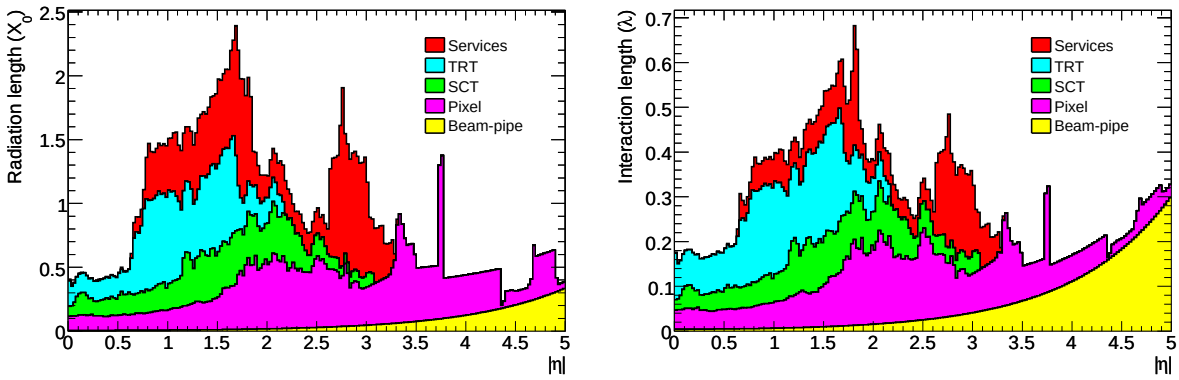

Figure 2.7: Material distribution of the Inner Detector as a function of $|\eta|$ expressed in radiation lengths (*left*) and in interaction lengths (*right*). [13]

radiation. In the endcaps individual layers of straw tubes are separated by polypropylene foils. CO_2 gas is circulated through the space between the straw tubes to avoid contamination from Xenon permeating the straw tube walls or exiting through possible leaks which would absorb the transition radiation. Transition radiation hits produce a larger signal on average and two different thresholds are used to differentiate between signals from minimum ionising particles and signals from transition radiation. For electrons with energies above 2 GeV between 7 and 10 high-threshold hits are expected.

2.3.4 Material Distribution in the Inner Detector

The distribution of material in the Inner Detector as a function of $|\eta|$ expressed in radiation and interaction lengths is shown in figure 2.7. The thickness of the Inner Detector material varies between approximately 0.5 radiation lengths in the central region and up to 2.4 radiation lengths in the endcaps.

2.3.5 Inner Detector Performance

The resolution of the inverse transverse momentum in the central region of the Inner Detector can be approximated by

$$\sigma\left(\frac{1}{p_T}\right) = 0.34 \text{ TeV}^{-1}\left(1 \oplus \frac{44 \text{ GeV}}{p_T}\right) \tag{2.1}$$

where the first term represents the geometric resolution of the detector and the second term represents the contribution from multiple scattering. The numerator of the second term indicates the p_T at which the two terms are equal. For particles with a transverse momentum of 100 GeV the transverse momentum resolution is approximately 3.8% at $\eta = 0$. At $\eta = 2.5$ a resolution of 11% is expected [17].

The resolution of the transverse impact parameter for tracks with $p_T = 100$ GeV is approximately $11\,\mu$m. The multiple scattering term is equal to the geometric term at transverse momenta between 14 GeV and 20 GeV depending on the angle with respect to the z axis. The resolution of the impact parameter in the z direction z_0 varies between approximately $90\,\mu$m in the central region and $190\,\mu$m in the forward direction. The multiple scattering term is equal to the geometric term for the z_0 measurement at transverse momenta between 2.3 GeV and 3.7 GeV.

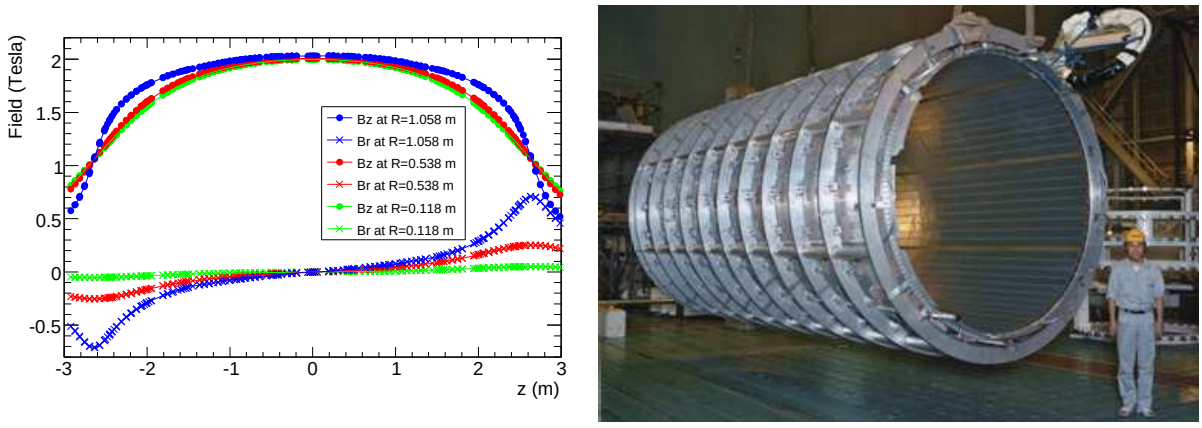

Figure 2.8: Strength of the radial and axial components of the magnetic field of the solenoid as a function of z (*left*) and a photograph of the solenoid (*right*). [13]

2.4 Solenoid

The superconducting solenoid that provides an axial magnetic field of 2 T to the Inner Detector is located between the TRT and the electromagnetic calorimeter. Due to its location inside the calorimeter it was designed to require a minimum amount of material. At normal incidence it constitutes approximately 0.66 radiation lengths. The magnetic flux is returned through the tile calorimeter and its girder support structure. The strength of the magnetic field in the axial and radial directions as a function of z and a photograph of the solenoid are shown in figure 2.8.

2.5 Calorimeter

The ATLAS calorimeter consists of a section at small radius in which liquid argon is used as the active material and a section at large radius in which plastic scintillator tiles are used as the active material. The calorimeter is divided into a presampler, an electromagnetic calorimeter and a hadronic calorimeter. The tile calorimeter constitutes the central part of the hadronic calorimeter. The endcaps of the liquid argon calorimeter consist of an electromagnetic endcap and a hadronic endcap each. The forward calorimeter which is located at small radius at the center of the calorimeter endcaps consists of one electromagnetic module and two hadronic modules on each side of the detector.

The different components of the liquid argon calorimeter are housed in three different cryostats, one for the barrel section and one for each endcap. The barrel cryostat contains the electromagnetic barrel calorimeter, the barrel presampler and the solenoid magnet. The endcap cryostats contain the endcap presampler, the electromagnetic endcap calorimeter, the hadronic endcap calorimeter at larger $|z|$ and the forward calorimeter at small radius. The structure of the calorimeter is illustrated in figure 2.9.

2.5.1 Electromagnetic Calorimeter

The barrel section of the liquid argon calorimeter and the electromagnetic endcap consist of lead absorber plates with a thickness between 1.1 mm and 2.2 mm interleaved with copper electrodes. In the barrel section a 2.1 mm gap on each side of the electrodes is filled with liquid argon. In the electromagnetic endcap the width of the liquid argon gap increases with the radius from 0.9 mm to 3.1 mm.

Both the absorbers and electrodes have an “accordion” shape as shown in figures 2.10 and 2.11. The plates are aligned along the axial and radial directions. The crests of the waves are aligned axially

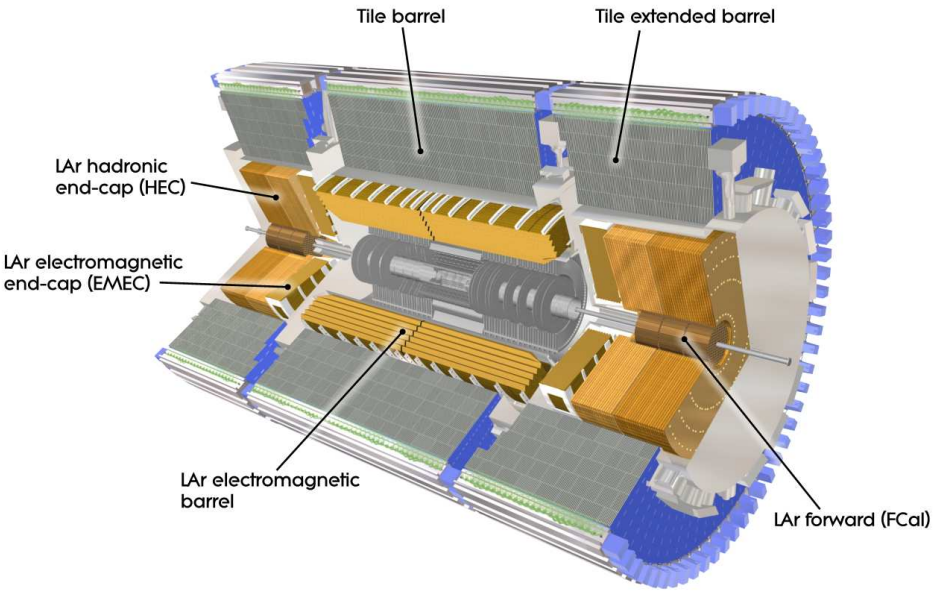

Figure 2.9: Cut-away view of the ATLAS calorimeter. [13]

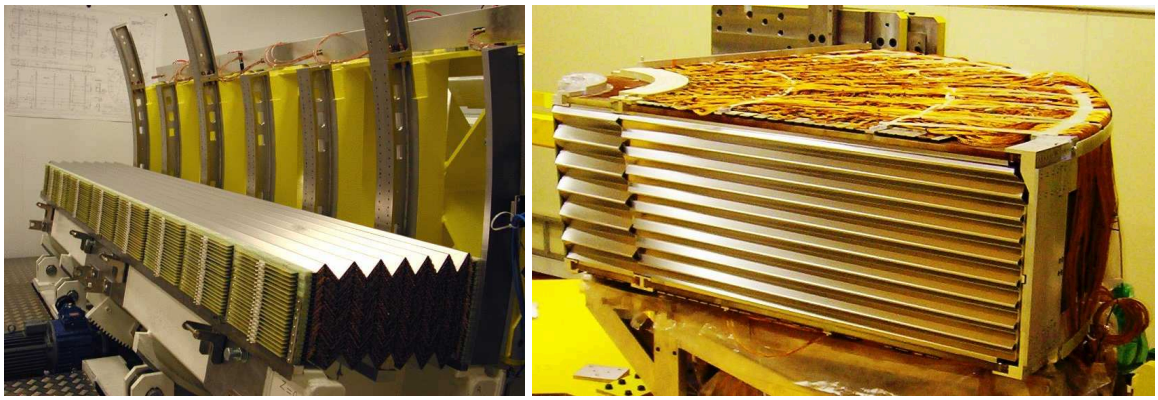

Figure 2.10: Photographs of sections of the electromagnetic barrel (*left*) and endcap (*right*) calorimeters. [13]

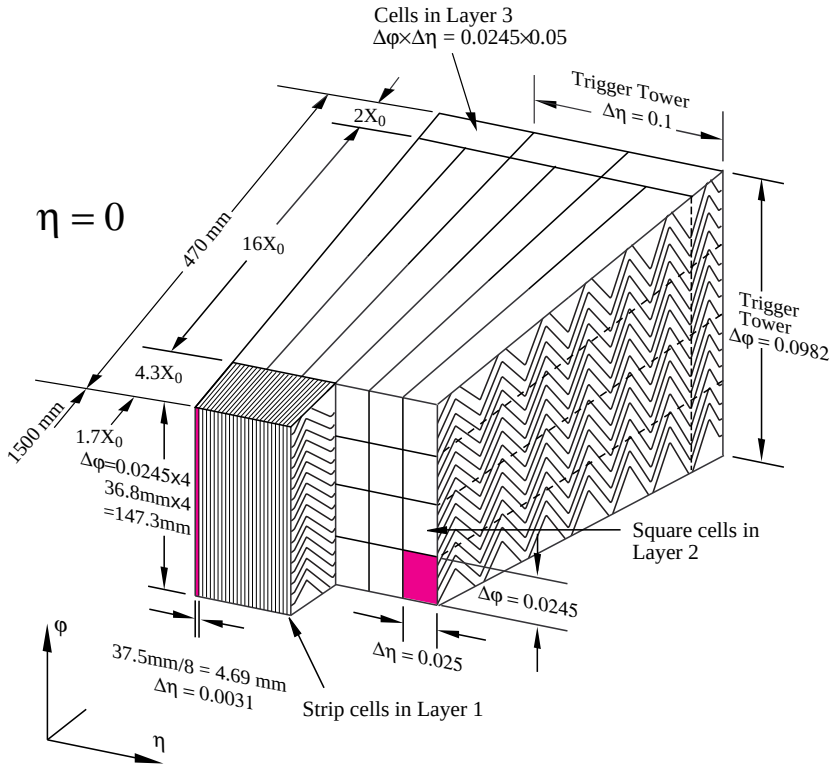

Figure 2.11: Drawing of a section of the electromagnetic barrel calorimeter. [13]

in the barrel section and radially in the endcaps. The barrel section of the calorimeter is segmented radially into a front, middle and back section as illustrated in figure 2.11. The endcaps consist of two concentric wheels separated at $|\eta| = 2.5$. The region between $|\eta| = 1.5$ and $|\eta| = 2.5$ of the outer wheels is segmented in the *z* direction into three sections as in the barrel. The outermost part of the outer wheel and the inner wheel are segmented into two sections in the *z* direction.

The segmentation of each section in ϕ is achieved by combining the output of several electrodes. The segmentation in η is achieved by etching of the electrodes. The segmentation is projective in η. The front layers of the barrel calorimeter and the endcaps in the region of the endcaps with three sections in the *z* direction have a fine segmentation in η to allow a separation between prompt photons and neutral pions. In the barrel region each cell has a width in η of $0.025/8$. The segmentation becomes coarser in the endcap with increasing $|\eta|$ to maintain a strip width of several mm.

The barrel and the endcaps in the region between $|\eta| = 1.5$ and $|\eta| = 1.8$ are covered by presamplers which consist of separate instrumented liquid argon layers. The presamplers provide a measurement of the showers that started in the Inner Detector and the solenoid. Their segmentation is relatively coarse compared to the front layer of the calorimeter.

Figure 2.12 shows the thickness of the electromagnetic calorimeter expressed in radiation lengths as a function of $|\eta|$. The thickness varies between approximately 25 and 40 radiation lengths.

2.5.2 Hadronic Endcap Calorimeter

The hadronic endcap calorimeter consists of two wheels in each endcap. Each wheel is segmented into two sections in the *z* direction. The wheels consist of wedge-shaped modules as shown in figure 2.13. Flat copper plates are used as the absorber. The copper plates have a thickness of 25 mm in the front

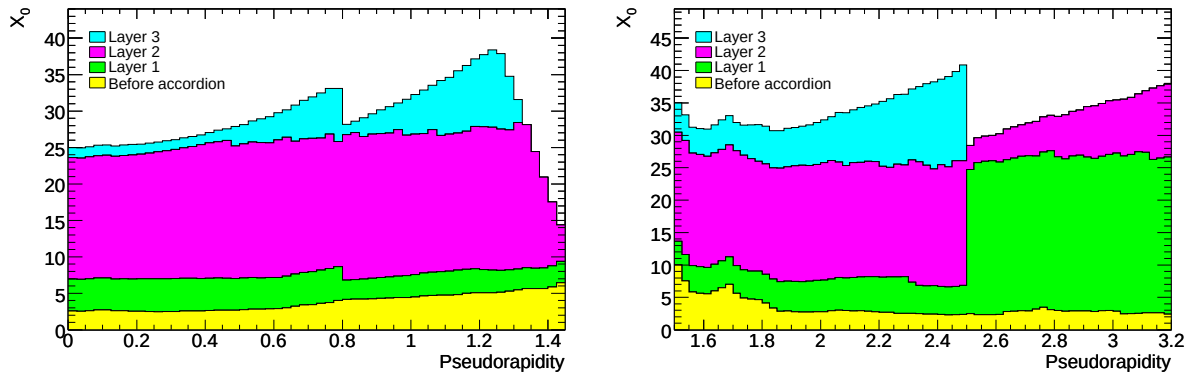

Figure 2.12: Thickness of the barrel (*left*) and the endcap (*right*) electromagnetic calorimeter expressed in radiation lengths as a function of $|\eta|$ [13]

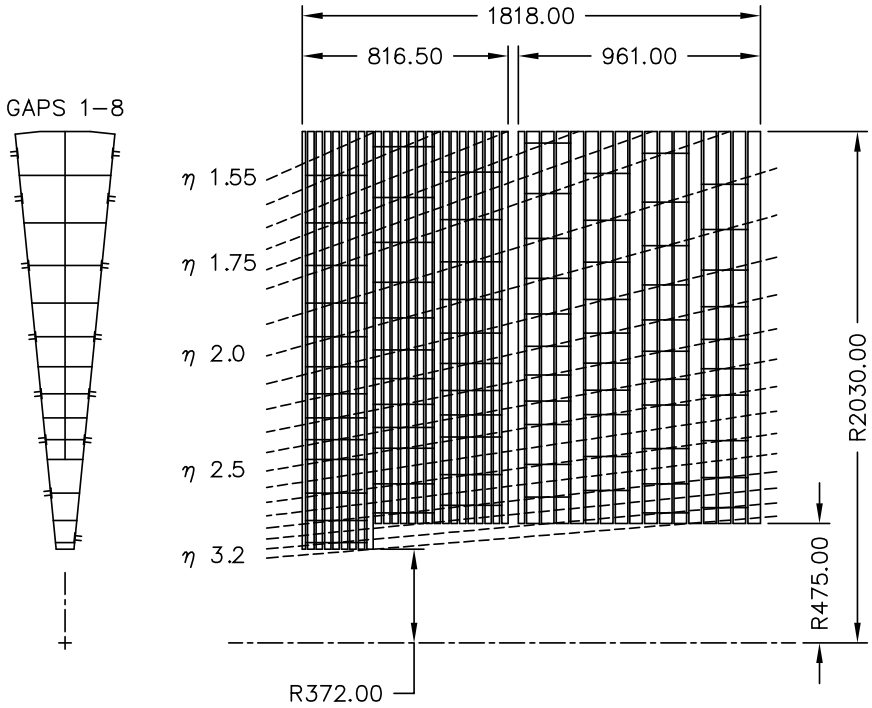

Figure 2.13: Drawings of a module of the hadronic endcap calorimeter (*left*) and of a cross-section of the hadronic endcap calorimeter in the *R*-*z* plane (*right*). [13]

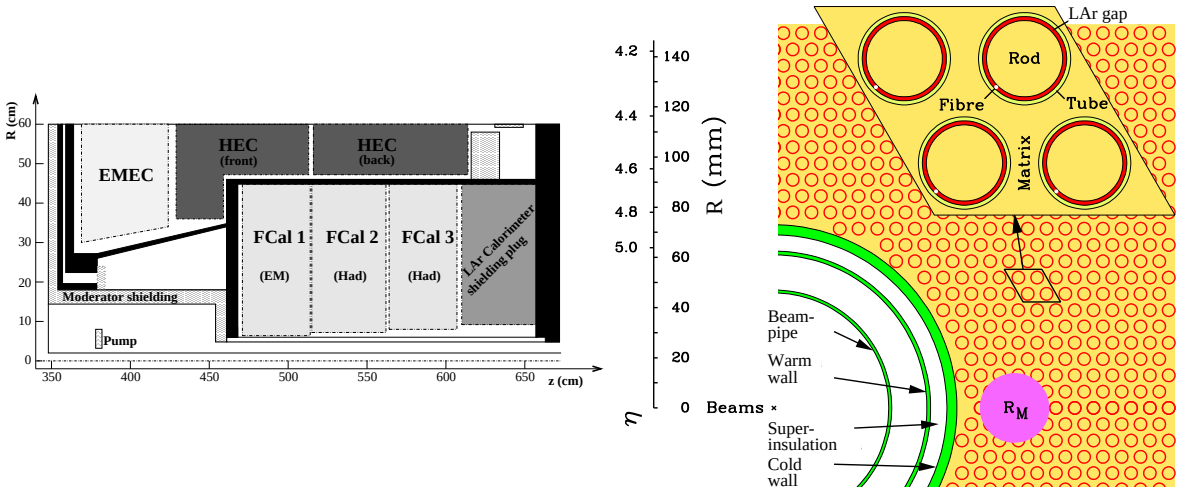

Figure 2.14: Layout and location of the forward calorimeter (*left*) and internal structure of the first module of the forward calorimeter (*right*). [13]

wheel and of 50 mm in the back wheel. Liquid argon gaps between the copper plates with a width of 8.5 mm are instrumented with copper electrodes. The gaps are subdivided by the electrodes into four separate volumes with a width of 1.8 mm each. The calorimeter is segmented in η and ϕ by etching of the electrodes. The segmentation is almost projective in η as shown in figure 2.13. The coarseness of the granularity increases with $|\eta|$ in a single step at $|\eta| = 2.5$.

2.5.3 Forward Calorimeter

The forward calorimeter consists of three modules in each endcap located between the beam pipe and the hadronic endcap calorimeter as shown in figure 2.14. The electrodes of the forward calorimeter consist of axially-aligned rods inserted in copper tubes with a gap between the rods and the tubes. The gap has a width of 0.269 mm, 0.376 mm and 0.508 mm in the first, second and third FCal module, respectively, and is filled with liquid argon. The rods in the first module of the forward calorimeter are made of copper. The tubes in the first module are embedded in a set of copper absorber plates with holes for the electrodes. In the second and third modules the rods and the absorber surrounding the tubes are made of tungsten.

The structure of the first FCal module is shown in figure 2.14. In the first, second and third module the signal from four, six and nine electrodes is combined for the readout, respectively.

2.5.4 Hadronic Barrel Calorimeter

The tile calorimeter consists of a barrel section surrounding the electromagnetic barrel calorimeter in the radial direction and two extended barrel sections surrounding the liquid argon endcap calorimeters. It is made of steel absorber interleaved with plastic scintillator tiles with the steel occupying approximately 82% of the volume. The structure of a tile calorimeter module is shown in figure 2.15. The light from the scintillator tiles is transported by readout fibers to photomultipliers located in the steel girder on the outside of the calorimeter. The calorimeter is segmented by combining the fibers from several tiles in a common photomultiplier. The segmentation is illustrated in 2.16. In the barrel section the segmentation is projective in η to a good approximation. In the extended barrel the approximation of a projective geometry is less accurate.

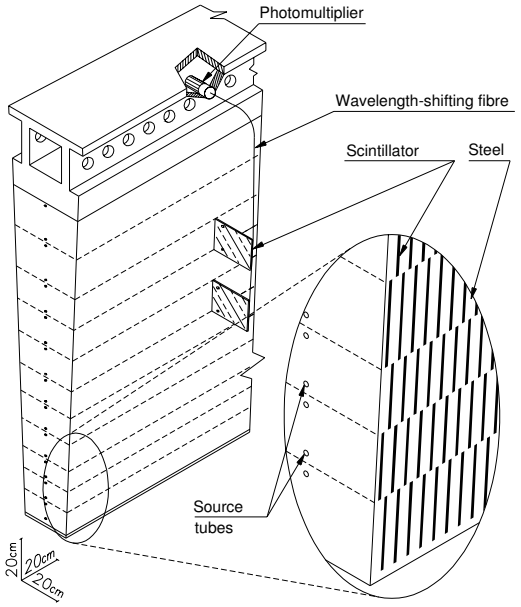

Figure 2.15: Structure of a module of the hadronic tile calorimeter. [13]

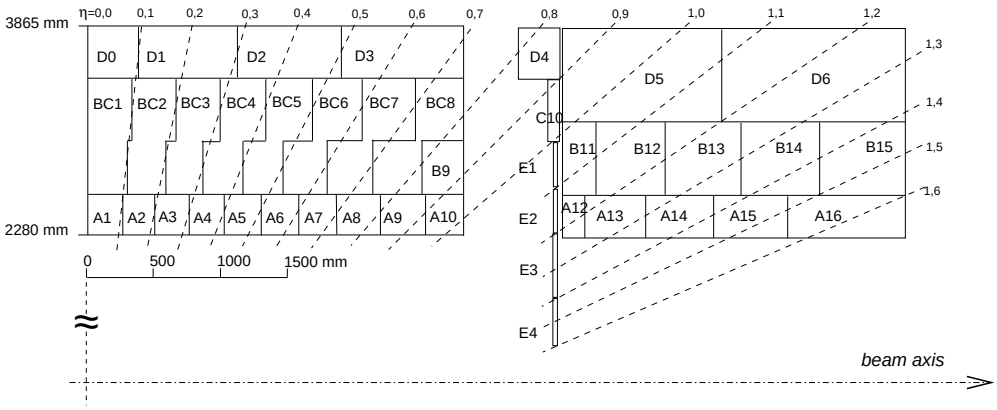

Figure 2.16: Segmentation of the tile calorimeter in r and η. [13]

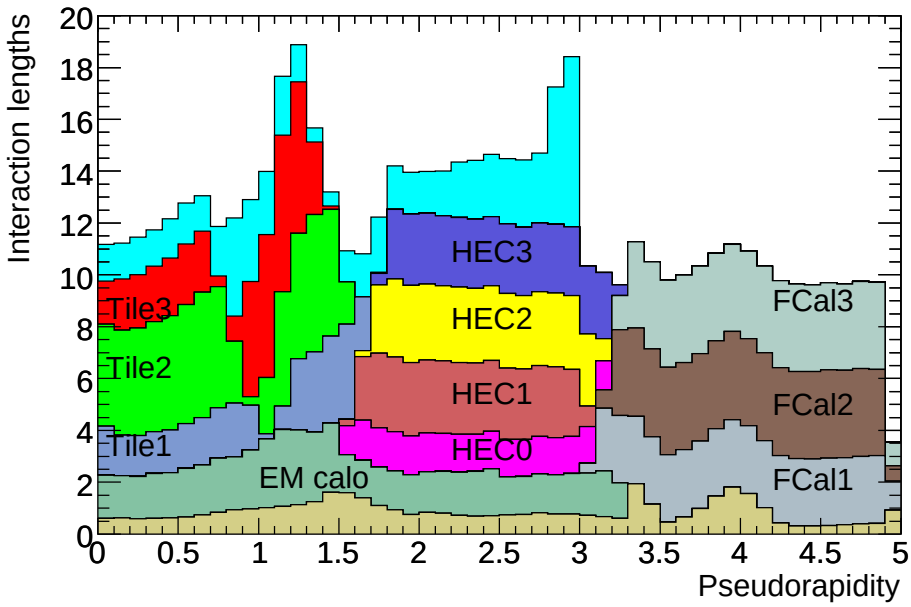

Figure 2.17: Thickness of the calorimeter expressed in hadronic interaction lengths as a function of $|\eta|$. [13]

The gap region between the barrel and the extended barrel sections is instrumented with a subsection of a standard tile calorimeter module, the plug calorimeter, and several scintillators.

Figure 2.17 shows the thickness of the calorimeter expressed in hadronic interaction lengths. The thickness of the hadronic calorimeter, excluding the transition regions, varies between approximately 8 and 14 interaction lengths.

2.5.5 Calorimeter performance

The energy resolution of the calorimeter can be expressed as

$$\frac{\sigma(E)}{E} = \frac{a}{\sqrt{E\,(\text{GeV})}} \oplus \frac{b}{E\,(\text{GeV})} \oplus c \tag{2.2}$$

where the first term is a stochastic term representing fluctuations of the shower development and the energy deposit in the absorber, the second term represents the contribution from noise and the third constant term arises from local non-uniformities of the calorimeter response.

In the central detector region stochastic and constant terms of $(10.1 \pm 0.4)\%\sqrt{\text{GeV}}$ and $(0.2 \pm 0.1)\%$, respectively, have been determined from electron testbeam data. For hadrons a stochastic term of $(52.0 \pm 1.0)\%\sqrt{\text{GeV}}$, a constant term of $(3.0 \pm 0.1)\%$ and a noise term of 1.6 GeV $\pm$ 0.1% have been observed.

In the forward calorimeter, stochastic and constant terms of $(28.5 \pm 1.0)\%\sqrt{\text{GeV}}$ and $(3.5 \pm 0.1)\%$, respectively, were measured for electrons. For pions stochastic and constant terms of $(94.2 \pm 1.6)\%\sqrt{\text{GeV}}$ and $(7.5 \pm 0.4)\%$, respectively, have been determined using a basic technique that does not take into account the structure of the energy deposits within the individual FCal modules.

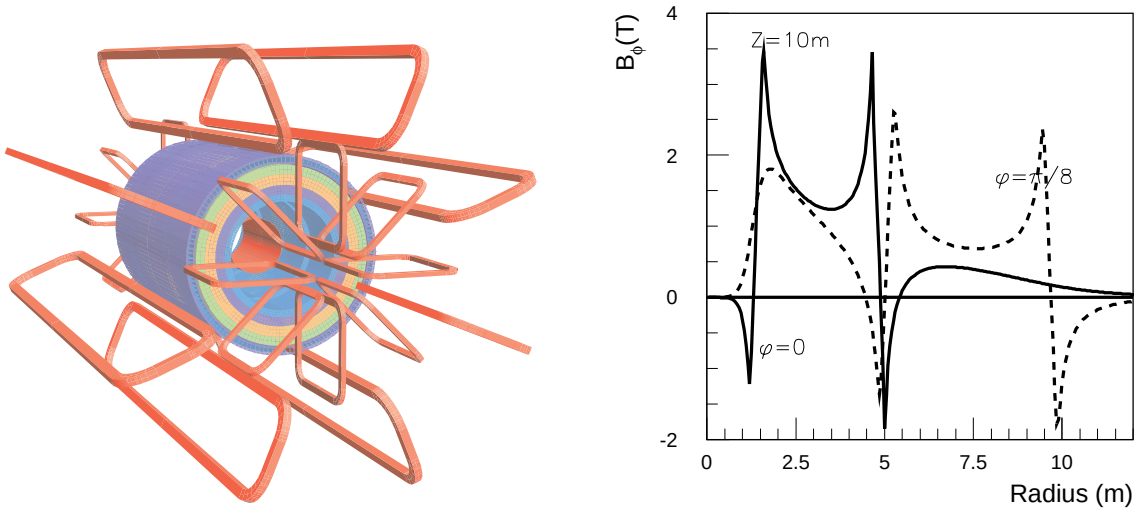

Figure 2.18: Layout of the ATLAS magnet system (*left*) and strength of the azimuthal magnetic field at $z = 10\,\text{m}$ in the plane of an endcap coil (*solid*) and in the plane of a barrel coil (*dotted*). [13, 18]

2.6 Toroid Magnet

The magnetic field for the ATLAS muon spectrometer is provided by a system of superconducting air-core toroid magnets. The system consists of 2 endcaps with 8 magnets each and a barrel part with 8 magnets surrounding the calorimeter and the endcap toroids in the radial direction. The layout of the system is illustrated in figure 2.18. The barrel magnets are contained in individual cryostats. The endcap magnets are contained in a common cryostat for each endcap. The strength of the magnetic field varies between 0.15 T and 2.5 T depending on the location. The azimuthal component of the magnetic field as a function of the radius is shown in figure 2.18.

2.7 Muon Spectrometer

The muon spectrometer consists of a combination of precision tracking chambers and trigger chambers. The chambers are arranged in a barrel section in 3 layers at approximately 5 m, 7.5 m and 10 m radius and in two endcaps. The chambers in the barrel section and the endcap wheels are arranged in 8 sectors matching the toroid magnets. In each layer or disk 8 large chambers are placed between the magnets in the azimuthal direction and 8 smaller chambers are placed at the azimuth of the magnet either outside or inside the magnet with a small overlap with the large chambers. The layout of the muon spectrometer is shown in figure 2.19.

Monitored drift tube (MDT) chambers are used as precision tracking chambers over the full coverage of the muon spectrometer of $|\eta| < 2.7$ except for the region $|\eta| > 2.0$ of the innermost disks of the endcaps which is instrumented with cathode strip chambers (CSC). Gaps are present in the central region at $\eta = 0$ for services to the solenoid, the calorimeter and the Inner Detector and in the region of the ATLAS support structure. The drift tubes of the monitored drift tube chambers have a diameter of approximately 30 mm. They are filled with a mixture of argon and CO_2 at a pressure of 3 bar. Tungsten-rhenium wires are used as the anodes. The maximum drift time is 700 ns which corresponds to 28 bunch crossings at the nominal bunch spacing. In each MDT module the drift tubes are arranged in two sheets of 4 layers each in the innermost section of the muon spectrometer and of 3 layers each in the middle and outer sections. The sheets are separated by a spacer structure as shown in figure 2.20. The drift tubes are

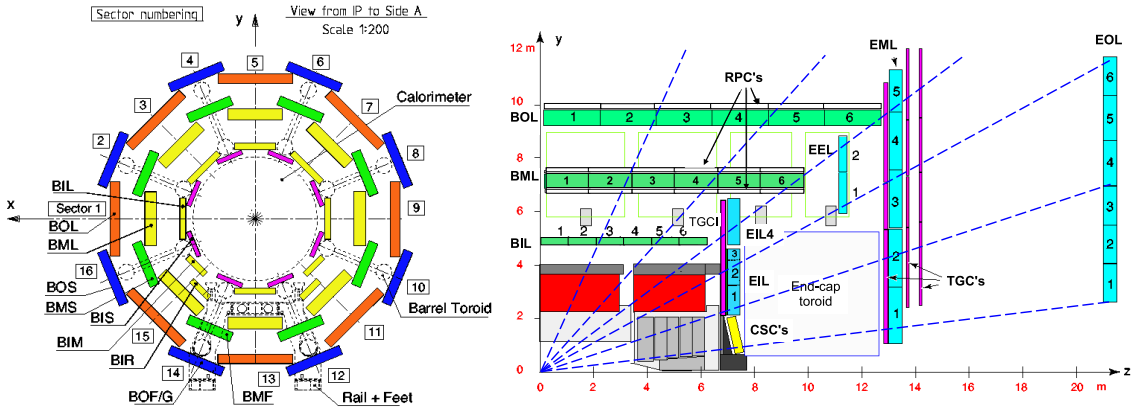

Figure 2.19: Layout of the muon spectrometer barrel (*left*) and drawing of a sector of the muon spectrometer in the *r-z* plane (*right)*. [13]

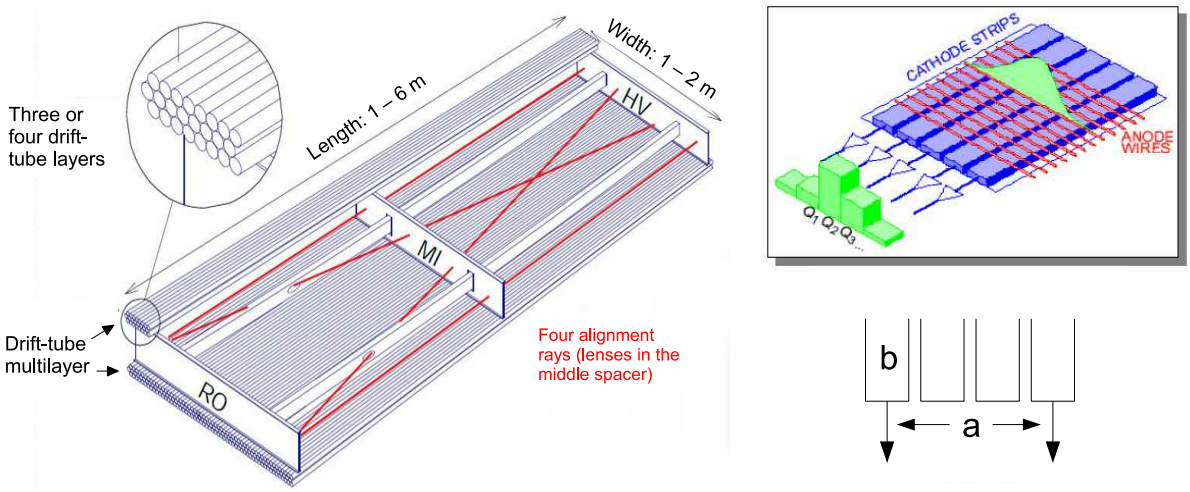

Figure 2.20: Layout of an MDT chamber with 3 layers (*left*) and illustration of the readout of the precision coordinate of the cathode strip chambers (*right*). [13]

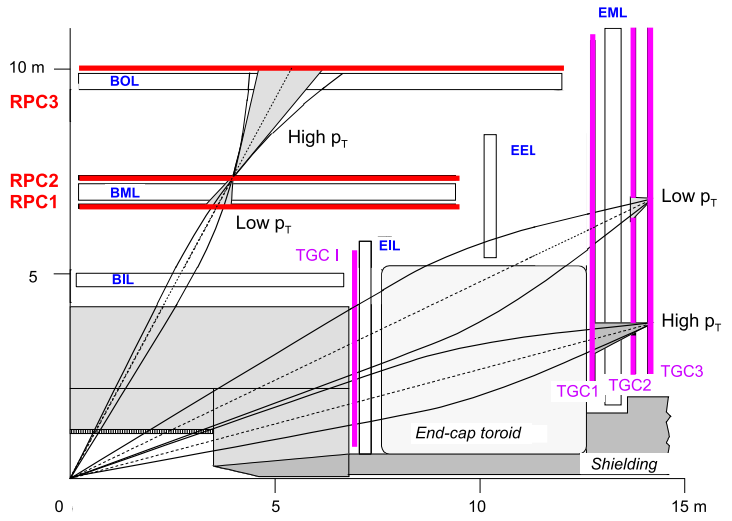

Figure 2.21: Layout of the muon trigger chambers and illustration of the angular acceptance for different transverse momentum thresholds of the level 1 trigger. [13]

aligned in the azimuthal direction and provide a precision measurement in the η direction orthogonal to the bending plane of the toroid magnets. The intrinsic precision of the measurement in chambers with 6 (8) tubes is $35\,\mu$m ($30\,\mu$m). The measurement of the ϕ coordinate is provided by the trigger chambers.

Cathode strip chambers are multiwire proportional chambers. They are used in the innermost section of the inner wheel due to their capability to operate at the high rates expected in that region. The wires are aligned radially. One cathode providing the precision measurement in the η direction is segmented into strips orthogonal to the wires. The other cathode is segmented into strips parallel to the wires. The precision coordinate is determined from the distribution of the measured charge deposition along the wire direction as illustrated in figure 2.20. Cathode strip chambers consist of 4 layers of wires and readout electrodes. The precision of the measurement of the r coordinate is $40\,\mu$m.

In the barrel section of the muon spectrometer, resistive plate chambers (RPC) are used as trigger chambers. Each chamber consists of two independent pairs of parallel plates instrumented with readout strips and a 2 mm gap filled with gas. The chambers operate at a high voltage in the avalanche mode with a signal width of 5 ns. The RPC modules are mounted in a common support structure with the MDT modules. The middle MDT layer is instrumented with two RPC modules and the outer MDT layer with one. The transverse momentum of the muons is estimated for the level 1 trigger from the angle of the track segment reconstructed in two chambers with respect to the line from one of the chambers to the interaction point. The transverse momentum thresholds are defined as the corresponding widths of coincidence windows. Three low thresholds are defined between the inner and middle RPC layers and three high thresholds are defined between the middle and outer layers. The layout of the trigger chambers and the principle of the determination of p_T thresholds are illustrated in figure 2.21.

In the forward region, thin gap chambers (TGC) are used as the trigger chambers. The chambers are multi-wire chambers with a wire pitch of 1.8 mm and a width of the gas gap of 2.8 mm. They are operated in a quasi-saturated mode with a gas gain of approximately 3×10^5 with a 99% efficiency of observing a signal in a 25 ns window. In the forward region, coincidence windows are defined between the TGC layers of the big wheels outside the endcap toroid as shown in figure 2.21. As in the barrel, three high-p_T thresholds and three low-p_T thresholds are defined. The position of a hit in the η direction is determined from the anode wire signal. The wires are aligned azimuthally and read out in groups of

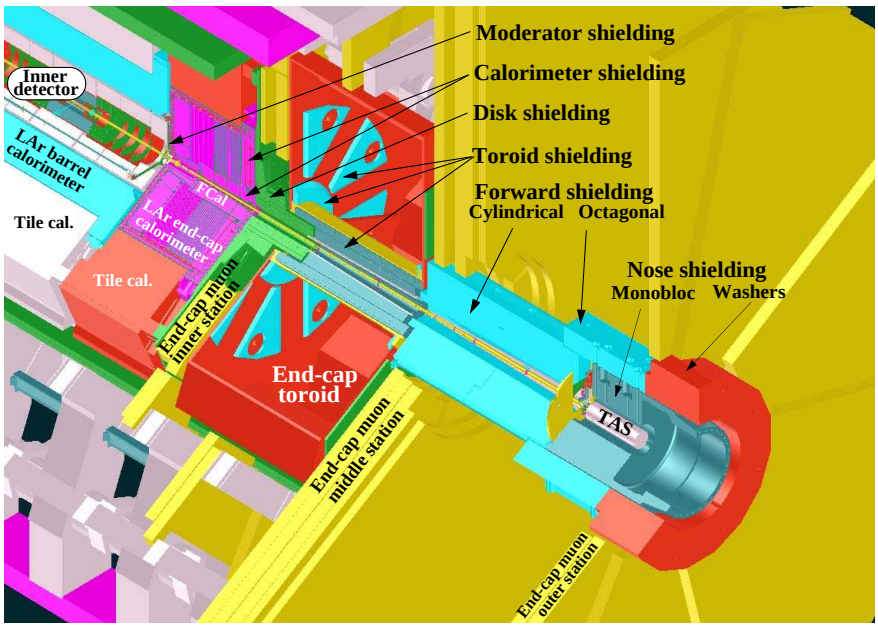

Figure 2.22: ATLAS radiation shielding elements. [13]

6 to 31 wires corresponding to widths between 10.8 mm and 55.8 mm. TGC modules contain two wire planes in the innermost wheels and the two outer wheels and three wire planes in the intermediate wheels located in front of the big MDT wheels. In each module, two cathodes are segmented with strips in the radial direction which provide a measurement of the azimuthal coordinate. The big TGC wheels consist of an outer section and an inner section with different segmentations in the ϕ direction. Each module covers an azimuthal angle of 7.5° in the outer and of 15° in the inner section. The wheels cover the region $1.05 < |\eta| < 2.4$ except for the innermost wheel which covers the region $1.05 < |\eta| < 1.92$.

2.8 Muon Spectrometer Performance

The ATLAS muon spectrometer provides an additional measurement of the transverse momentum of muons over the range $|\eta| < 2.7$ that does not depend on the momentum measurement in the Inner Detector. For muons with a momentum of 100 GeV a momentum resolution of 3.1% is expected both in the central and forward regions [17]. In the forward region the resolution degrades for muons with low momenta due to multiple scattering and energy loss fluctuations [18]. The resolution expected for muons with a momentum of 10 GeV in directions close to $\eta = 2$ is 6.4%. In the central region, the resolution for muons with a large momentum degrades due to the reduced bending by the magnetic field. For muons with a momentum of 1000 GeV the expected resolution is 10.5% in the central region.

2.9 Shielding

Several shielding components have been installed in the forward regions of ATLAS to protect the Inner Detector and the forward muon chambers from radiation produced mainly in the endcap and forward calorimeters, the beam pipe and the TAS collimator. The layout of the shielding is shown in figure 2.22. The innermost part of the shielding is installed on the inside surfaces of the electromagnetic endcap calorimeter and the forward calorimeter. It is made of polyethylene doped with B_4C. Low-

energetic neutrons from the calorimeters are captured by the dopant and thus the radiation level in the Inner Detector coming from the forward calorimeters is reduced. Several brass shielding elements and calorimeter endcap plugs are installed inside the endcap cryostats on the outside of the endcap and forward calorimeters in the direction of increasing $|z|$. These shielding elements reduce the radiation level in the forward muon spectrometer coming from the calorimeter. The moderator shielding and the forward LAr calorimeter plugs are shown in figure 2.14.

A large steel shielding disk is installed in front of the first muon endcap disks. In addition to providing shielding it serves as support for the muon chambers and as a link between the central detector region and the tile calorimeter for the solenoid field flux return. The endcap toroid cryostats contain several moderator shielding elements made of polyethylene doped with boron to further reduce the radiation in the middle and outer muon spectrometer wheels. The beam pipe inside the toroid cryostats is covered with a cast-iron tube surrounded by moderator and the toroid bore tube made of steel. The forward region contains further shielding elements around the beam pipe and the TAS collimator made of cast iron and concrete as shown in figure 2.22. The TAS collimator serves to protect the first LHC quadrupole magnet from the products of collisions inside ATLAS and absorbs the largest fraction of the energy from collisions together with the forward calorimeter.

2.10 Trigger

The ATLAS trigger consists of 3 layers operating at different rates and levels of detail. The level 1 trigger has been implemented using custom-made electronics. It reduces the event rate from 40 MHz at which bunch crossings will take place under nominal conditions to 75 kHz at which the full detector readout can be operated. The level 2 trigger uses the information in regions of interest around the trigger objects identified by the level 1 trigger to reduce the event rate to 3.5 kHz. At this rate the analysis of the complete event information is feasible. The third level of the trigger is called event filter. It uses the complete event information to reduce the event rate to 200 Hz at which the data is written to long-term storage.

The level 1 trigger is based on the calorimeter, the muon trigger chambers and special additional triggers such as a filled-bunch trigger based on the beam-pickup monitors and a minimum bias trigger for the early low luminosity phase based on dedicated scintillator counters installed in front of the endcap calorimeters. In the muon trigger chambers, coincidences in at least two chambers passing one of six p_T thresholds are used as the trigger. Typically, coincidences are required in all but one of the individual layers of the participating multi-layer chambers. Six different p_T thresholds can be defined by the width of the coincidence window as described in section 2.7. Three low-p_T thresholds in the approximate range from 6 GeV to 9 GeV are defined using a chamber close to a reference chamber as illustrated in figure 2.21. Three high-p_T thresholds in the range from 9 GeV to 35 GeV are defined using a chamber at a larger distance from the reference chamber.

For the level 1 calorimeter trigger e/γ, jet and τ signatures are reconstructed and identified. Groups of calorimeter cells in an area of a fixed size in the η-ϕ plane called trigger towers are used as the basic objects. Trigger towers have a surface area in the η-ϕ plane of 0.1×0.1 in a large fraction of the calorimeter. They are created separately for the electromagnetic and hadronic calorimeters.

Groups of 2×2 trigger towers in both the hadronic and electromagnetic calorimeters called jet elements are used to search for jet signatures. A jet trigger can be defined for search windows with a size of 2×2, 3×3 or 4×4 jet elements. For each allowed group of jet elements in the calorimeter the transverse energy is calculated and compared with a list of thresholds. To avoid overlap, the area of the jet trigger candidate is required to be centered around a 2×2 set of jet elements that are a local maximum. In total, eight combinations of thresholds and search window sizes can be defined.

Groups of 2×2 trigger towers in the electromagnetic calorimeter are used to search for e/γ signatures.

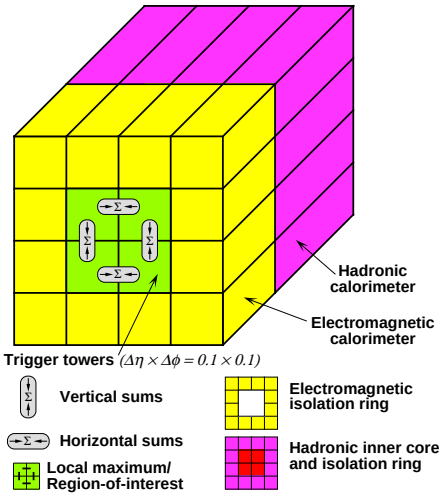

Figure 2.23: Calorimeter readout for the level 1 e/γ and τ triggers. [13]

The transverse energy is calculated for all 4 combinations of 1×2 or 2×1 trigger towers and compared with a list of thresholds. For a trigger at least one of the combinations is required to pass the threshold. Each of the 12 towers surrounding the 2×2 group and the 4 towers in the adjacent 2×2 group in the hadronic calorimeter is required to have a transverse energy below an isolation threshold. To avoid overlaps, the 2×2 group in the electromagnetic calorimeter is required to be a local maximum. The algorithm is applied to all groups of 2×2 electromagnetic towers. The principle of operation of the e/γ trigger is illustrated in figure 2.23.

Tau trigger signatures are defined in a similar way to e/γ signatures. The transverse energy of the 4 possible combinations of electromagnetic tower pairs in a group of 2×2 is added to the transverse energy of the adjacent 2×2 group of hadronic towers and the result for at least one combination is required to pass a predefined threshold. Isolation thresholds are set for the 12 towers surrounding the 2×2 group in the electromagnetic calorimeter and the 12 towers surrounding the 2×2 group in the hadronic calorimeter.

Eight sets of thresholds are available for the e/γ trigger and an additional 8 sets are available for either the e/γ trigger or the τ trigger. The numbers of signatures passing each set of thresholds are counted and $E_{\mathrm{T}}^{\mathrm{miss}}$ and several other quantities are calculated and forwarded to the central trigger processor. The results of the muon and calorimeter triggers are combined and a level 1 accept signal together with an 8 bit word describing the type of trigger is issued if the conditions for at least one trigger item are satisfied.

The level 1 trigger has a latency of less than $2.5\,\mu$s during which the data is stored in subdetector-specific pipeline memories. When a level 1 accept signal is issued the data is processed by the detector-specific readout drivers and stored in readout buffers. The information on regions of interest is passed to the level 2 trigger which requests and analyses the data in the regions of interest. If the event passes the level 2 selection criteria the data is forwarded from the readout buffers to an event builder which prepares the data for reconstruction in the event filter. The event filter processes the event using the reconstruction framework that is used for offline event reconstruction. Events that pass the event filter selection are assigned to trigger streams and stored on output nodes of the ATLAS trigger and data acquisition system. From the output nodes the events are copied to the CERN long-term storage system.

Chapter 3

Identification of hadronic τ decays using the τ lepton flight path

At the LHC, many processes involving undiscovered non-Standard Model particles are expected to have signatures with τ leptons in the final state. In supersymmetric models decays to τ leptons can be dominant for both charged and neutral Higgs bosons with a large range of possible masses. Tau leptons also occur as final state particles in supersymmetric cascade decays [2]. The production of a Standard Model Higgs boson in vector boson fusion with the decay $H \to \tau^+\tau^-$ is one of the potential discovery processes with the ATLAS experiment at small Higgs boson masses [19, 1, 2]. In models beyond the Standard Model, more resonances with large masses may occur which predominantly decay into τ leptons [2].

Tau leptons decay to electrons or muons with a total branching ratio of approximately 35%. Hadronic τ decays are classified by the number of charged hadrons as 1-prong (approximately 50%) or 3-prong (approximately 15%) decays. Decays with more than 3 charged hadrons have a branching ratio of approximately 0.1% and are usually neglected for the purpose of identifying the decays of new particles. The branching ratios for the most common classes of τ decays are given in table 3.1.

Hadronic τ lepton decays exhibit characteristic signatures with low track multiplicities and strongly collimated energy deposits in the calorimeter. In addition, the lifetime of the τ lepton leads to measurable non-zero impact parameters of the decay products. The latter are characteristic also for electrons and muons from leptonic τ lepton decays. Dedicated algorithms have been implemented for the identification of hadronic τ lepton decays.

The quantities characterising the collimation of the τ decay products depend on the momentum of the τ lepton and the dependence has to be taken into account in identification methods. Tau leptons in decays of a Standard Model Higgs boson with a mass of 120 GeV produced in vector boson fusion will have a transverse momentum of the order 40 GeV to 60 GeV. In early ATLAS data the Standard Model processes $W \to \tau\nu$ and $Z \to \tau^+\tau^-$ will allow the study of the performance of the reconstruction and identification of hadronic τ decays using τ leptons of slightly smaller average transverse momenta. Decays of non-Standard Model bosons with large masses may lead to τ leptons with larger average transverse momenta of up to several hundred GeV. Tau leptons with smaller average transverse momenta are expected from supersymmetric cascade decays in some Supersymmetry scenarios [2].

Tau leptons have a lifetime of $c\tau = 87.11\mu$m and a transverse flight distance at intermediate momenta at the LHC of approximately 2-3 mm. In 1-prong decays the non-zero impact parameter may be used for the identification of the decay. In 3-prong decays it is possible to reconstruct the flight path of the τ lepton using a secondary vertex fit.

Charm- and bottom-flavoured hadrons also feature a non-zero flight distance and their decay products have non-zero impact parameters. The multiplicity of charged particles resulting from bottom decays is larger and the decay products are less collimated than in the case of τ lepton decays. Hence, an

$\tau \to \mu \nu_\mu \nu_\tau$	$(17.36 \pm 0.05)\%$
$\tau \to e \nu_e \nu_\tau$	$(17.85 \pm 0.05)\%$
$\tau \to h^\pm \nu_\tau$	$(11.61 \pm 0.06)\%$
$\tau \to \pi^\pm \nu_\tau$	$(10.91 \pm 0.07)\%$
$\tau \to h^\pm \pi^0 \nu_\tau$	$(25.94 \pm 0.09)\%$
$\tau \to h^\pm 2\pi^0 \nu_\tau$	$(9.51 \pm 0.11)\%$
$\tau \to h^\pm 3\pi^0 \nu_\tau$	$(1.34 \pm 0.07)\%$
$\tau \to 3h^\pm \nu_\tau$	$(9.80 \pm 0.08)\%$
$\tau \to 3h^\pm \pi^0 \nu_\tau$	$(4.75 \pm 0.06)\%$

Table 3.1: Branching ratios for different categories of τ decays. [20]

identification based purely on the impact parameter or the flight distance is feasible in the case of *b*-tagging while for the τ identification it is preferable to use the impact parameters and the flight distance in combination with other Inner Detector and calorimeter observables.

The offline reconstruction of hadronic τ decays is seeded by a jet reconstructed in the calorimeter passing a transverse momentum threshold or by a track passing a quality selection and a transverse momentum threshold. Two algorithms for the different seed choices have been developed [21, 22, 23] using different reconstruction and identification approaches. In both algorithms, τ candidate objects are created starting from the seeds. The energy, momentum, charge and charged particle multiplicity of the visible τ decay products are estimated and quantities characterising the collimation and isolation of the τ candidate are calculated and used for a τ candidate selection based on cuts or advanced multivariate techniques.

The energy of the τ candidate is estimated in the calorimeter-based algorithm from the seed energy using an H1-style calibration as discussed briefly in section 4.2.3. In the track-seeded algorithm, the track selection is optimized to balance a large efficiency with a small migration rate between the 1-prong and 3-prong categories and to reject tracks from conversions in decays with neutral pions. The energy of the τ candidates is calculated following an energy-flow approach using the track momentum at small transverse momenta instead of charged energy deposits in the calorimeter. A dedicated reconstruction of π^0 subclusters is performed.

The calorimeter-seeded and track-seeded algorithms have been merged into a single algorithm using either type of seed. The merged algorithm provides a common set of τ candidates with the properties calculated by each sub-algorithm depending on the availability of the respective seed. In this chapter track-seeded τ candidates are used.

The efficiency of the track reconstruction in hadronic τ decays is discussed in section 3.1. The performance of the ATLAS detector for the reconstruction of primary vertices is studied in section 3.2. In sections 3.3 and 3.4, the performance of the reconstruction of the impact parameters and the transverse flight distance is presented. In section 3.5 an improved τ identification is described which uses the impact parameter significances and the transverse flight path significance in combination with other discriminating observables in an artificial neural network. The studies in this chapter are performed using mostly datasets of simulated $Z \to \tau^+\tau^-$ and $W \to \tau\nu$ events. Additionally, simulated QCD dijet events are used for studies requiring fake τ candidates. The datasets are listed in table 3.2.

Dataset	Process	$\sqrt{s}$ (TeV)	Task ID	Events used
106052	$Z \to \tau^+\tau^-$	10	95953 - 95955	998 421
106023	$W \to \tau\nu$	10	95962, 95964 - 95966	1 199 273
106573	$A \to \tau^+\tau^-, m_A = 800$ GeV	10	95978, 95979	99 954
105010	QCD dijet	10	99034, 99035	1 000 000
105011	QCD dijet	10	95975, 95976	936 178
105012	QCD dijet	10	95970 - 95973	1 400 000

Table 3.2: Monte Carlo datasets used for the study of hadronic τ decays. ATLAS software releases 14.2.10.1 and 15.3.1.6 were used for the simulation and the reconstruction, respectively.

3.1 Track reconstruction performance

The track reconstruction efficiency is studied for charged pions from hadronic τ decays using simulated $Z \to \tau^+\tau^-$ and $W \to \tau\nu$ events. The tracks are required to pass a quality selection as defined in [13]. The selection consists of the following cuts:

- $p_T > 1$ GeV
- $|\eta| < 2.5$
- $|d_0| < 2\,\text{mm}$
- $|z_0 \sin(\theta)| < 10\,\text{mm}$
- Number of hits in the silicon detectors ≥ 7

In addition, it is required that at least 80% of the hits of a track weighted by the detector element were created by the original pion. The weights 10, 5 and 1, respectively, are assigned to hits in the Pixel Detector, the SCT and the TRT.

Here, the track parameters at the perigee with respect to the primary vertex are used. The perigee is defined as the point on the track at the position of closest approach to the vertex in the transverse plane. The transverse impact parameter d_0 is defined as the distance between the perigee and the vertex in the transverse plane. The impact parameter z_0 is the distance between the perigee and the vertex in the z direction. The component orthogonal to the track is obtained by multiplying z_0 by $\sin(\theta)$. The perigee parametrisation of tracks is illustrated in figure 3.1.

Figure 3.2 shows the track reconstruction efficiency as a function of the p_T and $|\eta|$ of the pion. Compared to a similar study presented in [2] that used an earlier release of the ATLAS software and a different detector geometry the efficiency is observed to be reduced by approximately 2%. A difference of slightly above one percent is explained by a reduction of the primary vertex reconstruction efficiency. The fraction of $Z \to \tau^+\tau^-$ events without a reconstructed primary vertex is 1.6% in the dataset used for figure 3.2. In a dataset produced using a software release and detector geometry similar to the ones used for [2] the fraction of events without a primary vertex is 0.4%. In events without a reconstructed primary vertex the impact parameter z_0 is calculated with respect to the center of the interaction region and tracks are likely to fail the cut on $|z_0 \sin(\theta)|$. A similar effect may explain the reduced efficiency for 1-prong decays with respect to the efficiency for 3-prong decays since the primary vertex will be defined better on average in events with 3-prong decays. For comparison the efficiency without the application of track quality cuts is shown in figure 3.3.

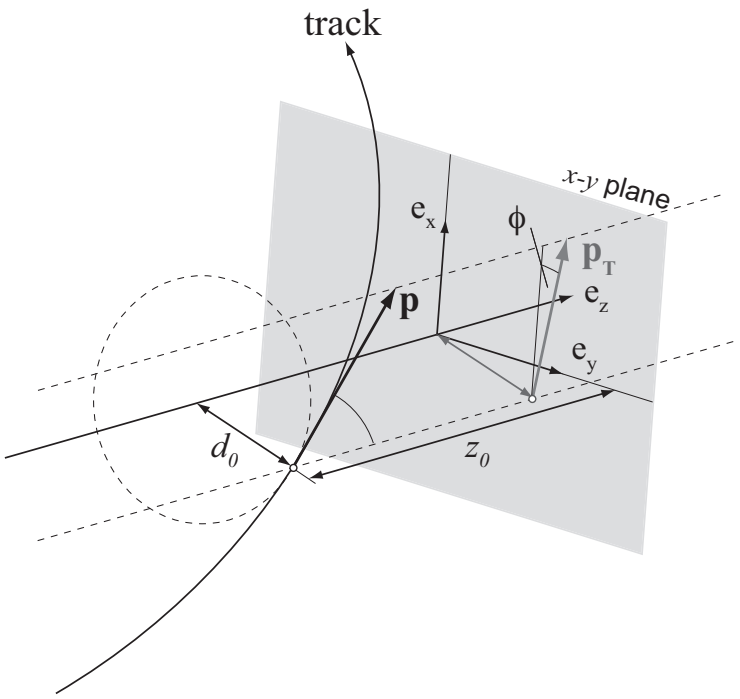

Figure 3.1: Graphical illustration of the perigee parametrisation of tracks. [24]

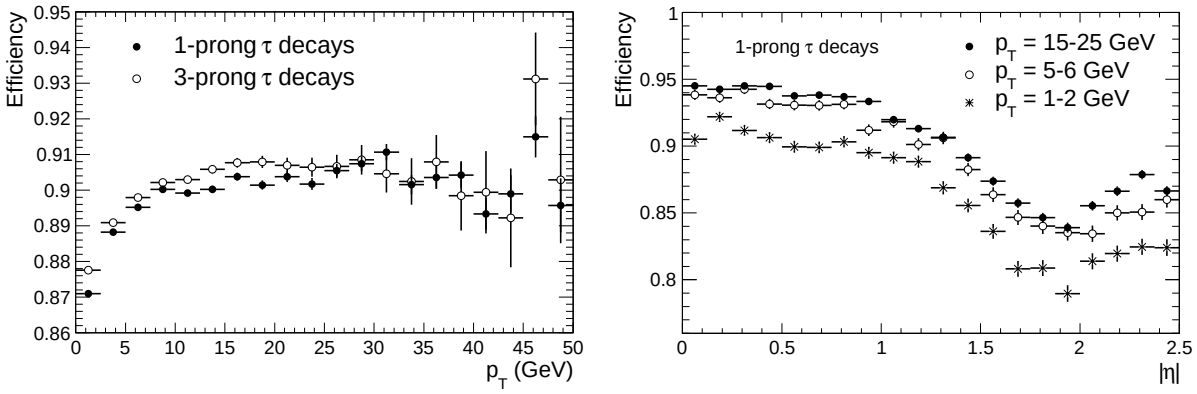

Figure 3.2: Track reconstruction efficiency for charged pions from τ lepton decays as a function of p_T (*left*) and $|\eta|$ (*right*) using standard track quality cuts in simulated $Z \to \tau^+\tau^-$ and $W \to \tau\nu$ events.

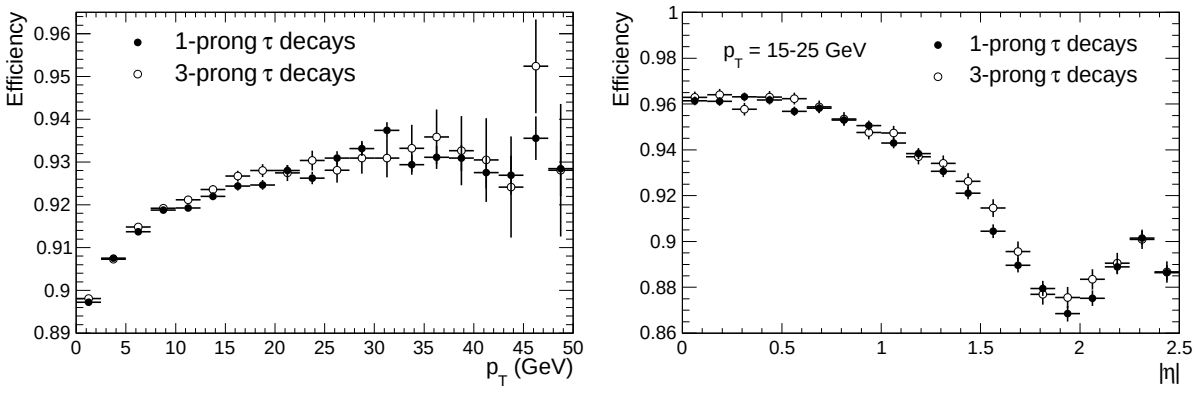

Figure 3.3: Track reconstruction efficiency for charged pions from τ lepton decays as a function of p_T (*left*) and $|\eta|$ (*right*) without track quality cuts in simulated $Z \to \tau^+\tau^-$ and $W \to \tau\nu$ events.

The track reconstruction efficiency in three-prong decays decreases with increasing visible transverse momentum of the τ lepton due to the decreasing opening angle between the pions. Figure 3.4 shows the maximum distance ΔR in the η-ϕ plane among the three possible combinations of pions from 3-prong τ decays for three different ranges of the visible transverse momentum of the τ candidate. Figure 3.5 shows the fraction of pion pairs reconstructed as a pair of tracks as a function of ΔR between the pions and the track reconstruction efficiency as a function of the visible transverse momentum of the τ lepton. A dataset of simulated $A \to \tau^+\tau^-$ events with an A boson mass of 800 GeV is used as it provides τ leptons with a large range of visible transverse momenta. At small opening angles the efficiency of the reconstruction of 2 tracks decreases by approximately 15% with respect to the maximum. The difference of the track reconstruction efficiencies for 1-prong decays and 3-prong decays increases to up to 10% at visible transverse momenta close to 500 GeV.

3.2 Primary vertex reconstruction

At the nominal LHC luminosity of $10^{34}\,\mathrm{cm}^{-2}\mathrm{s}^{-1}$ and a center-of-mass energy of 14 TeV, 23 proton-proton interactions are expected to take place on average in every bunch crossing. The interaction region is expected to have a Gaussian shape with a σ of approximately 11 μm in the x and y directions and 5.6 cm in the z direction. The resolution of the Inner Detector is approximately 100 μm in the z direction. This allows the separate reconstruction of the primary interaction vertex and interaction vertices of additional minimum bias interactions.

The primary vertex reconstruction algorithm used in the ATLAS offline reconstruction [25] is an implementation of an adaptive multi-vertex fit [26]. Initially, a single vertex is fitted to tracks passing a loose preselection requiring compatibility with an origin in the expected interaction region. After the fit the compatibility of the tracks with the fitted vertex is evaluated and tracks found to be incompatible are used to form a new vertex seed. The procedure is iterated. In each iteration the compatibility of the tracks with all vertices is evaluated and the assignment of tracks to vertices is allowed to change. A weight function is used to determine the compatibility of a track with a given vertex. The weight function is adjusted in each iteration in a way such that the χ^2 interval covering the largest variation of weights is reduced and the assignment becomes stricter. In an analogy with the thermodynamic process of annealing the parameter that is reduced to increase the rigidity of the track-vertex association is called temperature. The vertex of the signal interaction is identified from the list of reconstructed vertices as

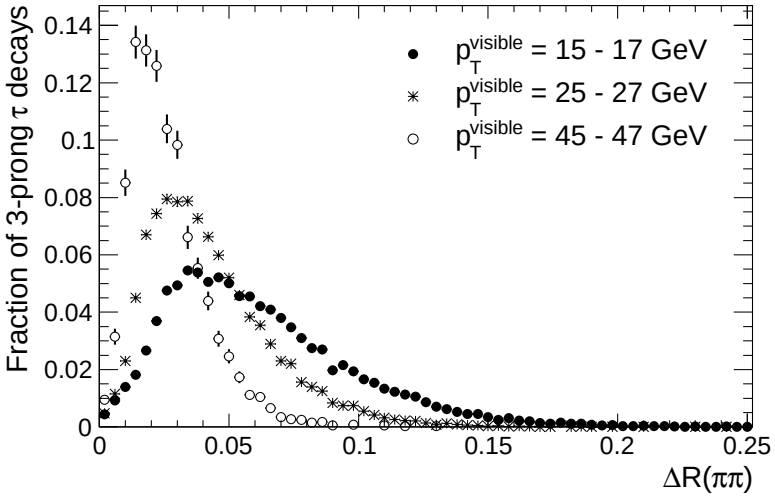

Figure 3.4: Maximum opening angle in the η-ϕ plane ΔR among the three possible combinations of pion pairs in 3-prong τ decays for three different ranges of the visible transverse momentum of the τ lepton.

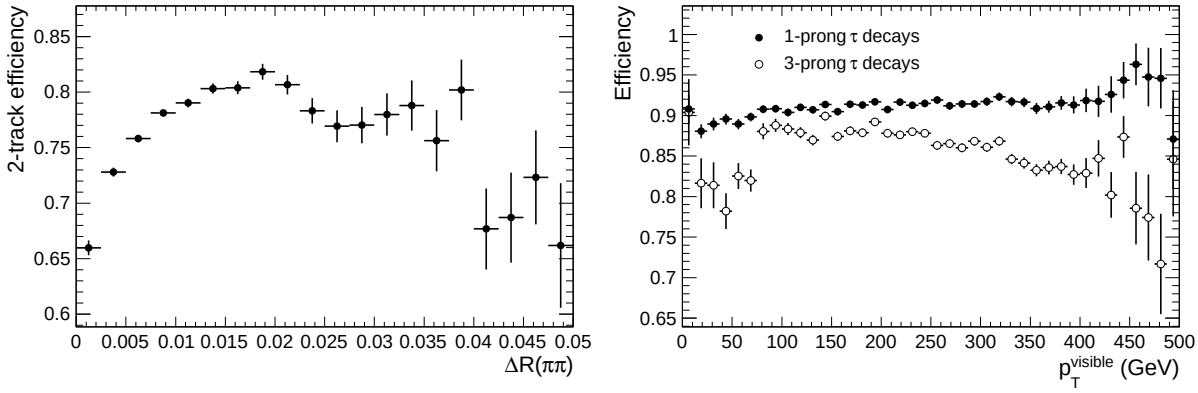

Figure 3.5: Fraction of pion pairs from τ lepton decays reconstructed as a pair of tracks as a function of ΔR (*left*) and track reconstruction efficiency for pions from τ decays as a function of the visible transverse momentum of the τ lepton (*right*) for standard track quality cuts in simulated $A \rightarrow \tau^+\tau^-$ events with an A boson mass of 800 GeV.

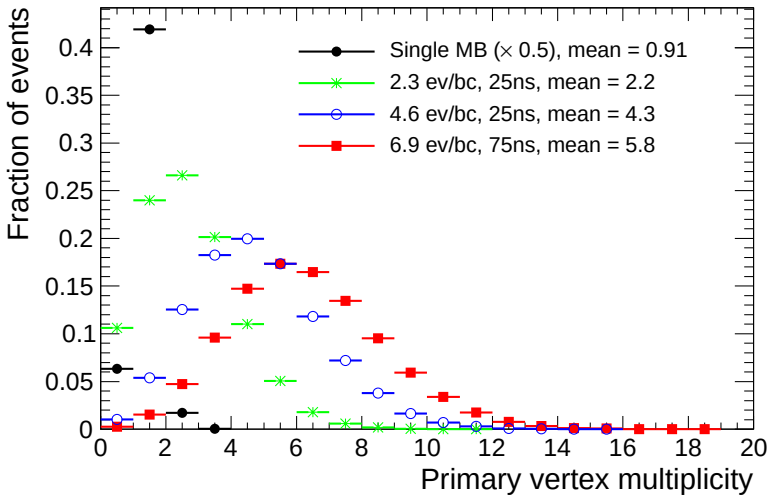

Figure 3.6: Primary vertex multiplicity in simulated minimum bias data for different luminosity scenarios.

the vertex with the largest $\sqrt{N}\Sigma p_T^2$ where the sum is calculated over all N tracks used in the vertex fit.

Figure 3.6 shows the primary vertex multiplicity reconstructed in single minimum bias events and in minimum bias events at luminosities corresponding to average numbers of 2.3 and 4.6 interactions per bunch crossing at the nominal spacing of 25 ns and of 6.9 interactions per bunch crossing at a bunch spacing of 75 ns. The average reconstructed primary vertex multiplicity is close to the true one. The simulation of datasets with multiple minimum bias interactions close in time to the triggered bunch crossing is discussed in section 4.4.

Residuals and pulls of the primary vertex position in the x and z directions in simulated $Z \rightarrow \tau^+\tau^-$ and $W \rightarrow \tau\nu$ events are shown in figure 3.7. The residuals are defined here as the difference between the measured value and the true value of the measured quantity. The pulls are defined as the residuals divided by the expected error on the measured quantity. The distribution of the residual of the x coordinate has a σ from a Gaussian fit of 14.1 μm which is close to the σ of the distribution of the true x coordinate of 15.0 μm. The distributions in the y direction are similar to the distributions in the x direction. The distribution of the residual of the z coordinate has significant tails, hence the resolution is determined from a Gaussian fit in the range $[-0.1, 0.1]$ mm. A σ of 55.6 μm is observed. The pull distributions of both coordinates have a Gaussian shape with a σ close to one.

Since the primary vertex resolution in the x and y directions is similar to the width of the interaction region, the transverse impact parameter calculated with respect to the center of the interaction region is a good approximation for the impact parameter with respect to the primary vertex.

3.3 Impact parameter reconstruction performance

The performance for the reconstruction of the impact parameters and the transverse flight distance is studied for tracks assigned to τ candidates. Here, only τ candidates reconstructed by the track-seeded τ reconstruction algorithm are considered. The seed track is required to pass the standard track selection and to have a transverse momentum above 6 GeV. Additional tracks are required to pass stricter requirements on the impact parameters and to have a hit in the B-layer to reject tracks from conversions in τ decays with neutral pions.

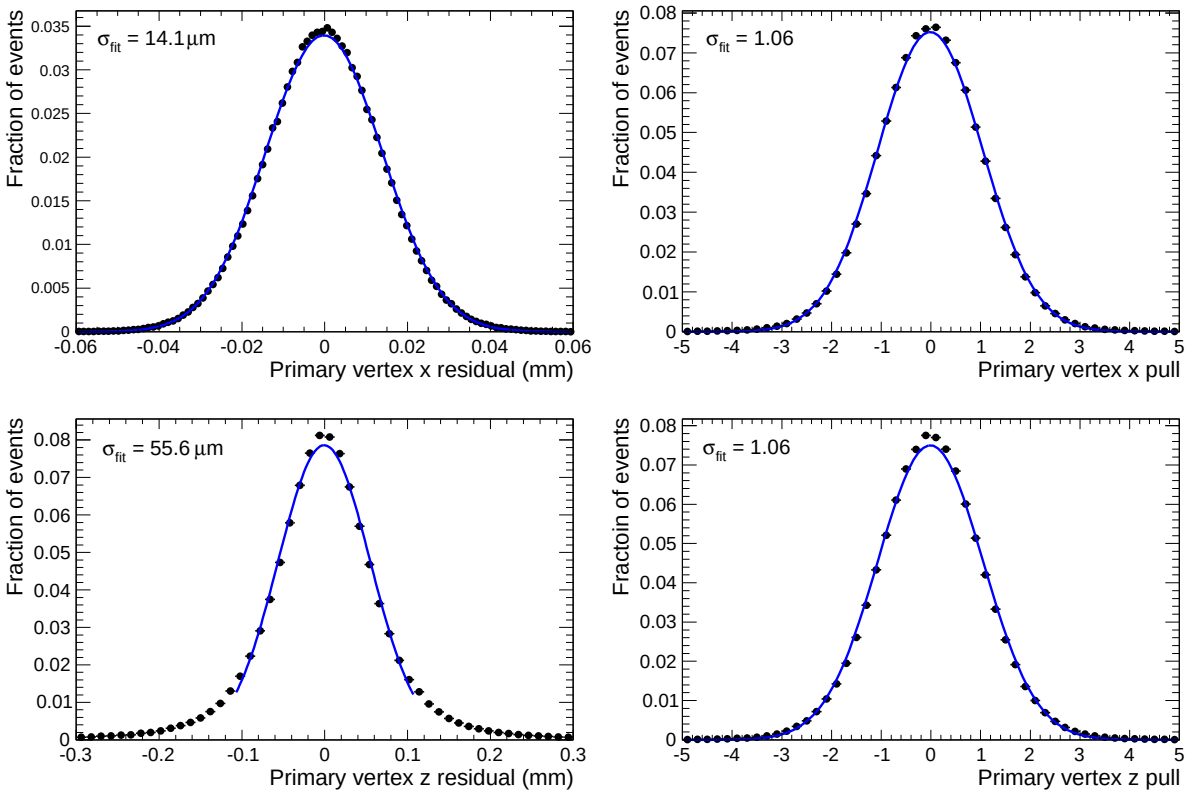

Figure 3.7: Residual (*left*) and pull (*right*) of the primary vertex position in the x (*top*) and z (*bottom*) directions in simulated $Z \to \tau^+\tau^-$ and $W \to \tau\nu$ events.

The following track quality requirements are applied to the seed track:

- $p_T > 6$ GeV
- $|d_0| < 2\,\text{mm}$
- $|z_0 \sin(\theta)| < 10\,\text{mm}$
- Number of hits in the silicon detectors ≥ 7

The following track quality requirements are applied to additional tracks:

- $p_T > 1$ GeV
- $|d_0| < 1\,\text{mm}$
- $|z_0 \sin(\theta)| < 1.5\,\text{mm}$
- Number of hits in the silicon detectors ≥ 7
- Number of hits in the *B*-layer ≥ 1
- Number of hits in the Pixel Detector ≥ 2

Figure 3.8 shows the residuals and pulls of the transverse impact parameter d_0 and the impact parameter in a plane containing the z axis $z_0 \sin(\theta)$ for pions from 1-prong τ decays reconstructed by the track-seeded algorithm in simulated $Z \to \tau^+\tau^-$ and $W \to \tau\nu$ events. The impact parameter is calculated with respect to the identified primary vertex. For the calculation of the impact parameter, the position of the primary vertex is estimated without using the track from the τ candidate.

The residual distributions are composed of contributions with different widths depending on the p_T and $|\eta|$ of the track. Since the variation of the widths of the different contributions is not significantly larger than an order of magnitude, the distributions may be approximated by a double Gaussian. The resolutions are determined from a double Gaussian fit. For the transverse impact parameter σ values of $20\,\mu$m and $42\,\mu$m are obtained. For $z_0 \sin(\theta)$ the fit results in σ values of $51\,\mu$m and $119\,\mu$m. The pull distributions are Gaussian with a σ close to one in each case.

The resolutions of the impact parameters d_0 and $z_0 \sin(\theta)$ are shown in figure 3.9 for pions from 1-prong τ decays as a function of $|\eta|$. Different distributions are shown for the impact parameter with respect to the true primary vertex and the impact parameter with respect to the reconstructed primary vertex. In both cases the true impact parameter with respect to the true primary vertex is used as the reference value in the calculation of the residuals. The resolution is calculated as the σ from a Gaussian fit to the central interval covering 80% of the distribution. The resolution of the transverse impact parameter with respect to the reconstructed primary vertex increases from $20\,\mu$m in the central detector region to $30\,\mu$m in the forward region. The resolution of $z_0 \sin(\theta)$ decreases from approximately $130\,\mu$m in the central region to $55\,\mu$m in the forward region.

Figure 3.10 shows the significance of d_0 and $z_0 \sin(\theta)$ of the track associated with 1-prong τ candidates, where the significance is calculated as the value divided by its estimated error,

$$\text{Significance}(d_0) = d_0/\sigma(d_0) \tag{3.1}$$

$$\text{Significance}(z_0 \sin(\theta)) = z_0 \sin(\theta)/\sigma(z_0 \sin(\theta)). \tag{3.2}$$

Distributions are shown for τ candidates reconstructed from 1-prong τ decays, τ candidates seeded by a track from a *b*- or *c*-hadron decay and τ candidates seeded by other tracks. The sign of the impact

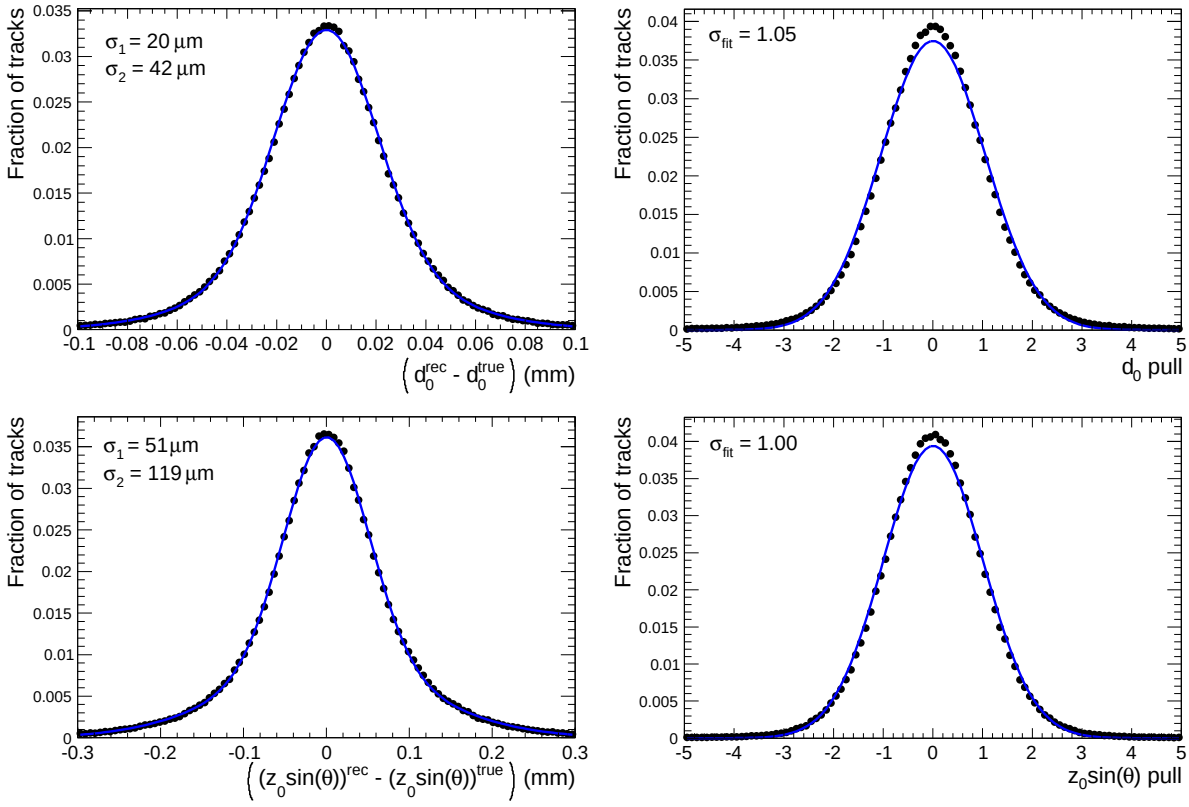

Figure 3.8: Residual (*left*) and pull (*right*) of the transverse impact parameter d_0 (*top*) and the impact parameter in a plane containing the z axis $z_0 \sin(\theta)$ (*bottom*). The resolution includes contributions from the primary vertex reconstruction and the track reconstruction.

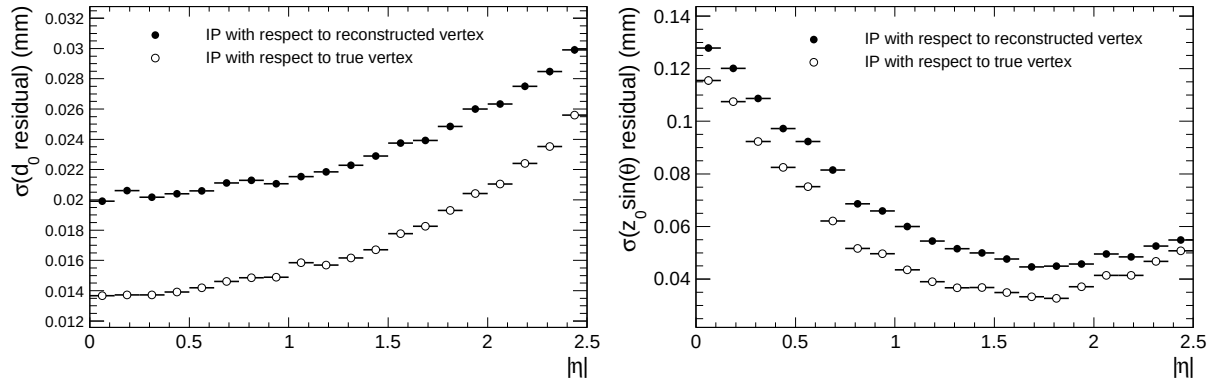

Figure 3.9: Resolutions of the transverse impact parameter d_0 (*left*) and the impact parameter in a plane containing the z axis $z_0 \sin(\theta)$ (*right*). The reconstructed impact parameter is compared in each case to the true impact parameter with respect to the true primary vertex.

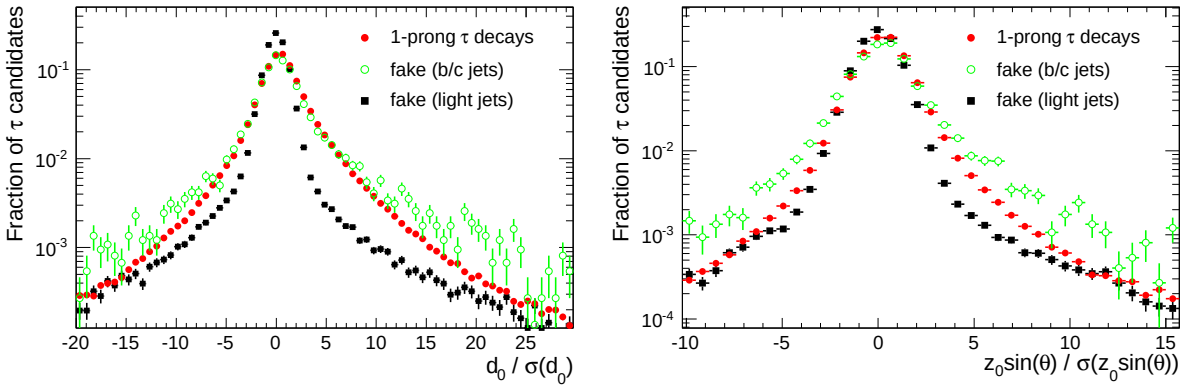

Figure 3.10: Significance of the signed transverse impact parameter d_0 (*left*) and the impact parameter in a plane containing the z axis $z_0 \sin(\theta)$ (*right*) for 1-prong τ candidates reconstructed from the decay products of hadronic τ decays, for 1-prong τ candidates reconstructed from the decay products of b or c hadron decays and for 1-prong τ candidates reconstructed from light jets.

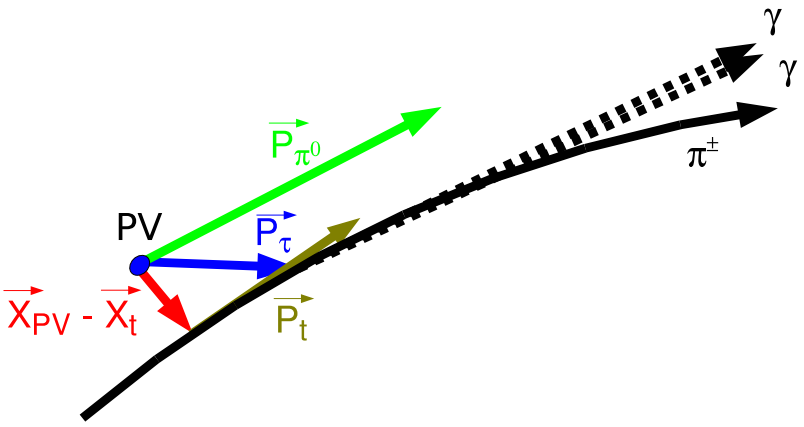

Figure 3.11: Graphical illustration of the vectors used in the calculation of the lifetime sign of the impact parameter for 1-prong τ candidates (not to scale).

parameter is calculated with respect to the direction of the transverse energy-weighted barycenter of the π^0 clusters associated with the τ candidate if present. The sign is calculated as [2, 27]

$$\text{sign}(d_0) = \text{sign}\left((\vec{P}_{\pi_0} \times \vec{P}_t) \cdot (\vec{P}_t \times (\vec{X}_{PV} - \vec{X}_t))\right) \tag{3.3}$$

where $\vec{P}_{\pi_0}$ is a vector in the direction of the transverse energy-weighted barycenter of the π^0 clusters, $\vec{P}_t$ is a vector in the direction of the track momentum at the perigee, $\vec{X}_{PV}$ is the position of the primary vertex and $\vec{X}_t$ is the position of the perigee. The different vectors are depicted in figure 3.11. This sign is positive if the point of closest approach between the track linearized at the perigee and the axis defined by the π^0 clusters is located in front of the vertex in the direction of the π^0 clusters. For pions from τ lepton decays, the sign is positive in the ideal case of a track reconstruction without errors if the sign is calculated with respect to the τ lepton momentum. Thus, it reflects the finite lifetime and flight distance of the τ lepton. The direction of the axis defined by the π^0 clusters is taken from the calorimeter and the axis is assumed to pass through the primary vertex. If no π^0 clusters are associated with the τ candidate and the τ candidate has a calorimeter seed, the sign of the impact parameter is calculated with respect to the direction of the calorimeter seed. If neither π^0 clusters nor a calorimeter seed are present, the default sign is used which is positive if the difference between the azimuthal angle of the track at the perigee and the azimuthal angle of the vector pointing from the vertex to the perigee is $\pi/2 + n2\pi$ with $n \in \mathbb{Z}$ and negative otherwise.

The distribution of the d_0 significance shows a moderate discrimination power between tracks from τ decays and tracks from light jets. The absolute value of the impact parameter of tracks from *b*- or *c*-hadron decays is slightly larger than the one from τ decays. The lifetime sign of the impact parameter introduces a positive bias of the distribution as expected. The discrimination power of the $z_0 \sin(\theta)$ significance distribution is smaller than the one of the d_0 significance distribution.

3.4 Secondary vertex reconstruction performance

For τ candidates with at least 2 associated tracks a secondary vertex fit is performed. Currently, there are five different algorithms available in the ATLAS software suitable to perform the fit of a secondary vertex. All algorithms minimize a χ^2 calculated using the measured track parameters and the track parameters expressed as a function of the vertex position. The algorithms are implementations of filtering methods in which the information of individual tracks is added sequentially to the vertex estimate [28, 29, 30]. The fitters differ in the details of the implementation and the approximations [25]. Two of the vertex fitters, VKalVrt and the adaptive vertex fitter, offer the possibility to down-weight tracks with a large χ^2. In the case of the adaptive fitter the fit is iterated and a temperature parameter is lowered as described in section 3.2 for the primary vertex fit. The vertex fit is iterated also with VKalVrt since the calculation of the weights, which is based on the χ^2 with respect to the reconstructed vertex, requires an estimate of the vertex position. However, the weight function is not modified between iterations. In the following section, the distributions characterizing the secondary vertex fit are introduced using the adaptive vertex fitter. The performance of the different vertex fitters is compared after the introduction of the distributions.

Figure 3.12 shows the residuals of the secondary vertex position in the directions parallel to the τ candidate axis and orthogonal to the τ candidate axis and the *z* axis. Distributions are shown for 3-prong τ decays where each charged particle has been correctly reconstructed as a track and the 3 tracks have been assigned to a 3-prong τ candidate and for multi-prong candidates where at least one track originates from a charged particle from a τ decay. The resolution of the secondary vertex position is sensitive to the opening angle of the tracks and hence the momentum of the τ lepton. Double Gaussians are fitted to the distributions for correctly reconstructed 3-prong decays. In the parallel direction σ values of $576\,\mu$m and 1.93 mm are observed. In the orthogonal direction σ values of $9.95\,\mu$m and $21.2\,\mu$m are observed.

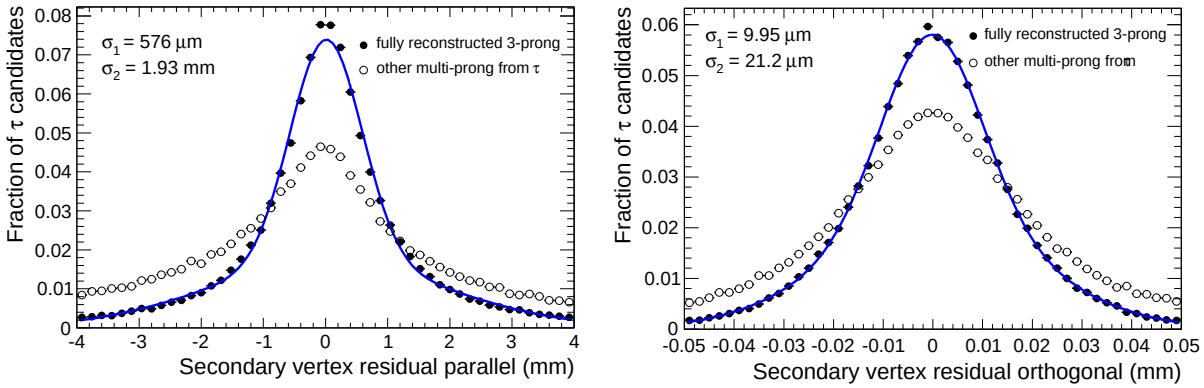

Figure 3.12: Residual of the secondary vertex position in the directions parallel (*left*) and orthogonal (*right*) to the momentum of the τ candidate in $Z \to \tau^+\tau^-$ and $W \to \tau\nu$ events. Distributions are shown for fully reconstructed 3-prong decays and for multi-prong τ candidates where at least one track originates from a particle from a τ lepton decay. The adaptive vertex fitter is used.

Residuals and pulls of the secondary vertex position in the x and z directions are shown in figure 3.13. The distributions of residuals consist of contributions with resolutions varying by almost two orders of magnitude. Hence, the distributions cannot be approximated well by double Gaussians and no fit is performed. The distributions of pulls have a Gaussian shape with a σ obtained from a fit of 1.03 and 1.04 in the x and z directions, respectively, indicating that the errors are underestimated on average by 3% and 4%, respectively.

Figure 3.14 shows the residual and pull of the transverse flight distance. A σ of 457 μm is obtained for the narrow component of a double Gaussian fitted to the residual distribution. The distribution of pulls has a Gaussian shape with a σ from a fit of 1.03. The resolution of the transverse flight path as a function of $|\eta|$ and p_T is shown in figure 3.15. The resolution is dominated by the secondary vertex resolution in the transverse direction and hence the opening angle of the tracks and the transverse momentum of the τ lepton. The p_T of the τ leptons in $Z \to \tau^+\tau^-$ and $W \to \tau\nu$ events is to a good approximation independent of η in the range of the Inner Detector acceptance, $|\eta| < 2.5$.

Figure 3.16 shows the distributions of residuals of the secondary vertex position in the direction parallel to the τ candidate axis obtained with the different vertex fitters for fully reconstructed 3-prong τ decays. No significant difference between the different vertex fitters is observed. The transverse flight path significance, which is calculated as the transverse flight path divided by its estimated error, for τ candidates reconstructed from light jets is sensitive to the rejection of outlying tracks. This is illustrated in figure 3.16 which shows the transverse flight path significance calculated with the five available vertex fitters for τ candidates from light jets. The sign of the transverse flight path significance is calculated with respect to the visible transverse momentum of the τ candidate. The distribution obtained with the adaptive vertex fitter contains the smallest fraction of τ candidates with a large transverse flight path significance and has a less pronounced tail for negative significances. Figure 3.17 shows the efficiency of a cut on the transverse flight path significance for τ candidates from τ decays as a function of the efficiency for τ candidates from light jets and the difference of the efficiency obtained with four of the vertex fitters with respect to the efficiency obtained with the fast Billoir fitter. The adaptive vertex fitter is up to 7% more efficient than the fast Billoir fitter for the selection of τ candidates from τ decay products at small efficiencies for τ candidates reconstructed from light jets. Hence, currently the adaptive vertex fitter is used for the τ identification.

The vertex calculated by the adaptive vertex fitter may be assigned a negative χ^2 or number of de-

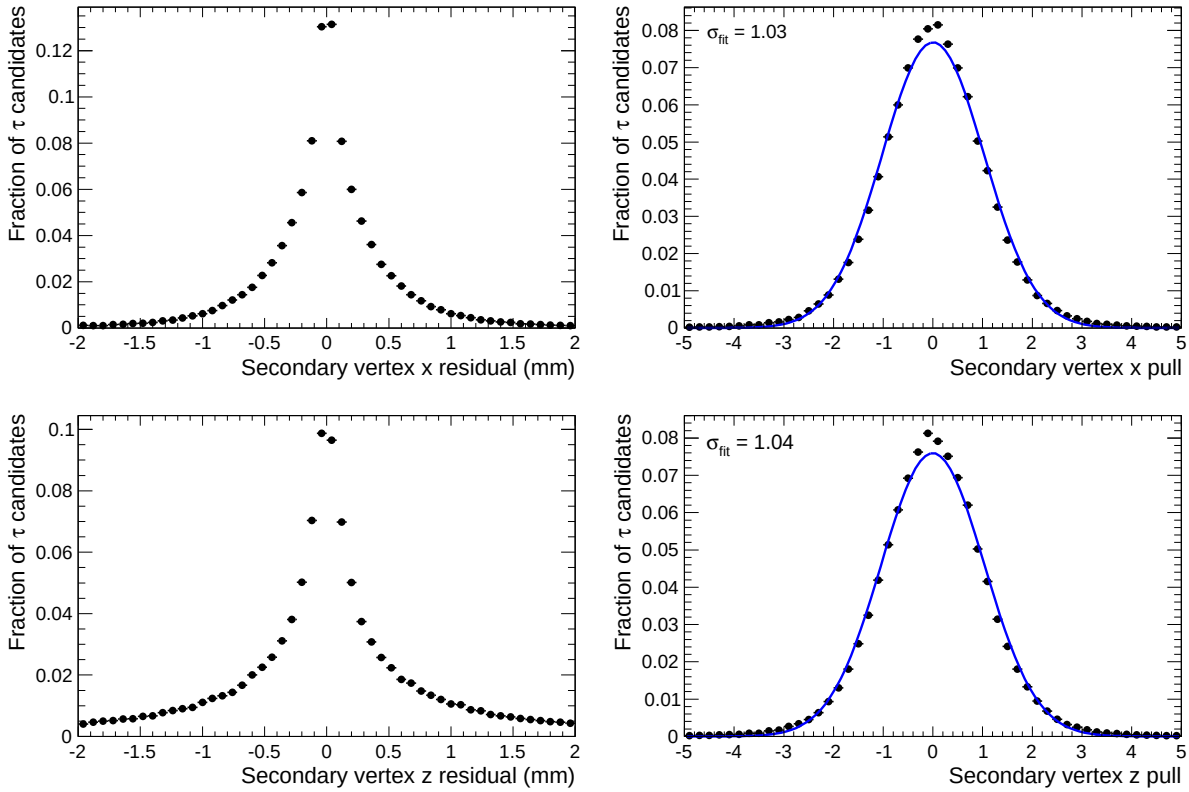

Figure 3.13: Residuals (*left*) and pulls (*right*) of the secondary vertex position in the x (*top*) and z (*bottom*) directions for fully reconstructed 3-prong τ candidates in $Z \to \tau^+\tau^-$ and $W \to \tau\nu$ events.

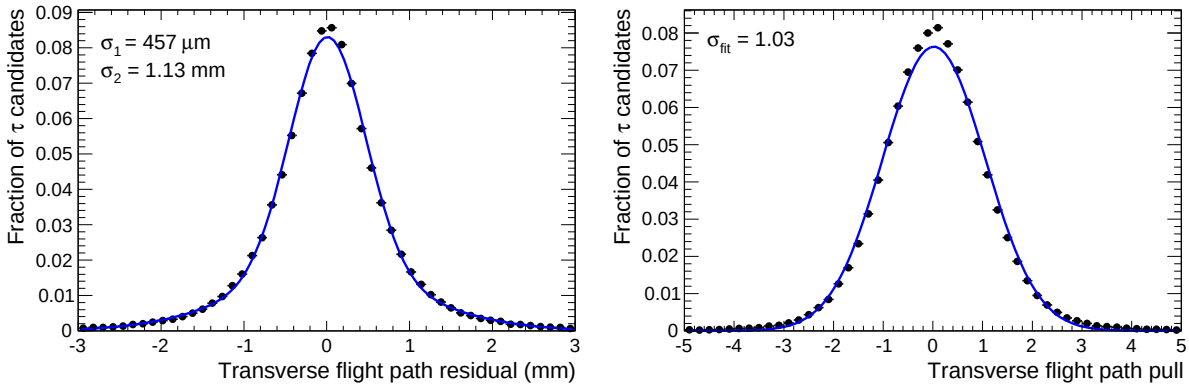

Figure 3.14: Residual (*left*) and pull (*right*) of the transverse flight path for fully reconstructed 3-prong τ decays in $Z \to \tau^+\tau^-$ and $W \to \tau\nu$ events.

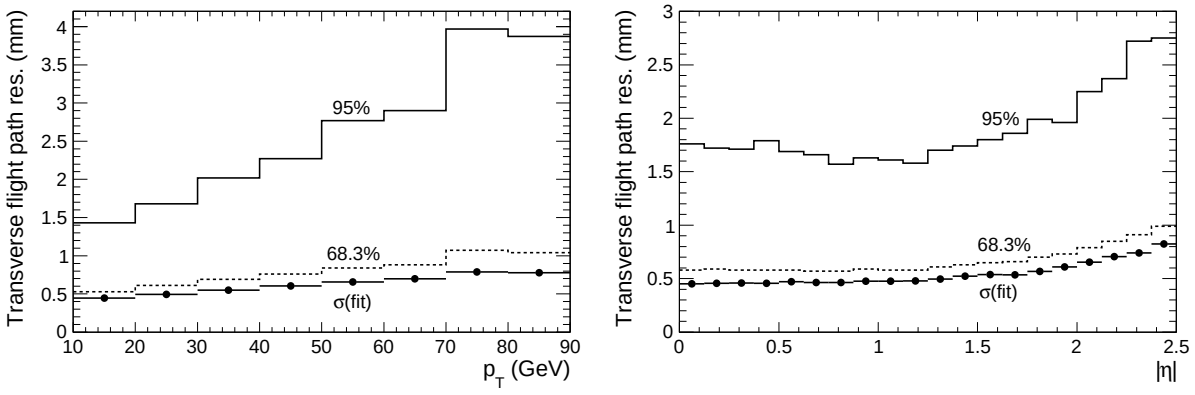

Figure 3.15: Resolution of the transverse flight path for fully reconstructed 3-prong τ decays in $Z \rightarrow \tau^+\tau^-$ and $W \rightarrow \tau\nu$ events as a function of p_T (*left*) and $|\eta|$ (*right*). The σ from a single Gaussian fit to the central interval covering 80% of the residual distribution (*markers*) and the half-widths of the central intervals covering 68.3% (*dashed line*) and 95% (*solid line*) of the residual distributions are shown.

grees of freedom if more than one track was effectively excluded from the vertex fit due to the weighting procedure. It is assumed that the tracks for the affected τ candidates are incompatible with a common vertex. The affected τ candidates are included in the τ identification as τ candidates without a secondary vertex. For fully reconstructed 3-prong candidates from hadronic τ decays an inefficiency of the vertex reconstruction of 0.37% is observed. For τ candidates with less than 4 tracks from light jets an inefficiency of 2.6% is observed.

Figure 3.18 shows the significance of the transverse flight path for fully reconstructed 3-prong τ decays, for other multi-prong τ candidates originating from a τ decay, for τ candidates reconstructed from light jets and for τ candidates with at least one track originating from the decay of a *b* or *c* hadron or one of its decay products. The distributions show a good discrimination power between τ candidates reconstructed from τ decay products and τ candidates reconstructed from light jets.

3.5 Tau identification using the impact parameter and transverse flight path

The signature that is selected during the identification step generally consists of a collimated, isolated object in the calorimeter and the Inner Detector. The track multiplicity is required to be 1 or 3 by many analyses. Two-prong τ candidates can be used to study the migration from the 1-prong and 3-prong categories. Tau candidates with more than 3 tracks are reconstructed, however the fraction of τ candidates from τ decays at those track multiplicities is negligible and the τ candidates are intended to be used as a control sample in the determination of the efficiency and fake rate of τ identification methods with collision data. The hadronic energy deposit in the calorimeter is checked for consistency with the momentum of the reconstructed tracks. The invariant mass of the τ candidate is expected to be below the τ lepton mass.

The impact parameter significances and the transverse flight path significance are used together with other observables in an artificial neural network to identify hadronic τ decays. The neural network is trained using τ candidates from τ decays in simulated $W \rightarrow \tau\nu$ and $Z \rightarrow \tau^+\tau^-$ events and τ candidates from light jets in simulated QCD dijet events reconstructed by the track-seeded algorithm in ATLAS software release 13.0.30. The Stuttgart Neural Network Simulator [31] is used to create and train the

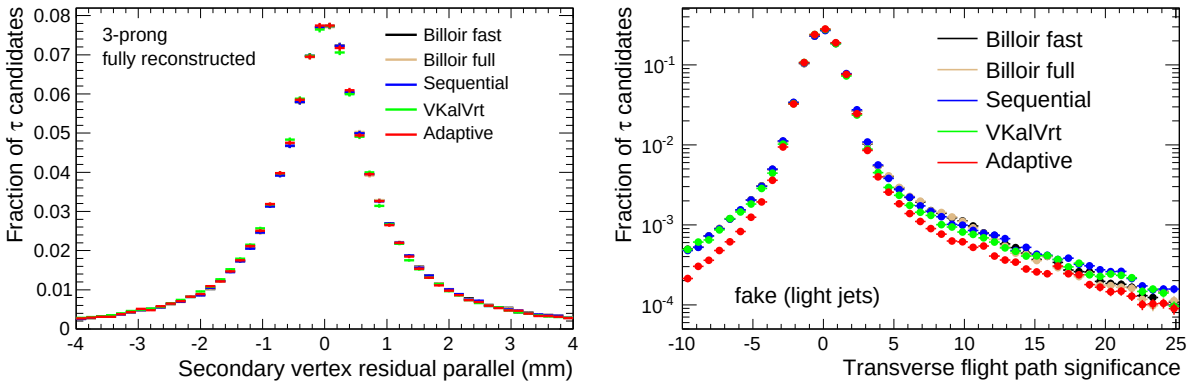

Figure 3.16: Secondary vertex residual in the direction parallel to the τ candidate momentum calculated with different vertex fitters for fully reconstructed 3-prong τ candidates (*left*) and significance of the transverse flight path calculated with different vertex fitters for τ candidates reconstructed from light jets (*right*). Only τ candidates with less than 4 tracks are used.

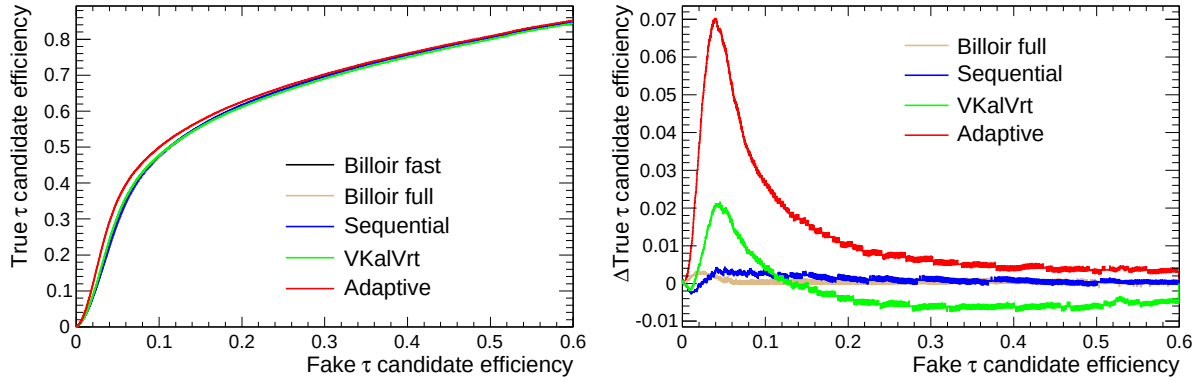

Figure 3.17: Efficiency of a cut on the transverse flight path significance for τ candidates from τ decay products as a function of the efficiency for τ candidates reconstructed from other sources (*left*) and the difference of the efficiency for τ candidates from τ decay products four of the vertex fitters with respect to the efficiency for the fast Billoir fitter (*right*). Only τ candidates with less than 4 tracks are used.

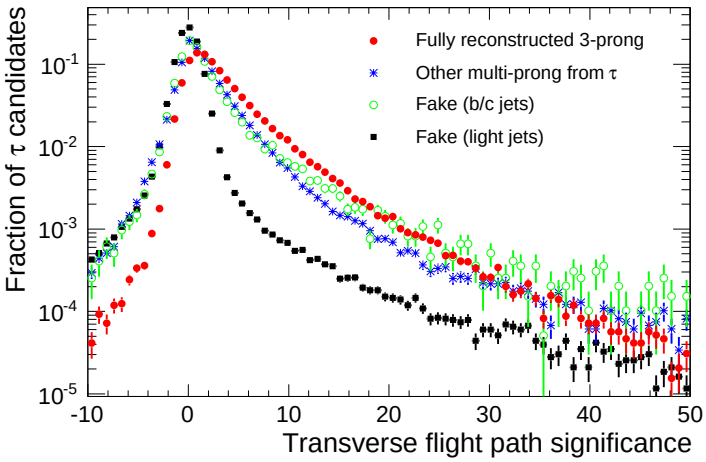

Figure 3.18: Significance of the transverse flight path for different categories of multi-prong τ candidates.

neural network. The layout of the network is based on an updated version of the neural network described in [32]. The artificial neural network is a feed-forward network with 2 hidden layers containing 30 nodes each and a single output node. The set of input variables is taken from the previous implementation of the neural network with minimal changes. Due to the similarity of the invariant mass of the track system for multi-prong τ candidates and the invariant mass of the τ candidate, the former quantity is removed from the list of input variables. For 1-prong τ candidates the significances of the impact parameters d_0 and $z_0 \sin(\theta)$ and for multi-prong candidates the transverse flight path significance are added. The unsigned impact parameter significances are used since at the time of the training the sign was not yet implemented. The additional input variables are used only if all quantities are available which are necessary for the calculation of the variables. A primary vertex is required for the calculation of both the impact parameters and the transverse flight path. A secondary vertex is required for the calculation of the transverse flight path. Separate neural networks with and without the impact parameter and transverse flight path significances are trained. Tau candidates are divided into 1-prong candidates with π^0 clusters, 1-prong candidates without π^0 clusters, 2-prong candidates and 3-prong candidates and neural networks are trained for each category. In total, 8 neural networks are trained.

The following input variables are common to all neural networks [22]. Unless indicated, all calorimetric quantities are calculated using cells within a cone of $\Delta R < 0.2$ around the seed track.

- Transverse energy of the τ candidate.
- Number of cells in the first electromagnetic calorimeter layer with a transverse energy above a certain threshold.
- Width of the transverse energy deposit in the first electromagnetic calorimeter layer calculated as the E_T-weighted variance

$$W_{strips} = \frac{\sum (\Delta\eta)^2 E_T}{\sum E_T} - \frac{\sum (\Delta\eta E_T)^2}{(\sum E_T)^2} \tag{3.4}$$

  where the difference in η is calculated with respect to the cell closest in η to the track at the first electromagnetic calorimeter layer.
- Transverse energy deposited in the area $0.1 < \Delta R < 0.2$ around the seed track taking into account all calorimeter layers divided by the transverse energy in a cone of $\Delta R < 0.2$ around the seed track.

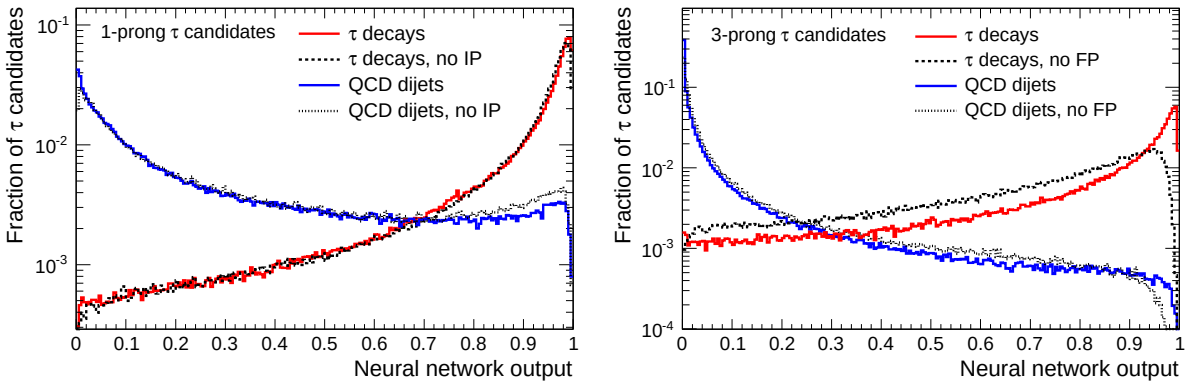

Figure 3.19: Neural network output for 1-prong (*left*) and 3-prong (*right*) τ candidates in $Z \to \tau^+\tau^-$, $W \to \tau\nu$ and QCD dijet events.

- Average ΔR with respect to the seed track of cells in the presampler and the first two layers of the electromagnetic calorimeter, the η strip and electromagnetic middle layers, weighted by the transverse energy deposited in the cells

$$R_{em} = \frac{\sum \Delta R \cdot E_T}{\sum E_T}. \tag{3.5}$$

- Transverse energy deposited in the back layer of the electromagnetic calorimeter and the hadronic calorimeter divided by the sum of the transverse momenta of the tracks.
- Transverse energy in the area $0.2 < \Delta R < 0.4$ around the seed track divided by the transverse energy in a cone of $\Delta R < 0.2$ around the seed track.
- Invariant mass of the τ candidate.
- Number of tracks in the area $0.2 < \Delta R < 0.4$ around the seed track.

For 1-prong candidates the following input variables are added if a primary vertex has been reconstructed:

- Transverse impact parameter significance $|d_0|/\sigma(d_0)$.
- Impact parameter significance in a plane containing the z axis $|z_0|\sin(\theta)/\sigma(z_0\sin(\theta))$.

For multi-prong candidates the following input variables are added:

- Width of the track system calculated in a way analogous to equation 3.5.
- Transverse flight path significance if a primary and secondary vertex are available and the secondary vertex passes the minimal requirement of a positive χ^2 and a positive number of degrees of freedom as discussed in the text.

The performance of the neural network is evaluated using versions of the datasets listed in table 3.2 reconstructed with release 14.2.25.8. Figure 3.19 shows the neural network output for 1-prong and 3-prong τ candidates in simulated $W \to \tau\nu$, $Z \to \tau^+\tau^-$ and QCD dijet events. The rejection of τ candidates from light jets that is achieved by a cut on the neural network output is shown in figure 3.20 as a function

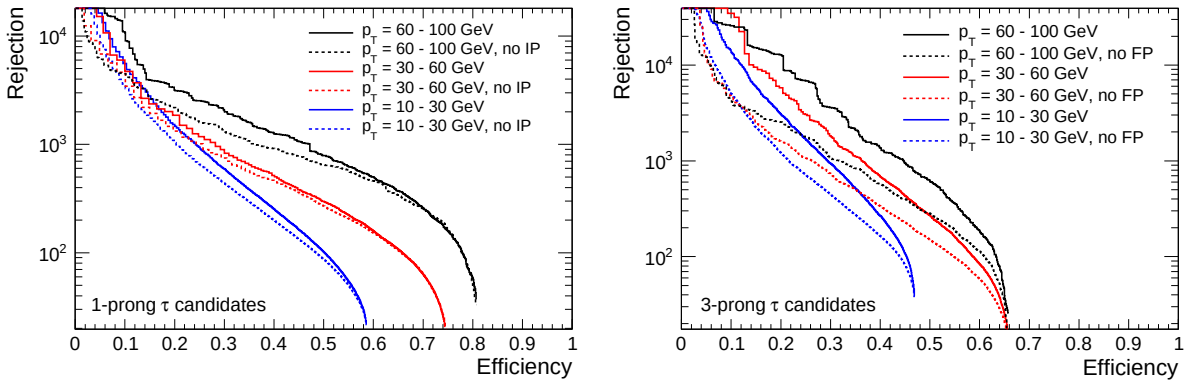

Figure 3.20: Rejection of light jets as a function of the efficiency for 1-prong (*left*) and 3-prong (*right*) τ decays in $W \rightarrow \tau\nu$ and QCD dijet events obtained by a cut on the neural network output variable.

Rejection at 30% Efficiency		1-prong	3-prong
$p_T =$ 10-30 GeV	with IP/FP	593 ± 13	942 ± 27
	without IP/FP	438 ± 9	451 ± 9
$p_T =$ 30-60 GeV	with IP/FP	897 ± 73	1827 ± 192
	without IP/FP	747 ± 54	740 ± 49
$p_T =$ 60-100 GeV	with IP/FP	2089 ± 331	3595 ± 723
	without IP/FP	1365 ± 173	1064 ± 117

Table 3.3: Rejection of τ candidates reconstructed from light jets at 30% efficiency for τ candidates from τ lepton decays obtained by a cut on the neural network output. Numbers are given for the full set of 8 neural networks and a reduced set of 4 neural networks not using the impact parameter and transverse flight path significances. Statistical errors due to the limited size of the Monte-Carlo datasets are given.

of the efficiency for τ candidates from τ lepton decays in $W \rightarrow \tau\nu$ events. The efficiency is calculated with respect to true 1-prong or 3-prong τ lepton decays. Only τ leptons are considered whose decay products are within the geometrical acceptance of the Inner Detector, which decay into at least one charged particle with a transverse momentum above 6 GeV and whose visible transverse momentum exceeds 10 GeV. The tracks of the reconstructed τ candidate are required to correspond to the charged particles from the τ decay and the track multiplicity of the τ candidate must be equal to the charged particle multiplicity of the τ decay. The rejection is calculated as the inverse of the efficiency of the selection of τ candidates from light jets minus one. The efficiency of the selection of fake τ candidates from light jets is calculated with respect to the truth jets reconstructed with the ATLAS cone algorithm [2] using as input the simulated visible hadronic final state particles excluding muons. Table 3.3 lists the rejection at 30% efficiency. The rejection is given for the full set of 8 neural networks and for the reduced set of 4 neural networks without the impact parameter and transverse flight path significances. For 1-prong decays an increase of the rejection of at least 20% is observed. For 3-prong decays an increase of more than a factor 2 is observed.

Chapter 4

Use of jet-vertex association for the central jet veto in the VBF $H \longrightarrow \tau^+\tau^-$ analysis

The production of a Standard Model Higgs boson in vector boson fusion at small Higgs boson masses at the LHC has a cross section approximately one order of magnitude below the cross section for the production of a Standard Model Higgs boson in gluon fusion as shown in figure 1.2. The ratio of the gluon fusion cross section to the vector boson fusion cross section decreases as the assumed Higgs boson mass increases and tends towards 1 at large Higgs boson masses close to 1 TeV as shown in figure 1.2. Hence, the vector boson fusion channel [33, 34] was originally considered only for the search at large Higgs boson masses [35]. By exploiting the hadronic structure of vector boson fusion events, the process was found to have a large expected signal significance also at small Higgs boson masses [19]. The prospects for the analysis with the ATLAS experiment were studied initially using a fast simulation [1] and more recently using a detailed simulation of the ATLAS detector [2]. For Higgs boson masses in the range 115 GeV to 135 GeV, vector boson fusion with the decay $H \rightarrow \tau^+\tau^-$ was found to be a possible discovery channel for a Standard Model Higgs boson with the ATLAS detector. The analysis is sensitive to pileup from additional minimum bias interactions [2]. In previous estimates of the signal significance pileup was not taken into account.

The datasets used in this chapter are listed in section 4.1. The original event selection optimized for the analysis in the absence of pileup is described in section 4.2. The expected effects of pileup are reviewed in section 4.5. A method for the improvement of the event selection in the presence of pileup is presented in sections 4.6 and 4.7. The method aims to identify jets not originating from the primary vertex of the main event and to discard them for the purpose of applying the central jet veto. The expected effects of the improved method on the vector boson fusion analysis is evaluated in section 4.8.

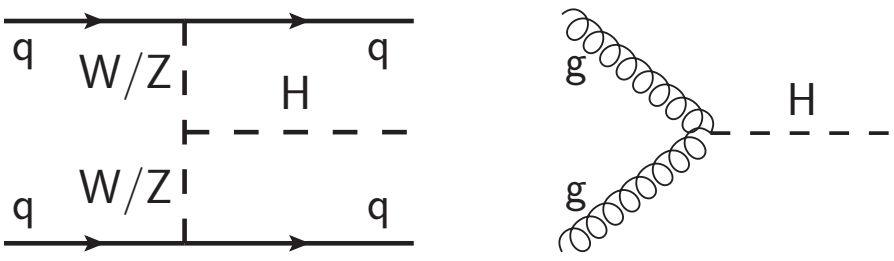

Figure 4.1: Feynman diagrams describing the production of a Higgs boson in vector boson fusion (*left*) and in gluon fusion (*right*) at a proton-proton collider.

4.1 Monte Carlo Datasets

The invariant $\tau^+\tau^-$ mass distributions after the event selection of the vector boson fusion analysis are calculated using VBF $H \to \tau^+\tau^-$ datasets generated with Herwig 6.510 [36] and $Z+2j$ and $Z+3j$ with $Z \to \tau^+\tau^-$ datasets generated with Alpgen [37] and Herwig. In the notation $Z+nj$, n denotes the number of cone jets with a cone radius of $\Delta R = 0.7$ reconstructed at the parton level after the parton showering that have a transverse energy above 20 GeV. The MLM matching procedure [38] is applied which requires the jets to correspond one-to-one to the partons generated by the matrix-element calculation. Purely electroweak production of $Z+2j$ and $Z+3j$ is not included. Tau decays are simulated with TAUOLA 2.7 [39] and PHOTOS 2.15 [40]. Multiple parton interactions are simulated with Jimmy 4.3 [41]. A GEANT4 [42] simulation of the ATLAS detector and the ATLAS digitization and reconstruction software are used to simulate the detector response. The datasets were generated for a center-of-mass energy of 14 TeV.

The performance of the jet-vertex association method and the efficiency of the central jet veto are evaluated using simulated VBF $H \to \tau^+\tau^-$, $Z+2j/3j$ (QCD) with $Z \to \tau^+\tau^-$ and $t\bar{t}$ events for a center-of-mass energy of 14 TeV and two different luminosity scenarios. The datasets for the $t\bar{t}$ process were generated with MC@NLO 3.1 [43] and Herwig. Minimum bias events were generated with Pythia 6.4 [44]. Datasets for a luminosity of $2 \cdot 10^{33}\,\mathrm{cm}^{-2}\mathrm{s}^{-1}$ with a bunch spacing of 25 ns, corresponding to an average number of 4.6 minimum bias interactions per bunch crossing, were simulated and digitized with ATLAS software release 12.0.7.1 and reconstructed with release 14.2.0.2. Datasets for a luminosity of $10^{33}\,\mathrm{cm}^{-2}\mathrm{s}^{-1}$ with a bunch spacing of 75 ns, corresponding to an average number of 6.9 minimum bias interactions per bunch crossing, were simulated and digitized with ATLAS software release 14.2.25.2 and reconstructed with release 14.2.25.8. The luminosity scenario with a bunch spacing of 75 ns is a special scenario for the early LHC operation. A dominant fraction of the dataset that may allow a first discovery of a Standard Model Higgs boson is currently expected to be taken at the nominal bunch spacing of 25 ns. The datasets for the scenario with a bunch spacing of 75 ns were simulated using minimum bias events which were generated for a center-of-mass energy of 10 TeV, hence the rate of additional high-p_T QCD interactions in those datasets is significantly smaller than that expected in a dataset with the same operation mode at a center-of-mass energy of 14 TeV. The discrimination power of the jet-vertex association method for the $t\bar{t}$ process is evaluated using a dataset simulated for a center-of-mass energy of 10 TeV. The dataset is simulated with pileup, corresponding to 4.6 interactions per bunch crossing at a bunch spacing of 25 ns.

Additional datasets of simulated Z and W production events are used for the evaluation of the primary vertex reconstruction and selection efficiencies. Datasets of $Z \to \mu^+\mu^-$ and $W \to e\nu$ events are used to study the performance of the primary vertex identification at an average number of 4.6 events per bunch crossing at a bunch spacing of 25 ns. The performance at the nominal luminosity which corresponds to 23 interactions per bunch crossing at a bunch spacing of 25 ns is evaluated using datasets of simulated $Z \to e^+e^-$, $W \to e\nu$ and $W \to \mu\nu$ events. All datasets used in this study are listed in table 4.1.

For brevity, the luminosity scenario corresponding to an average number of 4.6 interactions per bunch crossing at a bunch spacing of 25 ns will be referred to as luminosity scenario I in the following. The luminosity scenario corresponding to an average number of 6.9 interactions at a bunch spacing of 75 ns will be denoted luminosity scenario II.

4.2 Vector Boson Fusion $H \to \tau^+\tau^-$ in ATLAS

Figure 4.1 shows Feynman diagrams describing the production of a Higgs boson at a proton-proton collider in vector boson fusion and gluon fusion. The quarks participating in the vector boson fusion process are typically scattered at small angles to the beam. The jets initiated by the quarks are used to tag

Dataset	Process	$\sqrt{s}$ (TeV)	Luminosity scenario	Task ID	Events Used
005334	VBF $H \to \tau^+\tau^- \to lh$	14	–	7517	49 000
005334	VBF $H \to \tau^+\tau^- \to lh$	14	4.6 ev/bc, 25 ns	15067	44 819
205334	VBF $H \to \tau^+\tau^- \to lh$	14	–	58441, 58442	49 999
205334	VBF $H \to \tau^+\tau^- \to lh$	14	6.9 ev/bc, 75 ns	95136	48 323
205333	VBF $H \to \tau^+\tau^- \to ll$	14	–	56679, 56680	49 750
205333	VBF $H \to \tau^+\tau^- \to ll$	14	6.9 ev/bc, 75 ns	95134	41 491
005200	$t\bar{t}$	14	–	28350	539 387
005200	$t\bar{t}$	14	4.6 ev/bc, 25 ns	7554, 8990 8992, 8993 6786	106 149
205200	$t\bar{t}$	14	–	72511	997 340
205200	$t\bar{t}$	14	6.9 ev/bc, 75 ns	80893	957 113
105200	$t\bar{t}$	10	4.6 ev/bc, 25 ns	41348	50 000
208162	$Z+2j, Z \to \tau^+\tau^-$	14	–	75186	327 983
208162	$Z+2j, Z \to \tau^+\tau^-$	14	6.9 ev/bc, 75 ns	76984	310 745
208163	$Z+3j, Z \to \tau^+\tau^-$	14	–	78311	282 197
208163	$Z+3j, Z \to \tau^+\tau^-$	14	6.9 ev/bc, 75 ns	78372	281 447
206129	$Z+2j, Z \to \tau^+\tau^- \to ll$	14	–	76975	338 748
206130	$Z+3j, Z \to \tau^+\tau^- \to ll$	14	–	77623	217 011
106031	$W^- \to e\nu$	10	4.6 ev/bc, 25 ns	80129, 80130	948 088
106051	$Z \to \mu^+\mu^-$	10	4.6 ev/bc, 25 ns	78911, 78912 78914, 78917	745 810
005001	Minimum Bias	14	–	23536	100 000
106043	$W \to e\nu$	14	23 ev/bc, 25 ns	105324	10 000
106043	$W \to \mu\nu$	14	23 ev/bc, 25 ns	105323	10 000
106046	$Z \to ee$	14	23 ev/bc, 25 ns	101032	10 000
005001	Minimum Bias	14	–	4278	100 000
007903	Cavern Background	–	–	6304	10 000

Table 4.1: Monte Carlo datasets used for the vector boson fusion analysis and the study of jet-vertex association and the central jet veto in the presence of pileup. A Higgs boson mass of 120 GeV is assumed. The $t\bar{t}$ dataset 005200 for a luminosity corresponding to 4.6 events per bunch crossing at 25 ns bunch spacing was digitized with release 12.0.7.1 using the minimum bias and cavern background datasets 005001 and 007903. The $t\bar{t}$ dataset 005200 and the VBF dataset 005334 were reconstructed with release 14.2.0.2 with additional tags applied to treat known problems in the reconstruction.

vector boson fusion events. Since no color is exchanged between the quarks, QCD radiation is expected only in the direction between the scattered quark and the beam. This signature allows an additional discrimination against background processes that is not possible in the gluon fusion process. At leading order, the gluon fusion process contains no tagging jets. Since gluon fusion is a QCD process, radiation similar to the majority of background processes which are also QCD processes is expected.

The jet topology in vector boson fusion and $t\bar{t}$ events is illustrated in figure 4.2, which shows the η distribution of the jet with the largest transverse momentum in an event and the difference in η between the tagging jets.

The signature that is selected in the vector boson fusion analysis consists of two tagging jets with a large separation in η, the absence of hadronic activity in η between the tagging jets, two isolated leptons, where each lepton can be either an electron or a muon, or an isolated lepton and a hadronic τ candidate in the central detector region between the tagging jets, and a reconstructed mass of the $\tau^+\tau^-$ lepton pair close to the Higgs boson mass. The event selection is based on [2] with minimal changes.

4.2.1 Electron reconstruction

Electrons are reconstructed starting from clusters in the electromagnetic calorimeter with a fixed size of 3×7 cells in the η and ϕ directions in the electromagnetic middle layer corresponding to a size of $\Delta\eta \times \Delta\phi = 0.075 \times 0.175$. The cluster width in the ϕ direction is chosen to be larger to collect contributions from soft bremsstrahlung photons radiated in front of the calorimeter. Clusters of a fixed size rather than topological clusters as described in section 5.1 may be used due to the compactness and homogeneity of purely electromagnetic showers. An advantage of clusters with a fixed size is that the energy of the clusters is not intrinsically biased by pileup as discussed in chapter 5. An electron candidate is formed if an Inner Detector track which is not identified as originating from a conversion electron is matched to the electromagnetic cluster in a window of $\Delta\eta \times \Delta\phi = 0.05 \times 0.10$ and E/p is less than 10, where E denotes the energy of the cluster and p the momentum of the track.

Here, electrons are required to pass the "medium" electron cuts which are defined as:

- The electron cluster is required to match the track within $|\Delta\eta| < 0.1$.
- The track must have at least one hit in the Pixel Detector.
- The track must have at least seven hits in the silicon detectors.
- The track must have a transverse impact parameter with an absolute value of less than 5 mm.
- The energy-weighted barycenter of the cluster in the electromagnetic middle layer must be found within $|\eta| < 2.47$.
- η and E_T dependent cuts on the ratio of the transverse energy reconstructed in the hadronic calorimeter to the transverse energy of the electromagnetic cluster are applied.
- For the electromagnetic middle layer, η and E_T dependent cuts on the shower width and the ratio of the energy in a 3×7 window to the energy in a 7×7 window are applied. The energy in a 7×7 window is required to be positive.
- If the fraction of the cluster energy deposited in the electromagnetic front layer, the η strip layer, exceeds 0.5% and the energy-weighted barycenter of the cluster in the electromagnetic middle layer is found within $1.52 < |\eta| < 2.37$ or $|\eta| < 1.37$, η and E_T dependent cuts on the width of the energy deposit and the difference between the first and second maxima in the η strip layer are applied.

4.2.2 Muon reconstruction

Muons reconstructed by the Staco algorithm [2] are used in the vector boson fusion analysis. Tracks are reconstructed separately in the muon spectrometer and the Inner Detector. The tracks are extrapolated to the interaction region and a χ^2-based matching between the Inner Detector and muon spectrometer tracks is performed. Combined muon objects are created for pairs of matching tracks. Track parameters for the combined muon objects are obtained from a statistical combination analogous to an error-weighted average of the track parameters of the Inner Detector and muon spectrometer tracks.

4.2.3 Jet reconstruction and calibration

The analyses presented in this thesis were developed using jets reconstructed with the ATLAS seeded cone algorithm. Topological clusters [45] of calorimeter cells are used as the input objects. The clusters are formed by connecting cells based on the energy deposited in them and have a variable size and shape. The cluster formation is discussed in section 5.1. The ATLAS seeded cone algorithm is seeded by clusters with a transverse energy above 1 GeV. For each seed a jet axis is determined by calculating the sum of the momenta of all clusters included in a circle in the η-ϕ plane of a fixed radius around the seed cluster. The jets used in this study are created with a radius of 0.4. The direction of the cluster is determined during the cluster formation as the absolute-energy weighted mean of the cell directions. The determination of the jet axis is iterated using the clusters in a cone around the current jet axis until the distance between the updated jet axis and the current jet axis is smaller than a cut value of $\Delta R = 0.05$ that defines the stability of a cone or a maximum number of iterations is reached. Cones that are not stable are discarded. The reconstruction of stable cones is followed by a split and merge step to resolve ambiguities in the case of overlapping cones. If the transverse energy shared between two cones is larger than 50% of the transverse energy of the jet with the smaller transverse energy the jets are merged. Otherwise, the jets are split with shared clusters being assigned to the jet that is geometrically closer to the cluster. Jets are required to have a transverse energy above 7 GeV.

Seeded cone algorithms are known to be infrared and collinear unsafe [46]. Recently, the AntiKt algorithm [47] has been adopted as the algorithm recommended for ATLAS physics analyses which is both infrared and collinear safe. Jets reconstructed with the AntiKt algorithm generally have a circular shape in the η-ϕ plane. The AntiKt algorithm begins with a calculation of the distance measures

$$d_{ij} = \min\left(k_{t,i}^{-2}, k_{t,j}^{-2}\right) \frac{\Delta_{ij}^2}{R^2} \tag{4.1}$$

between pairs of input objects (i, j) with transverse momenta $k_{t,i}$ and $k_{t,j}$ and

$$d_{iB} = k_{t,i}^{-2} \tag{4.2}$$

between each input object and the beam. $\Delta_{ij} = \sqrt{(\Delta y)^2 + (\Delta\phi)^2}$ is the distance between objects i and j in the y-ϕ plane with the rapidity y and the azimuth ϕ. R is a parameter that defines the radius of the jet. Objects i and j are clustered if d_{ij} is the minimal distance. If the minimal distance is d_{iB}, object i is added to the list of jets and removed from the list of input objects. The procedure is iterated until the list of input objects is empty. The resulting jets typically have a radius R in the η-ϕ plane. In this study, topological clusters of calorimeter cells are used as the input objects.

The response of the ATLAS calorimeters to electromagnetic and hadronic particle showers is different. On average, the energy reconstructed for a hadronically interacting particle is smaller than the energy reconstructed for an electron or photon of the same energy. The calorimeter is calibrated in a way such that the energy for electrons is reconstructed correctly on average [48, 49]. For hadronic particles and jets an additional calibration is applied during the offline reconstruction. Methods implemented in

the ATLAS software attempt to identify electromagnetic and hadronic shower components and apply weights to correct the hadronic component such that the reconstructed energy is equal on average to the energy of the particles entering the calorimeter. For the standard reconstruction of jets, currently two methods are used in the ATLAS software, a cell-energy weighting method previously used at the H1 experiment [2] and a cluster-level calibration method called local hadronic calibration [50].

In the H1-style calibration, weights are applied after the jet finding to the energies reconstructed in cells that form the jet constituents, which may be either calorimeter towers or topological clusters. The weights are functions of the cell energy density and the cell position. The dependence of the weights on the energy density is motivated by the observation that energy deposits with a low energy density are more likely to originate from the hadronic component of a shower.

In the local hadronic calibration, topological clusters are classified by their shape, position and the structure of the energy deposit as hadronic or electromagnetic clusters. Weights similar to the weights applied in the H1-style calibration are applied to the energies of cells in hadronic clusters. A correction for energy not included in the cluster is applied. In this method, the calibrated clusters are used as the input to the jet reconstruction.

At the jet level, both methods yield comparable results. After the calibration, additional corrections are applied at the jet level to correct for particles not reaching the calorimeter and for inefficiencies of the jet-finding algorithm.

4.2.4 Event selection for the channel $H \rightarrow \tau^+\tau^- \rightarrow ll$

- Events are required to pass the single electron or muon trigger with a transverse momentum above approximately 20 GeV (EF_e20_loose or EF_mu20).

- An electron with a transverse momentum above 25 GeV or a muon with a transverse momentum above 20 GeV is required. Both leptons must be found in the central detector region within $|\eta| < 2.7$. The electron candidate must have been reconstructed by the standard electron reconstruction algorithm [2], indicated by value of the author variable assigned to the electron candidate of 1 or 3. In addition, the electron must satisfy the "medium" selection cuts as described in section 4.2.1. Only isolated electrons are selected by requiring the ratio of the energy in a cone with a radius of $\Delta R = 0.2$ around the electron cluster, excluding the energy deposited in the electromagnetic calorimeter in a window with a size given by 5×7 cells in the middle layer and excluding energy deposited in the TileGap3 scintillator, to the transverse momentum of the electron track to be smaller than 0.1 (etcone20$/p_T < 0.1$).

  The muon must have been reconstructed as a combined muon by the Staco algorithm [2]. The χ^2 of the combined muon track must be smaller than 500 (fitChi2 < 500) and the difference between the χ^2 of the combined muon track and the sum of the χ^2 of the Inner Detector and muon spectrometer tracks must be smaller than 100 (matchChi2 < 100). Only isolated muons are selected by requiring the ratio of the energy in a cone with a radius of $\Delta R = 0.2$ around the muon, excluding the energy deposited by the muon itself, to the transverse momentum of the muon to be smaller than 0.1 (etcone20$/p_T < 0.1$).

- The total number of leptons must be 2 and the leptons must have opposite charges. Leptons are selected according to the above criteria, however the transverse momentum threshold is lowered for the second lepton to 15 GeV for electrons and to 10 GeV for muons. Electrons found within $\Delta R < 0.2$ of a selected muon are discarded.

- The missing transverse energy must exceed 40 GeV.

- The fraction of the τ lepton momentum carried by each lepton as calculated from the lepton momenta and the missing transverse energy [2] has to be positive and smaller than 0.75. The angle between the lepton momenta is required to satisfy $|\cos(\Delta\phi)| < 0.9$.

- At least 2 jets with a transverse momentum above 20 GeV within $|\eta| < 4.8$ are required. At least one jet must have a transverse momentum above 40 GeV. Jets reconstructed with the ATLAS cone algorithm using a cone size of $\Delta R = 0.4$ are used. Jets within $\Delta R < 0.2$ of a selected muon or electron are discarded.

- The two tagging jets, which are selected as the jets with the largest transverse momenta, must be found in opposite detector hemispheres.

- The leptons must be found between the tagging jets in the η direction.

- The tagging jets must not have been identified as *b*-jets. The IP3D + SV1 *b*-tagger [2] is used, which combines impact parameter information with topological information of a reconstructed secondary vertex. A jet is considered a *b*-jet if the weight returned by the *b*-tagging algorithm is larger than 1.

- The tagging jets must be separated in η by at least 4.4.

- The tagging jets must have an invariant mass above 700 GeV.

- Events are rejected if a jet is found within $|\eta| < 3.2$ which is not a tagging jet.

- For a calculation of the signal significance based purely on the numbers of selected events, the invariant mass of the $\tau^+\tau^-$ lepton pair reconstructed from the τ decay products and the missing transverse energy is required to be within 15 GeV of the Higgs boson mass for a given mass hypothesis. This cut is not applied in the standard analysis in which the signal significance is calculated using a fit to the reconstructed $\tau^+\tau^-$ mass spectrum as discussed below.

4.2.5 Event selection for the channel $H \to \tau^+\tau^- \to lh$

- The same trigger requirement as in the dilepton channel is used.

- A lepton passing the same selection as in the lepton-lepton channel with the high transverse momentum thresholds is required.

- No additional leptons passing the same selection as in the lepton-lepton channel with the reduced transverse momentum thresholds are allowed.

- A hadronic τ candidate with a transverse momentum above 30 GeV is required. The τ candidate must have 1 or 3 tracks and a charge of 1 or -1. The charge must be opposite to the charge of the lepton. The τ candidate must pass the "medium" likelihood cut and the "medium" electron veto and the muon veto cuts. Tau candidates found within $\Delta R < 0.2$ of a selected lepton are discarded. The number of selected τ candidates must be 1.

- A missing transverse energy above 30 GeV is required.

- The transverse mass of the lepton and the missing transverse energy, $m_T = \sqrt{2 p_T^{lep} E_{\mathrm{T}}^{\mathrm{miss}} \cdot (1 - \cos\Delta\phi)}$, must be below 30 GeV.

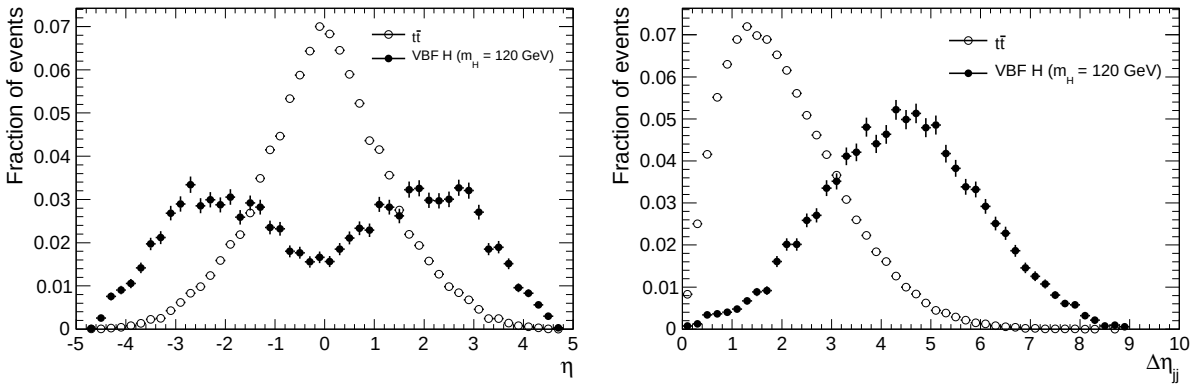

Figure 4.2: Pseudorapidity of the jet with the largest transverse momentum (*left*) and difference in η between the jets selected as tagging jets (*right*) in simulated vector boson fusion and $t\bar{t}$ events in the lepton-hadron channel after a preselection requiring a lepton and two tagging jets in opposite detector hemispheres.

- The fraction of the τ momentum carried by the lepton must be positive and smaller than 0.75. The fraction of the momentum of the other τ lepton carried by the hadronic τ decay products must be positive and smaller than 1. The angle between the lepton and the hadronic τ candidate must satisfy $|\cos(\Delta\phi)| < 0.9$.
- The event selection based on the tagging jets is the same as in the lepton-lepton channel with the single exception that no *b*-tag veto is applied.

Figure 4.3 shows the expected distribution of the reconstructed invariant mass of the $\tau^+\tau^-$ lepton pair for an integrated luminosity of $30\,\text{fb}^{-1}$ in the lepton-lepton and lepton-hadron channels for signal events and the background process $Z+2j/3j, Z \to \tau^+\tau^-$ (QCD). The cross section for the signal process is taken from [2]. The cross sections for the $Z+2j$ and $Z+3j$ processes are taken from the generators Alpgen and Herwig. A factor of 1.24 to correct the leading-order generator result to a next-to-next-to-leading-order result as discussed in [51] is applied. Only the dominant $Z+jets$ background is shown due to a lack of Monte Carlo statistics for the other background processes. The expected signal significance taking into account all background processes for an integrated luminosity of $30\,\text{fb}^{-1}$ determined from a likelihood ratio from a fit [2] is shown in figure 4.4. At a Higgs boson mass of 120 GeV, an expected signal significance of 4.85 is obtained by combining the results in the lepton-lepton and lepton-hadron channels. The effects of pileup are not taken into account in this estimate.

4.3 Simulation of minimum bias interactions

The total cross section for proton-proton collisions at a center-of-mass energy of 14 TeV is approximately 100 mb. Figure 4.5 shows values of the cross section measured at the ISR[1] and a cosmic air shower experiment [52] as a function of the center-of-mass energy and the results of a fit and model predictions. The expected values for the total cross section at the LHC derived from the data are $111.5 \pm 1.2^{+4.1}_{-2.1}$ mb at 14 TeV and $105.1 \pm 1.1^{+3.6}_{-1.9}$ mb at 10 TeV [53, 54].

Additional interactions taking place close in time to the triggered bunch crossing will affect the signal reconstructed in the detector. This effect is called pileup. The effect of additional proton-proton interac-

[1] Intersecting Storage Rings

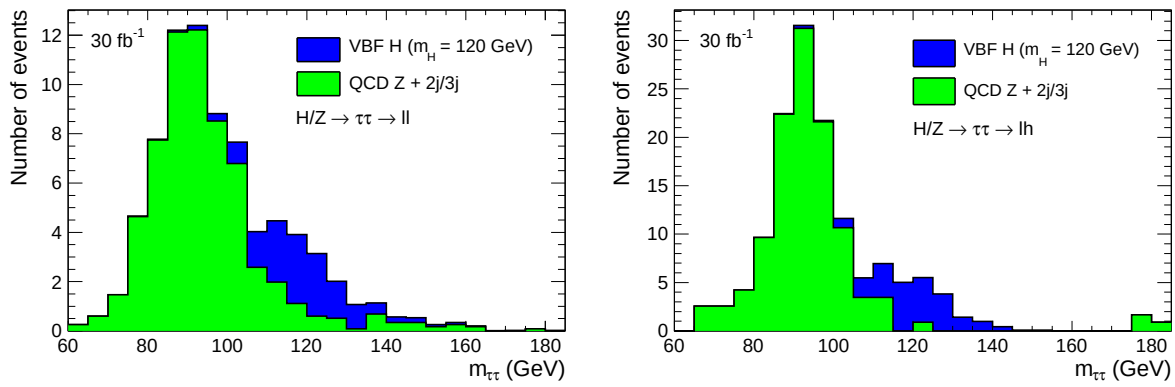

Figure 4.3: Invariant mass of the $\tau^+\tau^-$ lepton pair in the lepton-lepton channel (*left*) and the lepton-hadron channel (*right*) normalized to an integrated luminosity of $30\,\mathrm{fb}^{-1}$ for simulated signal and $Z+2j/3j$ (QCD) events.

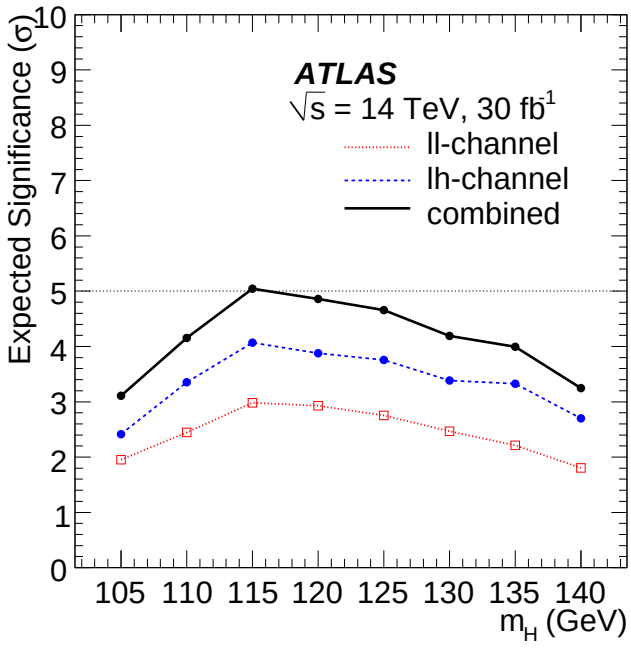

Figure 4.4: Expected signal significance for a Standard Model Higgs boson produced in vector boson fusion decaying into a $\tau^+\tau^-$ lepton pair for an integrated luminosity of $30\,\mathrm{fb}^{-1}$ as a function of the Higgs boson mass. [2] The estimate does not take into account pileup.

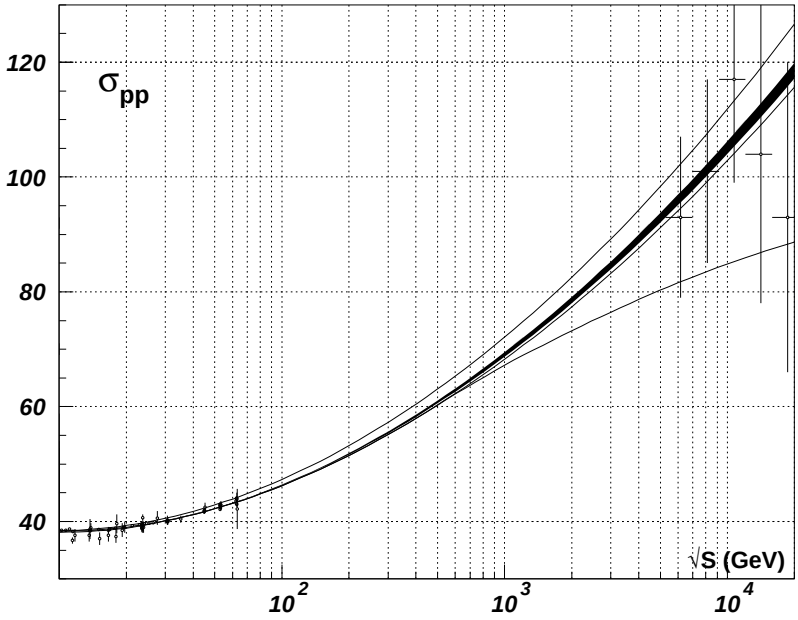

Figure 4.5: Total cross section for proton-proton scattering as a function of the center-of-mass energy measured at the ISR (*low center-of-mass energy*) and a cosmic air shower experiment (*high center-of-mass energy*). Fit results including the statistical errors are shown as a black band. Two curves close to the band show the sum of statistical and systematic errors. Two additional curves at a larger distance from the band show model uncertainties considered in [54].

tions is taken into account in the simulation by overlaying the main proton-proton collision event with the signal from additional minimum bias interactions taking place close in time to the main interaction. Experimentally, minimum bias interactions may be defined as proton-proton interactions triggered by a minimum bias trigger and not triggered by a high-p_T trigger. A minimum bias trigger, which may be a combination of several independent triggers, typically requires a minimum amount of activity in the detector that is sufficient to indicate that a proton-proton interaction has taken place. For the purpose of the simulation, minimum bias interactions are commonly defined as non-single diffractive inelastic proton-proton interactions. For this study, minimum bias interactions simulated with Pythia [44] are used. The simulation includes non-diffractive inelastic proton-proton collisions and high-p_T QCD interactions. The total cross section of the process is 51.6 mb at 10 TeV and 54.7 mb at 14 TeV. The difference with respect to the total proton-proton scattering cross section is given by the cross section for diffractive and elastic scattering.

The cross section predicted by Pythia for QCD dijet production with a transverse parton momentum above 17 GeV is 0.926 mb at 10 TeV and 1.48 mb at 14 TeV. Hence, this process is expected to constitute approximately 1.8% of the simulated minimum bias events at 10 TeV and 2.7% at 14 TeV. At 10^{34} cm^{-2} s^{-1}, QCD dijet production with a transverse parton momentum above 17 GeV can be expected to occur in between 40% and 50% of all bunch crossings. In this study, lower luminosities are considered which lead to average numbers of between 2.3 and 6.9 interactions per bunch crossing. At those luminosities, the QCD dijet process with a transverse parton momentum above 17 GeV may be expected to contribute to between 5% and 15% of all bunch crossings.

The expected charged particle multiplicity in minimum bias events at a center-of-mass energy of 14 TeV as a function of η and p_T is shown in figure 4.6. In the central detector region, between 4 and 10 charged particles per unit of η are expected approximately. The neutral particle multiplicity

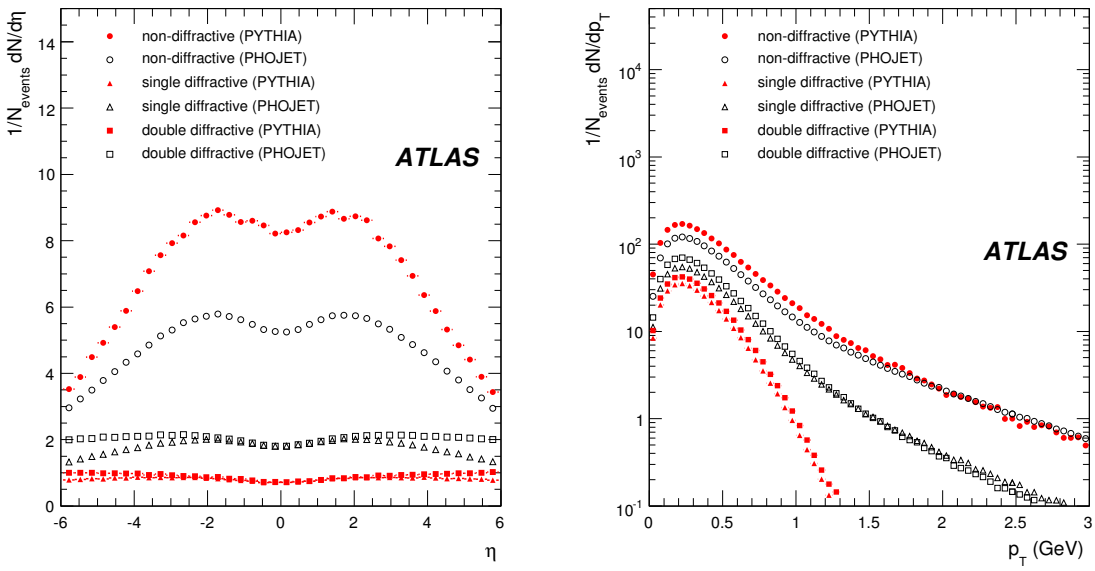

Figure 4.6: Multiplicity of stable charged particles in simulated minimum bias events for a proton-proton collider at a center-of-mass energy of 14 TeV as a function of η (*left*) and p_T (*right*). [2].

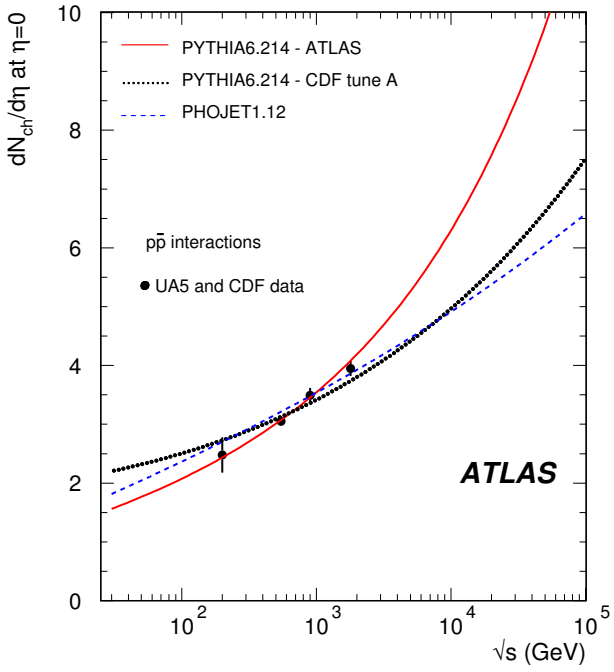

Figure 4.7: Multiplicity of stable charged particles at $\eta = 0$ measured at the SPS and the Tevatron and the extrapolation to the nominal center-of-mass energy of the LHC using Pythia with two different sets of parameters and Phojet. [2]

after π^0 decays is approximately equal to the charged particle multiplicity [48]. Figure 4.7 shows the total charged particle multiplicity measured at the SPS[2] and the Tevatron as a function of the center-of-mass energy. Also shown are extrapolations of the total charged particle multiplicity to the nominal center-of-mass energy of the LHC using Pythia with two different sets of parameters and Phojet [55]. The extrapolations have a large uncertainty and the charged particle multiplicity will be one of the first measurements at the LHC.

4.4 Simulation of pileup

Pileup is simulated by overlaying the hits from the GEANT4 [42] simulation of the primary proton-proton interaction with the hits from additional events. The dominant contribution is given by minimum bias events. In addition, small numbers of interactions of outlying protons with parts of the detector or a collimator and interactions of protons with gas present in the beam pipe are added. For each bunch crossing in the time interval of sensitivity of the ATLAS detector around the triggered bunch crossing, a number of events distributed randomly according to a Poisson distribution for the expected average number of events at the given luminosity is selected from datasets of simulated single events. The simulated hits are passed to the digitization algorithms for all subdetectors that are sensitive to the given bunch crossing. Interactions from radiation background in the cavern for the selected luminosity are added at a constant rate. For each bunch crossing, the same number of cavern background events is selected randomly from a dataset of simulated cavern background events. The events are assigned a time offset within the bunch crossing such that events are distributed uniformly over time. The subdetector digitization algorithms simulate the detector response and produce a signal which can be used by the reconstruction.

The subsystems of the Inner Detector are sensitive to interacting particles in a small time window around the triggered bunch crossing. The Pixel Detector is currently operated with a readout interval of $[-2,2]$ bunch crossings. A reduction of the readout interval to $[-1,+1]$ bunch crossings at low luminosity and intermediate luminosities is foreseen. At the nominal luminosity, the readout interval will include only the triggered bunch crossing [56]. The SCT is expected to be operated in a mode in which 3 bunch crossings are read out and the absence of a hit in the bunch crossing preceding the triggered bunch crossing followed by a hit in the triggered bunch crossing will be required. The TRT will operate in a mode in which 3 consecutive bunch crossings are read out. Since the TRT signal has a length of up to 60 ns the detector will be sensitive to up to two additional bunch crossings preceding and following the readout window. The time resolution of the detector will allow a discrimination between hits in different bunch crossings.

The signals of the liquid argon calorimeters have different lengths depending on the width of the liquid argon gap, the voltage and the electrode structure. Signals in the forward calorimeter are relatively short with a drift time in the first FCal module of 60 ns, and longer drift times in the second and third modules as expected from the increased width of the liquid argon gaps. In the electromagnetic endcap, the signal length increases with the radius as the width of the liquid argon gap increases. The maximum signal length in the LAr calorimeters is 800 ns which corresponds to 32 bunch crossings. The signal is sampled in 5 bunch crossings starting with the triggered bunch crossing. Hence, the detectors are sensitive to an interval of $[-32,5]$ bunch crossings. Signals in the tile calorimeter are shorter. Seven bunch crossings are sampled. The detector is sensitive to an interval of $[-8,7]$ bunch crossings.

The RPCs of the muon spectrometer are sensitive to a single bunch crossing. The TGCs will operate in a mode in which three consecutive bunch crossings are read out. The detectors are sensitive to hits from collisions in an interval of $[-2,4]$ bunch crossings. The CSCs are sensitive to an interval of approximately

[2] Super Proton Synchrotron

Subdetector	Sensitive interval (25 ns)
Pixel (high $\mathscr{L}$)	[-1,1]
Pixel (low $\mathscr{L}$)	[-2,4]
SCT	[-2,1]
TRT	[-2,2]
LAr EM	[-31,5]
LAr HEC	[-28,5]
LAr FCAL	[-23,5]
Tile	[-8,6]
TGC	[-2,3]
CSC	[-3,3]
RPC	[-4,4]
MDT	[-32,32]

Table 4.2: Interval of sensitivity of individual subdetectors used in the digitization of simulated pileup datasets.

$[-15,4]$ bunch crossings. The MDTs have the longest signals and readout time and are sensitive to an interval of $[-32,32]$ bunch crossings.

Table 4.2 summarizes the time intervals currently used for the digitization of simulated data with pileup.

4.5 Effects of pileup on the analysis

The discovery of a Standard Model Higgs boson at small Higgs boson masses in the vector boson fusion process is expected to require an integrated luminosity of approximately $30\,\text{fb}^{-1}$. The dataset will be composed of data taken at different luminosities during the initial years of LHC operation while the luminosity will be increased gradually to the design luminosity of 10^{34} cm^{-2} s^{-1}. The analysis of the vector boson fusion process will be affected in several ways by the presence of pileup. The calorimeter-based discriminating observables used for the identification of hadronic τ decays are known to be sensitive to pileup. The resolution of the missing transverse energy measurement is degraded in the presence of pileup which will affect the resolution of the invariant mass of the $\tau^+\tau^-$ lepton pair. Finally, the central jet veto will be affected by additional jets reconstructed in the calorimeter not originating from the primary interaction.

Additional jets affecting the efficiency of the central jet veto are expected from QCD dijet production in the same bunch crossing as the triggered event as discussed in section 4.3. The number of jets in the primary event passing a fixed transverse energy threshold is expected to increase due to a degradation of the jet energy resolution. In addition, a positive bias of the jet energy is introduced by the current cluster formation as is discussed in detail in chapter 5. The efficiency of the central jet veto for different luminosity scenarios is shown in figure 4.8.

4.6 Primary Vertex Selection

Figure 4.9 shows the residual of the z coordinate of the primary vertex in simulated $t\bar{t}$, $H \to \tau^+\tau^- \to lh$ and minimum bias events without pileup. The residual distribution for single minimum bias events has a

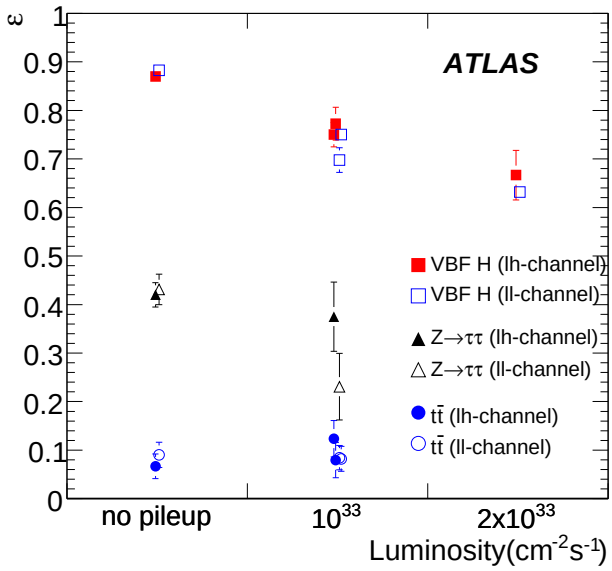

Figure 4.8: Efficiency [2] of the central jet veto in the vector boson fusion $H \to \tau^+\tau^-$ analysis for three different luminosity scenarios at a bunch spacing of 25 ns.

σ from a Gaussian fit of 82 μm. The tails deviate significantly from a Gaussian shape. The distributions for vector boson fusion $H \to \tau^+\tau^- \to lh$ and $t\bar{t}$ events have Gaussian widths of 52 μm and 34 μm, respectively.

From the list of reconstructed primary vertices, the primary vertex of the main interaction is identified by the primary vertex reconstruction algorithm as the vertex with the maximum value of $\sqrt{N}\sum p_T^2$, where the sum is taken over all N tracks assigned to the vertex. In $t\bar{t}$ events the primary interaction vertex is reconstructed and identified correctly by this method in almost all cases. In $H \to \tau^+\tau^- \to lh$ events there is a significant fraction of events in which the primary interaction vertex is either not reconstructed or not identified correctly. The identification efficiency, defined here as the fraction of all events in which the selected primary vertex candidate has a distance in the z direction from the true primary vertex of less than 300 μm, is 99.7% in $t\bar{t}$ events and 94.7% in $H \to \tau^+\tau^- \to lh$ events.

In physics analyses of processes including charged particles with a large transverse momentum the tracks associated with the high-p_T objects provide additional information on the position of the primary interaction vertex. In particular, the impact parameter z_0 of the lepton tracks in the $H \to \tau^+\tau^- \to lh$ and $H \to \tau^+\tau^- \to \ell^+\ell^-$ analyses may be used for the primary vertex selection. Figure 4.10 shows the z_0 of the reconstructed electron or muon with respect to the true primary vertex in $H \to \tau^+\tau^- \to lh$ events. The distributions are wider than the distribution of the z coordinate residual of the reconstructed primary vertex which is shown for comparison. Due to the flight path of the τ lepton the z_0 distributions have non-Gaussian tails.

After requiring a lepton trigger and a reconstructed lepton, the significance of the z_0 of the lepton with respect to the true primary vertex, which is defined as the value divided by its estimated error, is smaller than 20 in 99.9% of all $H \to \tau^+\tau^- \to lh$ events in luminosity scenario I. The significance of the distance in the z direction between the true primary vertex and the selected reconstructed primary vertex candidate is smaller than 20 in 95.7% of events after the same preselection and using the standard method for the primary vertex selection.

The primary vertex selection is extended to use the z_0 of a reconstructed lepton according to the

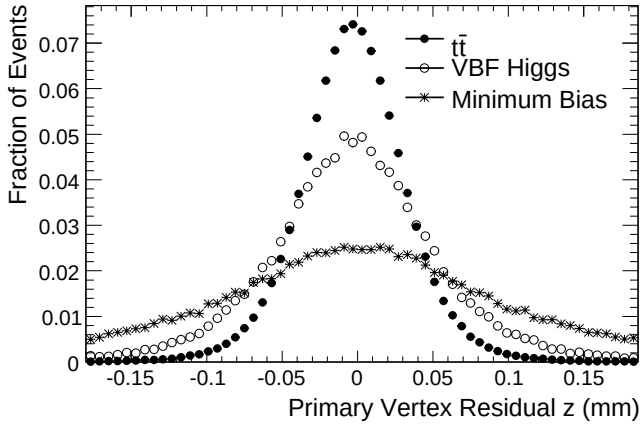

Figure 4.9: Residual of the z coordinate of the primary vertex position in $t\bar{t}$, $H \to \tau^+\tau^- \to lh$ and minimum bias events.

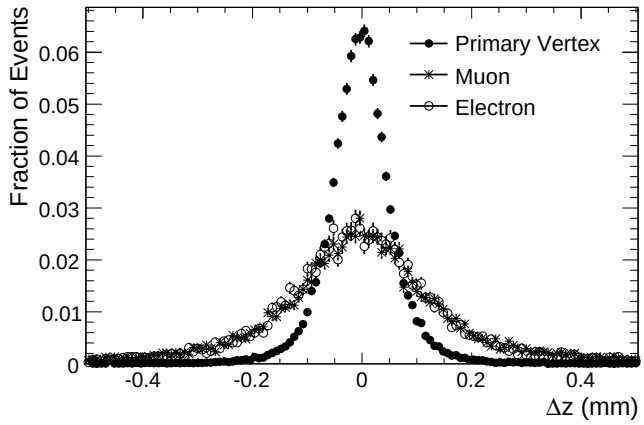

Figure 4.10: Impact parameter z_0 of the reconstructed muon or electron with respect to the true primary vertex in $H \to \tau^+\tau^- \to lh$ events with pileup. The z residual of the primary vertex is shown for comparison.

Process	Reconstruction	Standard Selection	Lepton-based Selection
4.6 ev/bc, 25 ns			
$t\bar{t}$	$(99.91 \pm 0.01)\%$	$(99.79 \pm 0.02)\%$	$(99.90 \pm 0.02)\%$
$W^- \to e\nu$	$(92.64 \pm 0.04)\%$	$(79.67 \pm 0.07)\%$	$(92.14 \pm 0.05)\%$
$Z \to \mu^+\mu^-$	$(96.74 \pm 0.03)\%$	$(90.90 \pm 0.04)\%$	$(96.30 \pm 0.03)\%$
VBF $H \to \tau^+\tau^- \to lh$	$(97.38 \pm 0.14)\%$	$(95.11 \pm 0.19)\%$	$(97.34 \pm 0.14)\%$
6.9 ev/bc, 75 ns			
$t\bar{t}$	$(99.79 \pm 0.01)\%$	$(99.04 \pm 0.02)\%$	$(99.58 \pm 0.01)\%$
$Z + 2j, Z \to \tau^+\tau^-$	$(99.07 \pm 0.03)\%$	$(95.43 \pm 0.07)\%$	$(98.35 \pm 0.05)\%$
$Z + 3j, Z \to \tau^+\tau^-$	$(99.49 \pm 0.03)\%$	$(97.58 \pm 0.06)\%$	$(98.96 \pm 0.04)\%$
VBF $H \to \tau^+\tau^- \to lh$	$(92.99 \pm 0.21)\%$	$(87.47 \pm 0.28)\%$	$(92.23 \pm 0.23)\%$
VBF $H \to \tau^+\tau^- \to ll$	$(95.03 \pm 0.13)\%$	$(94.48 \pm 0.14)\%$	$(94.50 \pm 0.14)\%$
23 ev/bc, 25 ns			
$W \to e\nu$	$(80.17 \pm 0.01)\%$	$(57.19 \pm 0.01)\%$	$(78.63 \pm 0.01)\%$
$W \to \mu\nu$	$(81.56 \pm 0.01)\%$	$(64.02 \pm 0.01)\%$	$(80.26 \pm 0.01)\%$
$Z \to e^+e^-$	$(81.60 \pm 0.01)\%$	$(60.35 \pm 0.01)\%$	$(79.91 \pm 0.01)\%$

Table 4.3: Primary vertex reconstruction and identification efficiencies. The reconstruction efficiency is defined as the fraction of events in which at least one primary vertex candidate is reconstructed within 300 μm in the z direction of the true primary vertex. The selection efficiency is defined as the fraction of events where the selected primary vertex candidate is found within 300 μm of the true primary vertex.

following method:

- The list of primary vertex candidates is initialized by the primary vertex reconstruction algorithm using the standard procedure. The primary vertex candidates are sorted in order of decreasing $\sqrt{N}\sum p_T^2$ with the sum taken over all N tracks assigned to the vertex.
- For each candidate, the weight $\sum p_T/(z_0/\sigma(z_0))$ is calculated with the z_0 of the lepton with respect to the candidate and the sum taken over all tracks assigned to the candidate. A value of 1 is used in place of the z_0 significance if the z_0 significance is smaller than 1.
- Iterating through the list once, the currently selected primary vertex candidate is replaced if the weight of the new candidate is larger than 3 times the weight of the currently selected candidate.

The efficiencies of the primary vertex reconstruction and the default and lepton-based selection methods are listed in table 4.3 for several physics processes in luminosity scenarios I, II, and for the case of an average number of 23 interactions per bunch crossing at a bunch spacing of 25 ns. Here, the reconstruction efficiency is defined as the fraction of events in which at least one primary vertex candidate is reconstructed within 300 μm of the true primary vertex. For processes with one lepton in the final state, exactly one reconstructed lepton passing the lepton selection of the vector boson fusion analysis is required. For processes with more than one lepton in the final state, at least one reconstructed lepton passing the lepton selection of the vector boson fusion analysis is required. If at least one reconstructed muon passing the selection is present in the event the muon with the largest transverse momentum is used for the identification. Otherwise, the electron with the largest transverse momentum is used.

The selection efficiency is improved for all processes if the impact parameter information of the lepton is used. The selection is observed to be close to optimal for the $t\bar{t}$ and vector boson fusion processes in luminosity scenario I. For all processes and luminosity scenarios I and II, the fraction of events where a primary vertex candidate has been reconstructed within 300 μm of the true primary vertex but the selected primary vertex is not found within the same interval is well below 1% with the lepton-based selection. At the nominal luminosity, the same fraction is below 2%.

Future studies may include the optimization of the use of information in events with more than one lepton. It may also be possible to improve the primary vertex reconstruction efficiency using the knowledge of high-p_T objects in an event.

4.7 Jet-vertex association

In this section, the reduction of the central jet veto efficiency shown in figure 4.8 is addressed by studying the possibility to identify jets from the primary interaction. Jets reconstructed in the calorimeter are linked to the interaction region by tracks pointing to the area of the jet. The z coordinate of the perigee of the tracks is used to discriminate between tracks originating from the primary interaction and tracks from additional minimum bias interactions. Jets are assigned to the primary interaction or the remainder of the event based on the fraction of the transverse momentum of tracks pointing to the jet contributed by tracks originating from the primary interaction vertex. This technique has been used at the D0 experiment and an implementation is available in the ATLAS software [57]. Differences between the implementation developed for this study and the alternate implementation available in the ATLAS software are discussed where relevant and the performance is compared.

Tracks are selected according to the following criteria:

- Number of hits in the silicon detectors ≥ 6
- Number of pixel hits ≥ 2
- Transverse momentum ≥ 0.8 GeV

The selected tracks are extrapolated to the entrance of the electromagnetic middle calorimeter layer. A track is assigned to a jet if the distance expressed as $\Delta R = \sqrt{\Delta\phi^2 + \Delta\eta^2}$ between the direction of the impact point and the jet direction is less than the jet radius. Cone jets with a radius of $\Delta R = 0.4$ using topological clusters and H1-style calibration are used. As a cross-check, some distributions are shown for AntiKt jets with a radius parameter of 0.4 using topological clusters and local hadron calibration.

A track is assigned to the selected primary interaction vertex of the event if its z_0 significance with respect to the vertex is smaller than 30 and the track is not found close to a pileup vertex. A track is defined as being found close to a pileup vertex if a primary vertex candidate identified as a pileup vertex is reconstructed within a certain maximal distance in the z direction from the perigee with respect to the selected primary vertex. The maximal distance is chosen as the distance in the z direction between the pileup vertex pu and the selected primary interaction vertex pv multiplied by $\sum p_T(pu)/(\sum p_T(pu) + \sum p_T(pv))$. Figure 4.11 shows the significance of z_0 with respect to the selected primary vertex for tracks from the main interaction and from pileup. Distributions are shown both for all tracks and for tracks assigned to the primary vertex. For luminosity scenario I, tracks assigned to the primary vertex are observed to be more likely to originate from the main pp interaction than from additional minimum bias interactions over the whole accepted interval of the z_0 significance. The performance of the track-vertex association is similar in luminosity scenario II. An increased rate of tracks from minimum bias interactions is observed in the second scenario.

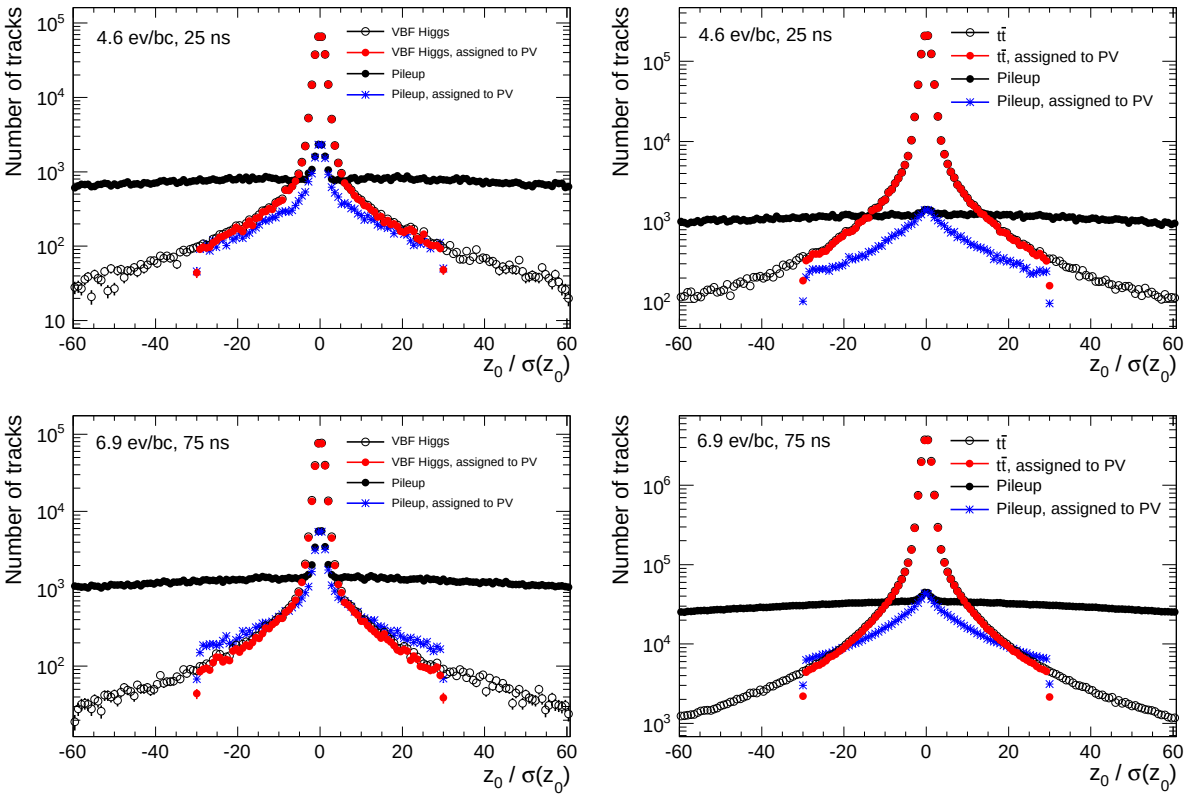

Figure 4.11: Significance of z_0 with respect to the selected primary interaction vertex of tracks from the main pp interaction and from pileup. An event preselection requiring a reconstructed lepton as in section 4.2 and track quality cuts are applied. Distributions are shown for all tracks (*black*) and for tracks assigned to the primary interaction vertex (*colored*) both for $H \rightarrow \tau^+\tau^- \rightarrow lh$ events (*left*) and for $t\bar{t}$ events (*right*) in the luminosity scenarios I (*top*) and II. The distribution for pileup tracks in $H \rightarrow \tau^+\tau^- \rightarrow lh$ events shows a peak around 0 which is due to a small fraction of misidentified primary vertex candidates.

For each jet, the fraction $\sum p_T(jet\ and\ pv)/\sum p_T(jet)$ is calculated where $\sum p_T(jet)$ denotes the total transverse momentum of all tracks associated with the jet and $\sum p_T(jet\ and\ pv)$ denotes the total transverse momentum of all such tracks which originate from the primary interaction vertex. Jets with a total associated track p_T of less than 2 GeV are assigned a negative value as in [57]. Figure 4.12 shows the fraction of the transverse momentum associated with a jet which originates from the primary vertex for $H \to \tau^+\tau^- \to lh$ and $t\bar{t}$ events and three different luminosity scenarios. As expected, for the zero-luminosity case the transverse momentum fraction is concentrated near 1. For the other luminosity scenarios significant contributions are observed also from jets with a small transverse momentum fraction from the primary vertex.

The discrimination power of the primary vertex p_T fraction is estimated by studying separately its distributions for jets that are part of the main pp event and for additional jets caused by pileup. To distinguish between jets from pileup and jets resulting from the primary interaction, the events are simulated with and without pileup. Jets in the pileup dataset for which a jet is found within the jet radius in the same event in the no-pileup dataset are labeled jets from the main pp interaction. The remaining jets present in the pileup dataset are labeled pileup jets. The distributions of the primary vertex p_T fraction for jets from the main pp interaction and for pileup jets are shown in figure 4.13. The distribution for pileup jets has a maximum towards 0 and decreases with increasing primary vertex p_T fraction. The distribution for jets from the main pp interaction shows the opposite behavior.

Figure 4.14 shows the rejection of pileup jets as a function of the efficiency for jets from the main pp interaction with the rejection defined here as the inverse of the efficiency. For comparison, figure 4.14 shows rejections which are obtained with the implementation of the method available in the ATLAS software. Release 15.0.0 is used for luminosity scenario I. Release 15.6.0 is used for luminosity scenario II. In release 15.0.0 a fix is applied to correct the calculation of the impact parameter. The impact parameter is calculated correctly in release 15.6.0 and the track selection cuts are loosened with respect to release 15.0.0. The performance of the implementation in release 15.6.0 is closer to the implementation developed for this study, however a small difference remains. The implementations differ by the methods used for the primary vertex selection and the assignment of tracks to the primary vertex. The implementation in release 15.6.0 uses the standard method implemented in the primary vertex reconstruction algorithm for the selection of the primary vertex. The assignment of tracks to the primary vertex in release 15.6.0 is inherited from the primary vertex reconstruction algorithm. The tracks used for the vertex fit are considered to originate from the primary vertex.

At an efficiency for signal jets of 80% a rejection of 9.6 is observed for pileup jets in $H \to \tau^+\tau^- \to lh$ events at a center-of-mass energy of 14 TeV in luminosity scenario I. For $t\bar{t}$ events at a center-of-mass energy of 10 TeV the observed rejection is 7.3 for the same luminosity scenario. In luminosity scenario II, the rejection is 7.5 in $H \to \tau^+\tau^- \to lh$ and 7.0 in $Z + 2j$, $Z \to \tau^+\tau^-$ events. Figure 4.15 shows the rejection of pileup jets as a function of the efficiency for jets from the main pp interaction for cone jets with H1-style calibration and for AntiKt jets with local hadronic calibration for luminosity scenario II. The rejection for AntiKt jets is observed to be slightly larger than the rejection for cone jets.

4.8 Central Jet Veto Performance

The efficiency of the central jet veto is evaluated after a preselection requiring a lepton trigger, a single reconstructed lepton and the identification and separation in η of the tagging jets as in section 4.2. No τ identification is applied to increase the number of events passing the preselection, however jets that are reconstructed within $\Delta R < 0.4$ of the true decay products of a hadronic τ decay are excluded from the analysis. Only jets in the region $|\eta| < 2.5$ covered by the Inner Detector are considered.

Figure 4.16 shows the number of jets in the region $|\eta| < 2.5$, with a transverse momentum above 20 GeV, not selected as tagging jets, and after the preselection. With pileup corresponding to luminosity

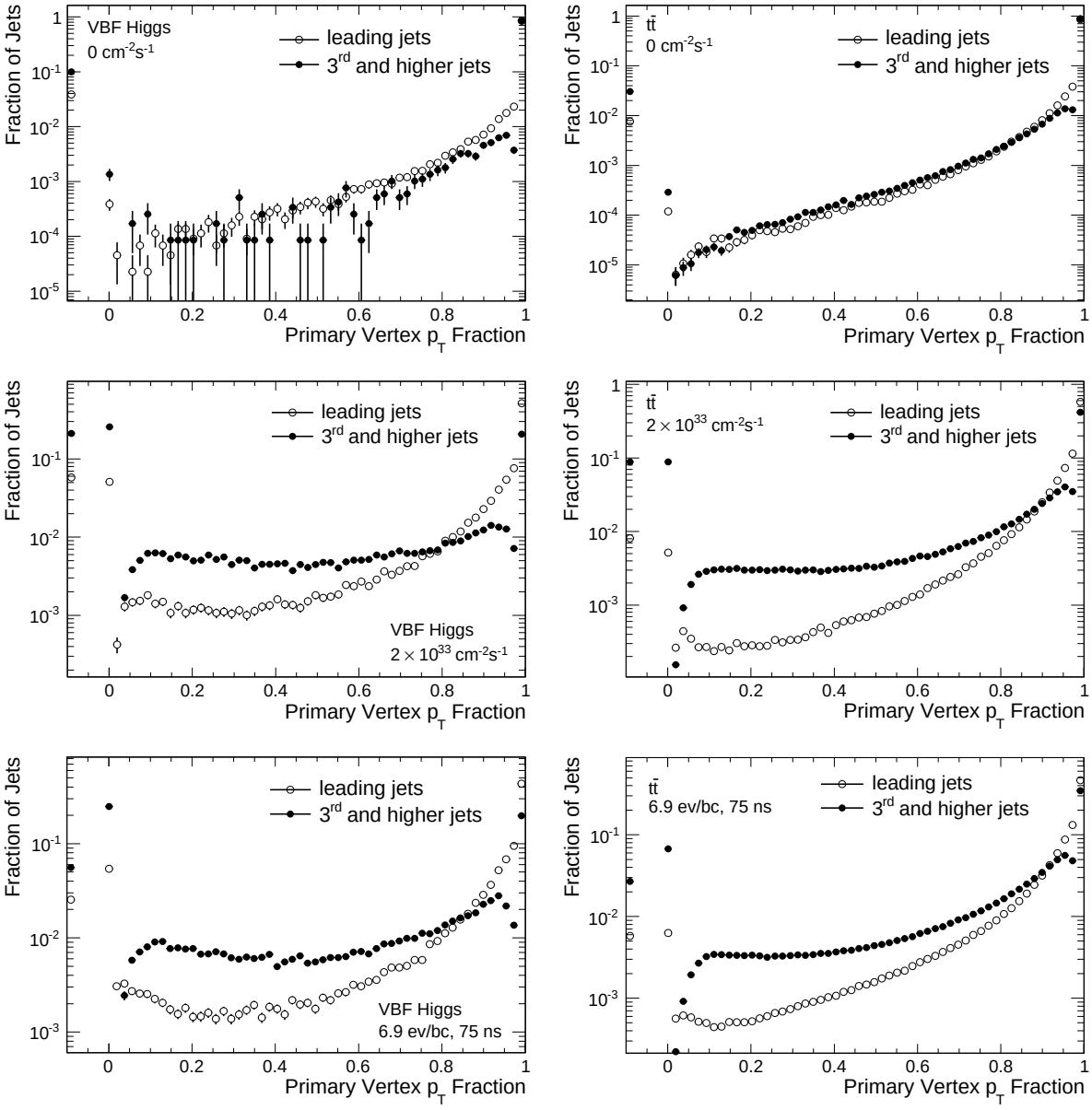

Figure 4.12: Fraction of the transverse momentum associated with a jet contributed by tracks from the primary vertex for $H \rightarrow \tau^+\tau^- \rightarrow lh$ events (*left*) and $t\bar{t}$ events (*right*) without pileup (*top*), in luminosity scenario I (*middle*) and in luminosity scenario II (*bottom*).

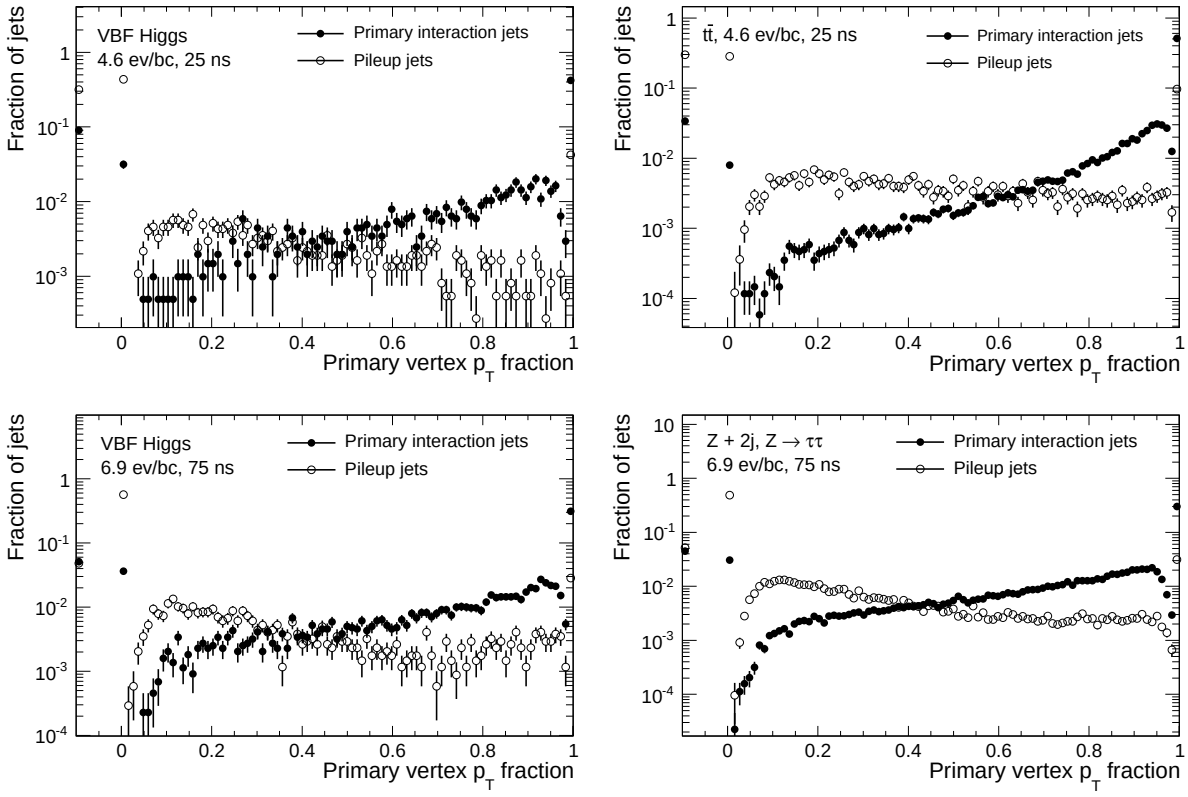

Figure 4.13: Fraction of the transverse momentum associated with a jet contributed by tracks from the primary vertex for jets not selected as tagging jets in $H \rightarrow \tau^+\tau^- \rightarrow lh$ events (*left*) and background events (*right*). The transverse momentum fraction is shown separately for jets from the primary interaction (*black*) and for jets caused by pileup (*white*). A preselection requiring a lepton trigger and a reconstructed lepton as in section 4.2 is applied. The VBF and $Z + 2j$ datasets were simulated for a center-of-mass energy of 14 TeV. The $t\bar{t}$ dataset was simulated for a center-of-mass energy of 10 TeV.

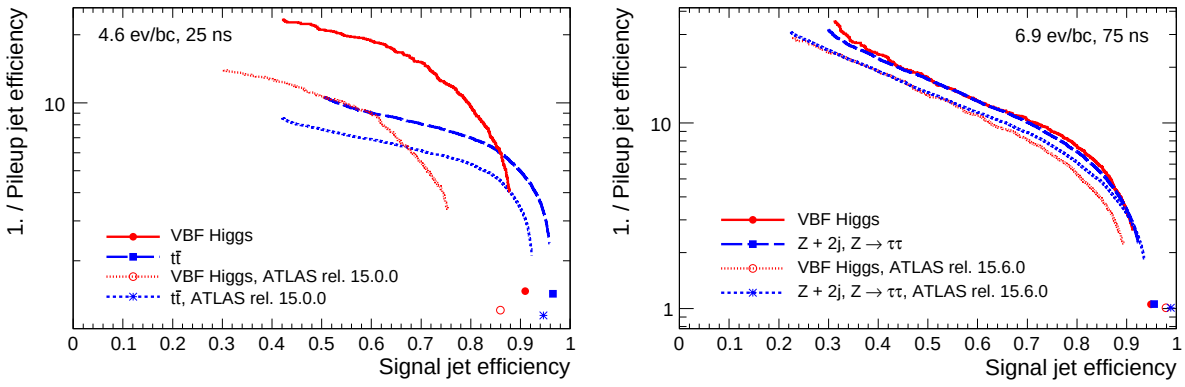

Figure 4.14: Rejection of jets caused by additional minimum bias interactions after a cut on the primary vertex p_T fraction as a function of the efficiency for jets from the main pp interaction. Only jets that do not have the largest or second-largest transverse momentum in an event are used. A preselection requiring a lepton trigger and a reconstructed lepton as in section 4.2 is applied. The rejections obtained with the implementation available in ATLAS software release 15.0.0 (*left*) and 15.6.0 (*right*) are shown for comparison.

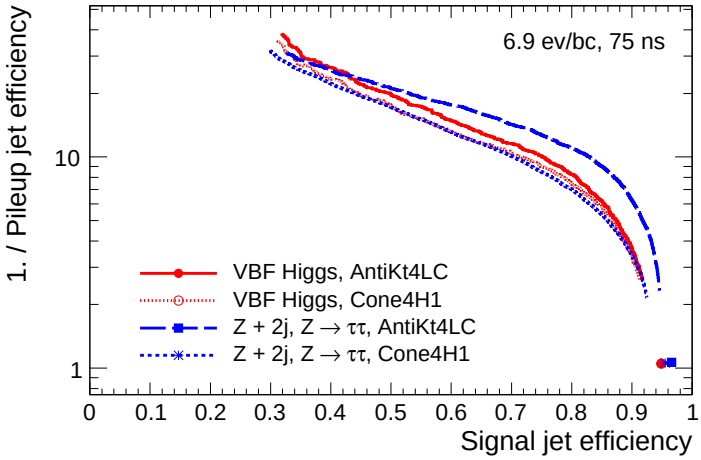

Figure 4.15: Rejection of jets caused by additional minimum bias interactions after a cut on the primary vertex p_T fraction as a function of the efficiency for jets from the main pp interaction. Distributions are shown for jets reconstructed with the cone algorithm with a radius of 0.4 and H1-style calibration and for jets reconstructed with the AntiKt algorithm with a radius parameter of 0.4 and local hadronic calibration. Jets are used only if they do not have the largest or second-largest transverse momentum in an event. A preselection is applied which requires a lepton trigger and a reconstructed lepton as in section 4.2.

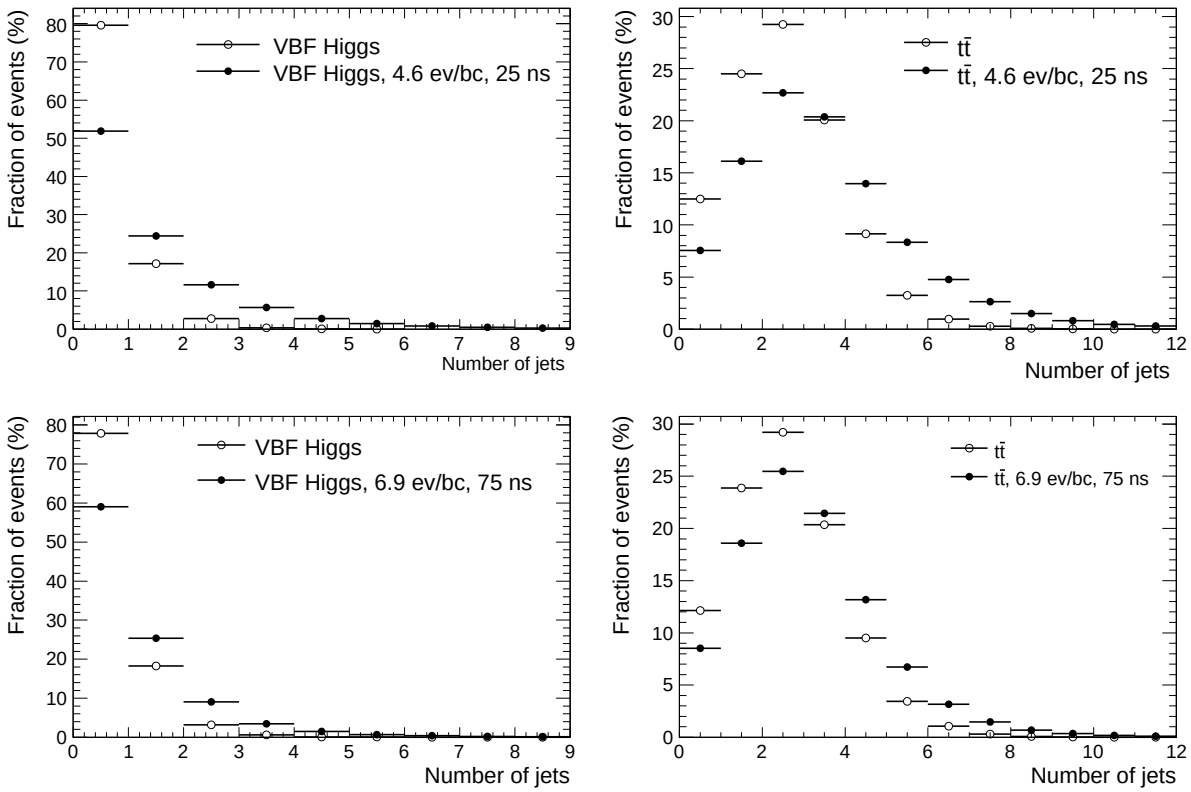

Figure 4.16: Number of jets not identified as tagging jets in the region $|\eta| < 2.5$ with a transverse momentum above 20 GeV in $H \to \tau^+\tau^- \to lh$ events (*left*) and $t\bar{t}$ events (*right*). The event samples are simulated with (*white*) and without (*black*) pileup for the luminosity scenarios I (*top*) and II (*bottom*). Jets found within a cone of $\Delta R < 0.4$ of the true hadronic decay products of a τ lepton decay have been excluded.

scenario I, the average number of jets increases by 0.76 in $H \to \tau^+\tau^- \to lh$ events and by 0.97 in $t\bar{t}$ events. In luminosity scenario II, the average number of jets increases by 0.43 in $H \to \tau^+\tau^- \to lh$ and by 0.55 in $t\bar{t}$ events. As mentioned in section 4.1, the rate of additional QCD dijet events in the datasets for luminosity scenario II is expected to be underestimated due to the use of minimum bias events generated for a center-of-mass energy of 10 TeV. From the cross sections given in section 4.3 one can expect a rate of approximately two thirds of the rate in datasets generated for a center-of-mass energy of 14 TeV. A likely explanation for the increase of the jet multiplicity being greater in $t\bar{t}$ events is the larger jet multiplicity in $t\bar{t}$ events and a positive bias of the jet energy due to pileup as discussed in section 4.5. The fraction of events without a jet decreases by 34.9% in $H \to \tau^+\tau^- \to lh$ events and by 39.5% in $t\bar{t}$ events by the addition of pileup corresponding to luminosity scenario I. In luminosity scenario II, the decrease is 24.2% in $H \to \tau^+\tau^- \to lh$ events and 29.9% in $t\bar{t}$ events.

The efficiency of the central jet veto applied in the region $|\eta| < 2.5$ using a transverse momentum threshold of 20 GeV is shown in figure 4.17. In the presence of pileup, the efficiency for signal events without a cut on the primary vertex p_T fraction is significantly reduced with respect to the no-pileup scenario. The efficiency is observed to be $(56.0 \pm 0.9)\%$ with pileup and $(88.4 \pm 0.5)\%$ without pileup. A large fraction of the efficiency lost in the pileup case is regained by considering only jets with a primary vertex p_T fraction above a certain cut value. Depending on the cut value, efficiencies between 74% and 87% are observed. A similar general behavior is observed for the $t\bar{t}$ process.

The performance of the central jet veto is evaluated using $H \to \tau^+\tau^- \to lh$ and $t\bar{t}$ events only since the production of complete background datasets for both considered luminosity scenarios was not feasible. Figure 4.17 shows the expected changes of the signal-to-background ratio and the Gaussian signal significance obtained by applying the central jet veto in the presence of pileup relative to the changes expected in the no-pileup scenario. The signal significance has a maximum at 0.5 in luminosity scenario I. The signal-to-background ratio has a secondary maximum at the same value. The global maximum of the signal-to-background ratio is observed for the case in which no jets are discarded. The efficiency for signal jets as defined in section 4.7 at a cut value of 0.5 is 80% in $H \to \tau^+\tau^- \to lh$ events and 92% in $t\bar{t}$ events. The signal significance after the application of the primary vertex p_T fraction cut is expected to be reduced by 5.9% with respect to the no-pileup case. The signal significance is expected to be 12% larger than for the case in which no cut is applied.

In luminosity scenario II, the signal-to-background ratio is observed to decrease continuously with an increasing cut value to below 50% at a cut value of 0.9. The signal significance has a maximum at a cut value of 0.1. After the application of the primary vertex p_T fraction cut, the signal significance is expected to be reduced by 10.0% with respect to the no-pileup case. The signal significance is expected to be 2.8% larger than in the case in which no cut is applied. The differences with respect to luminosity scenario I are explained by the lower pileup jet multiplicity as shown in figure 4.16 and the larger pileup track multiplicity as seen in figure 4.11 in luminosity scenario II. For an increase of the signal significance achieved by the central jet veto, a large rejection of pileup jets in $H \to \tau^+\tau^- \to lh$ events has to be balanced against a large efficiency for jets originating from $t\bar{t}$ events. In $t\bar{t}$ events for luminosity scenario II, a significant fraction of jets from the main interaction that would trigger the jet veto without pileup are rejected due to contributions to the primary vertex p_T fraction from pileup tracks. The dependence on the pileup track multiplicity can be reduced by only requiring a certain minimum p_T fraction if the total p_T of all tracks which are associated to the primary vertex is below 4 GeV. This is illustrated in figure 4.17. The dependence of the efficiency on the cut value for $H \to \tau^+\tau^- \to lh$ and $t\bar{t}$ at large cut values is reduced by this modification as expected. The increase of the signal significance is unchanged.

Future studies may include a comparison with purely track-based methods for a central jet veto and a comparison with a cut on the transverse momentum from the primary vertex instead of a cut on the transverse momentum fraction. The cut value on the primary vertex p_T fraction may be optimized using simulated signal events overlaid with minimum bias data from the detector for a given luminosity.

4.9 Summary

The use of jet-vertex association for the rejection of pileup jets and its application to the central jet veto in the vector boson fusion process are studied. Two luminosity scenarios of 4.6 interactions per bunch crossing at 25 ns bunch spacing and 6.9 interactions per bunch crossing at 75 ns bunch spacing are considered. Jets caused by pileup from minimum bias interactions are discarded by requiring a minimum fraction of the transverse momentum of tracks pointing to the position of the jet in the calorimeter to originate from the primary vertex.

The selection of the primary vertex can be improved by exploiting the impact parameter information of the reconstructed leptons. If a lepton is reconstructed, the correct primary vertex is selected in more than 99% of the events at intermediate luminosities and in more than 98% of the events at the design luminosity.

In datasets for luminosity scenario I at a center-of-mass energy of 14 TeV, the jet-vertex association method implemented for this study is shown to reject approximately 90% of the jets caused by pileup that may trigger the central jet veto in vector boson fusion events while keeping 80% of the jets from the primary pp interaction. In $t\bar{t}$ events at a center-of-mass energy of 10 TeV approximately 86% of jets caused by pileup are rejected at the same efficiency for jets from the main interaction. In datasets for

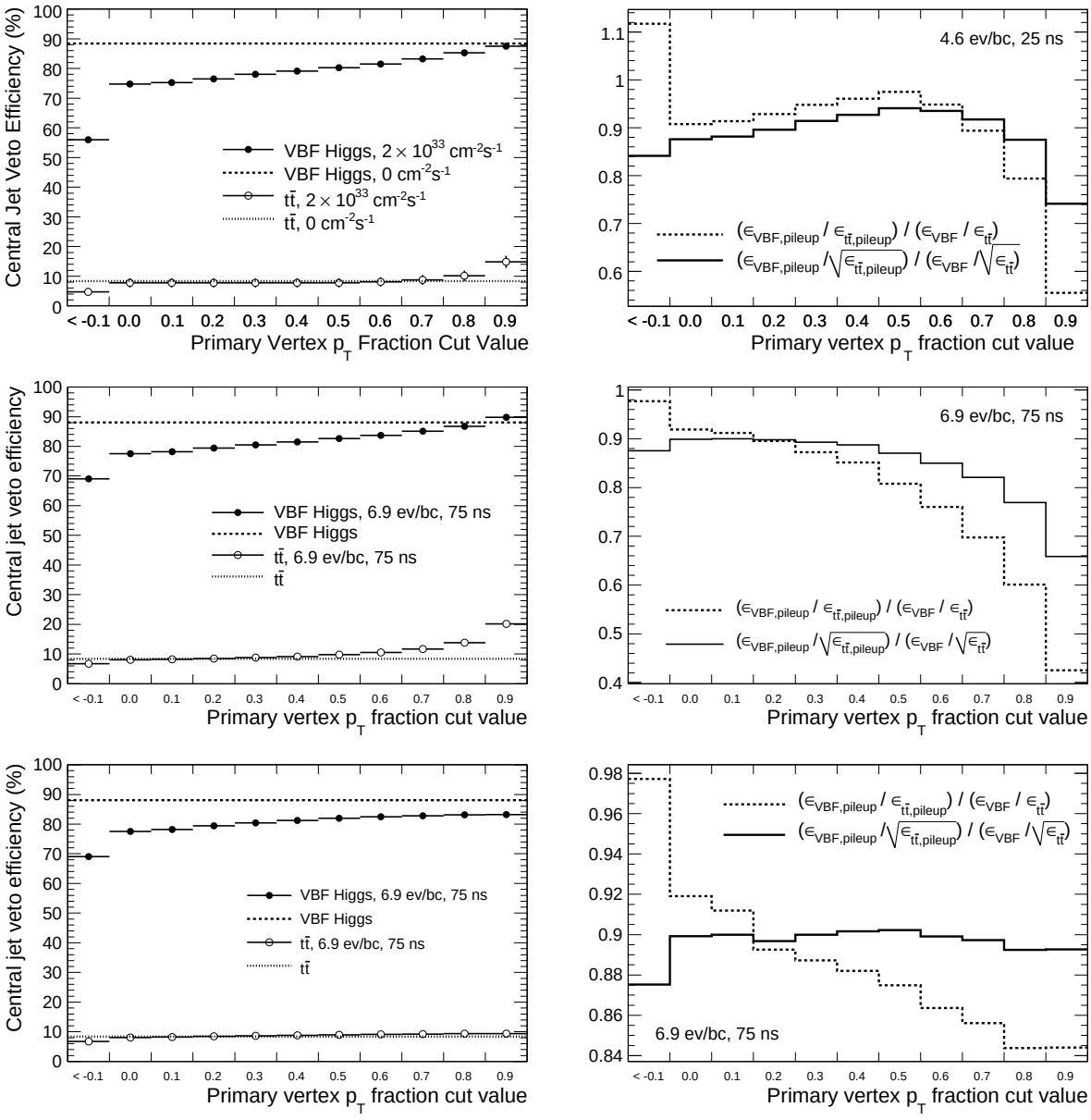

Figure 4.17: Efficiency of the central jet veto applied in the range $|\eta| < 2.5$ using a preselection as described in the text and a transverse momentum threshold of 20 GeV after a cut on the primary vertex p_T fraction as a function of the cut value (*left*) for $H \to \tau^+\tau^- \to lh$ (*black*) and $t\bar{t}$ (*white*) events. The efficiencies without pileup and without a cut on the primary vertex p_T fraction are shown for comparison. The plots on the *right* show the expected changes of the signal-to-background ratio (*dashed*) and the Gaussian signal significance (*solid*) obtained by applying the central jet veto in the pileup scenario relative to the changes expected for the no-pileup case. Distributions are shown for luminosity scenarios I (*top*) and II (*middle* and *bottom*). The bottom pair of plots shows distributions for which all jets with a transverse momentum from tracks from the primary vertex above 4 GeV are assigned a primary vertex transverse momentum fraction of 1.

luminosity scenario II, 87% and 86% of pileup jets are rejected in signal and $t\bar{t}$ events, respectively, at an efficiency of 80% for jets from the main interaction.

The efficiency of the central jet veto after an event preselection is observed to be reduced from $(88.4 \pm 0.5)\%$ to $(56.0 \pm 0.9)\%$ for $H \to \tau^+\tau^- \to lh$ events in luminosity scenario I. A cut on the fraction of the transverse momentum from the primary interaction vertex recovers a large fraction of the efficiency lost due to pileup. After a cut on the primary vertex p_T fraction of 0.5 the efficiency of the central jet veto for the signal process is expected to be $(80.3 \pm 0.6)\%$. The Gaussian signal significance after the application of the central jet veto is expected to increase by 12% by the requirement of an association of the jets to the main pp interaction vertex. In a dataset for luminosity scenario II, a maximum of the expected signal significance at a small cut value of 0.1 is observed. At large cut values, many jets in $t\bar{t}$ events are rejected due to a large contribution from pileup. As a consequence, these events are not rejected by the central jet veto. The latter can be improved by also accepting jets if the sum of the transverse momenta exceeds a certain threshold, where the sum is taken over all tracks which point to the jet and originate from the primary vertex.

Chapter 5

Formation of topological clusters in the presence of pileup

Jets are reconstructed using clusters of calorimeter cells [45] as input objects. The clusters are formed either by assigning all cells within a square in a fixed grid in the η-ϕ plane to a calorimeter tower object or by forming topological clusters that represent extended signal energy deposits of a variable size and shape.

Cells are selected during the formation of topological clusters by applying cuts on the energy reconstructed in the cells. The reconstructed energy in a cell may be negative due to the finite resolution of the energy reconstruction. To cancel the noise contribution, clusters are formed from cells with positive and negative signals. In the presence of pileup the cancellation is incomplete and the topological cluster formation introduces a significant positive bias to the reconstructed jet energy. A method is suggested which significantly reduces the bias.

The formation of topological clusters is described in section 5.1. In section 5.4 the Monte-Carlo datasets used for this study are listed. The effects of two-sided symmetric signal significance cuts on the average cell and cluster energies in minimum bias data are discussed in section 5.5. An improved method for the cell selection is suggested in section 5.6. The method is applied to QCD dijet and $t\bar{t}$ events and results are given in section 5.7.

5.1 Formation of topological clusters

Topological clusters are seeded by cells that pass a relatively large seed cut on the signal significance. The signal significance is defined in this context as the energy reconstructed in a cell divided by the RMS of the noise in the cell. The cut can be applied either to the signal significance or to its absolute value, accepting also cells with a large negative energy deposit. Cells located next to a cell contained in the cluster are added to the cluster if their signal significance passes a moderate neighbor cut. This second step is iterated until no further neighboring cells passing the neighbor cut are present. The clusters are finalized by adding all cells which are located next to a cell contained in the cluster and which pass a third small cut on the signal significance. With this procedure, the number of clusters is determined mostly by the seed cut while the size of the clusters is more sensitive to the intermediate neighbor cut. The largest rejection of noise is achieved by the seed cut while the cluster growing procedure ensures that energy deposits in the tails of the showers are included in the object. The cluster creation is followed by a cluster splitting step around local maxima that is described in detail in [45].

In this study, cut values of 4, 2 and 0 are used as the seed cut, the neighbor cut and the cluster finalization cut, respectively, which are the standard cut values for the topological clusters used as input to the jet reconstruction. In the standard clustering procedure, these cuts are applied to the absolute value

of the signal significance so that on average the negative noise contributions cancel the positive ones. In a pure noise dataset the average energy in clusters after the application of these two-sided symmetric cuts vanishes if the cell energy distributions are symmetric and uncorrelated.

5.2 Treatment of pileup in the liquid argon calorimeter

The signal in the liquid argon calorimeter is sampled in five consecutive bunch crossings starting with the triggered bunch crossing. Due to the length of the electron drift time in the liquid argon, the sampled signal is affected by energy deposits in up to 32 bunch crossings preceding the triggered bunch crossing. The signal shaping and readout of the calorimeter are optimized to minimize the impact of pileup on the measurement. A bipolar signal shape is used. It has a relatively short initial peak used to measure the amplitude and time. The peak is followed by a long negative tail. The amplitude and time of the signal are determined from the measured values using optimal filtering [58]. The integral of the pulse shape vanishes and the average cell energy in randomly triggered events is close to 0 and independent of the luminosity for the nominal bunch spacing of 25 ns. With an increasing bunch spacing, the discrete integral will start to differ from 0, depending on the exact pulse shape of a cell. For a bunch spacing of 75 ns this effect is demonstrated later in this chapter.

Figure 5.1 shows pulse shapes for the electromagnetic barrel and the forward calorimeter measured during a data taking period with cosmic muons in September 2008. Typical pulse shapes used in the digitization of the liquid argon calorimeter are shown in figures 5.2 and 5.3. The increase of the width of the liquid argon gap in the EM endcap with the radius leads to an increase of the drift time. This effect is visible in figure 5.2.

At a luminosity of 0, the reconstructed cell energies have a Gaussian distribution given by the electronic noise. The width of the cell energy distributions in randomly triggered events increases with the luminosity. The increase is due to an increase of the electronic noise contribution and due to energy deposits mainly from additional minimum bias interactions. The electronic noise contribution increases due to a different choice of the optimal filtering coefficients which are optimized to minimize the total noise. The increase due to energy deposits is taken into account in the topological cluster formation by adding a pileup noise term to the electronic noise at the given luminosity in the definition of the noise RMS that determines the cell selection cuts. In the following, the cell noise is understood to include pileup noise if not indicated otherwise. The RMS of the total cell noise is shown in figure 5.4 for the case of a luminosity of 0 and for the case of luminosity scenario I, as defined in section 4.1.

Figure 5.5 shows the expected total noise, expressed as the reconstructed transverse energy, in a 3x5 electromagnetic cluster in the barrel of the calorimeter for different luminosity scenarios. Both the width of the noise distribution and the positive tail are observed to increase with the luminosity. Since the average energy remains 0 due to the bipolar pulse shape, the most probable value becomes negative. Figure 5.6 shows the total noise in individual cells in the electromagnetic barrel middle layer at $\eta = 0$ and in the first FCal module at $\eta = 4$ for a luminosity scenario of 2.3 interactions per bunch crossing at a bunch spacing of 25 ns and for luminosity scenarios I and II. The distributions at 25 ns have similar characteristics to the ones shown in figure 5.5. At 75 ns bunch spacing, the negative part of the distribution is reduced in the forward calorimeter and the average reconstructed energy becomes positive. In the electromagnetic barrel middle layer the distributions for 2.3 interactions per bunch crossing at 25 ns bunch spacing and for luminosity scenario II do not differ significantly.

5.3 Treatment of pileup in the tile calorimeter

The signal in the tile calorimeter is sampled in seven consecutive bunch crossings. The shaped signal is unipolar with a full width at half maximum of 50 ns. The pulse shape is shown in figure 5.7. In the

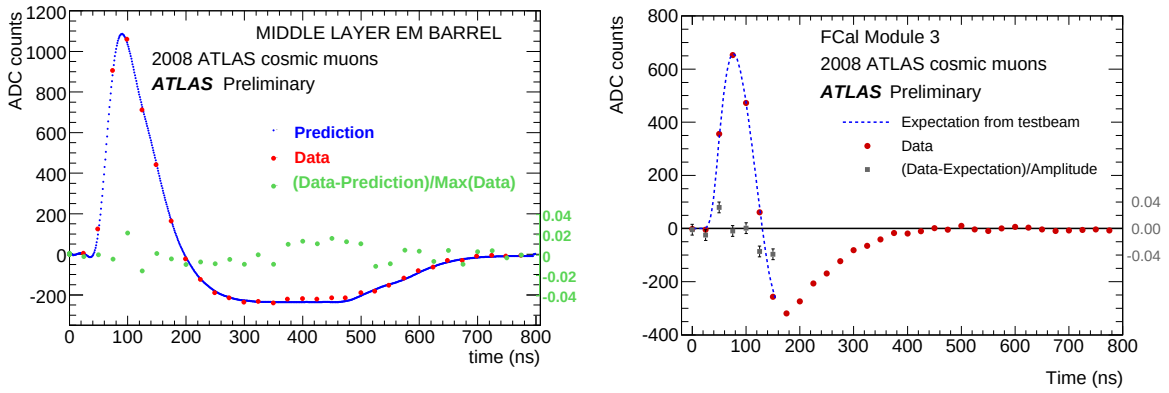

Figure 5.1: Pulse shapes observed during data taking with cosmic muons in the electromagnetic barrel middle layer (*left*) and in the third FCal module (*right*).

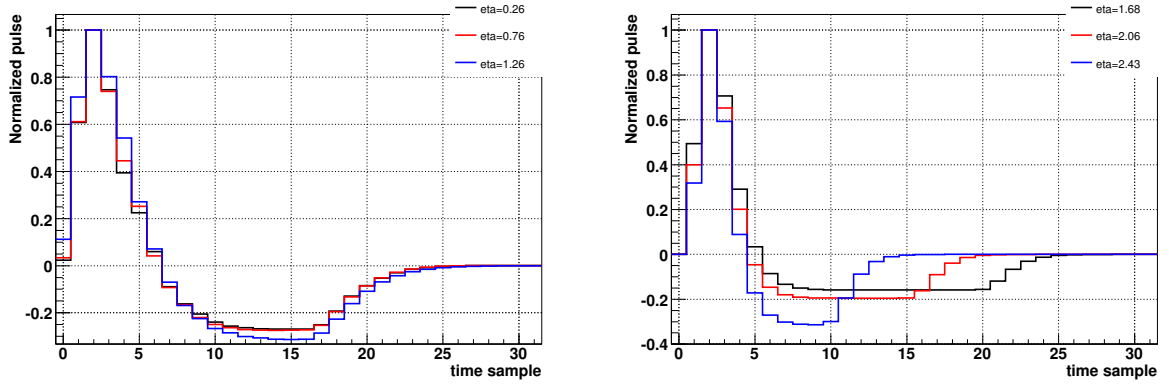

Figure 5.2: Pulse shapes used for the digitization of simulated data for different cells of the electromagnetic barrel middle layer (*left*) and the electromagnetic endcap middle layer (*right*). [59]

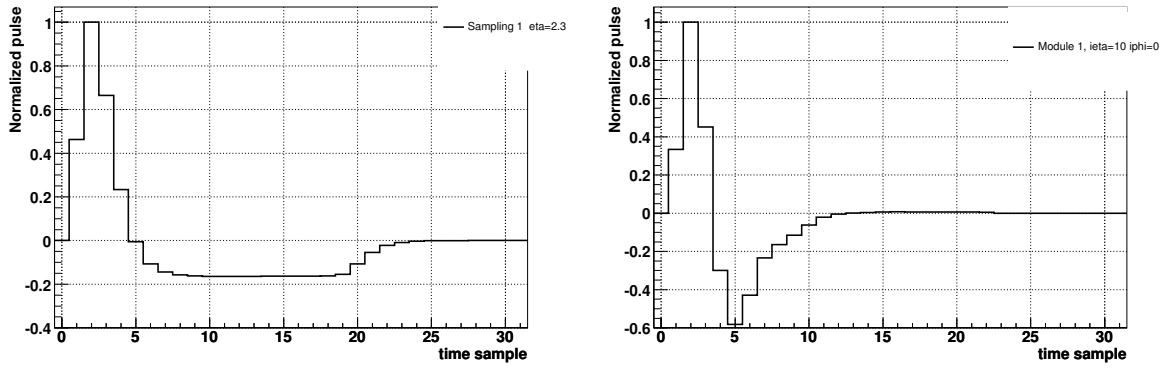

Figure 5.3: Typical pulse shapes used for the digitization of simulated data in the hadronic endcap (*left*) and the forward calorimeter (*right*). [59]

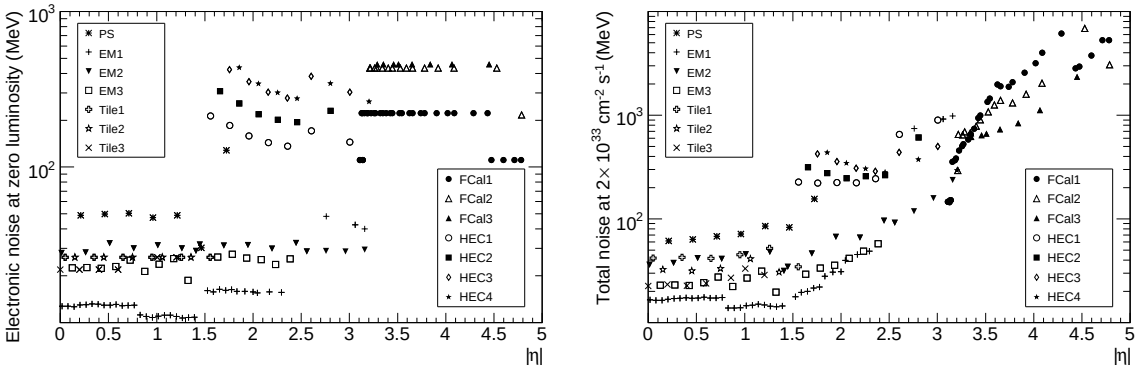

Figure 5.4: Expected RMS of the noise in individual calorimeter cells as a function of $|\eta|$ for a luminosity of 0 (*left*) and for luminosity scenario I (*right*). [13]

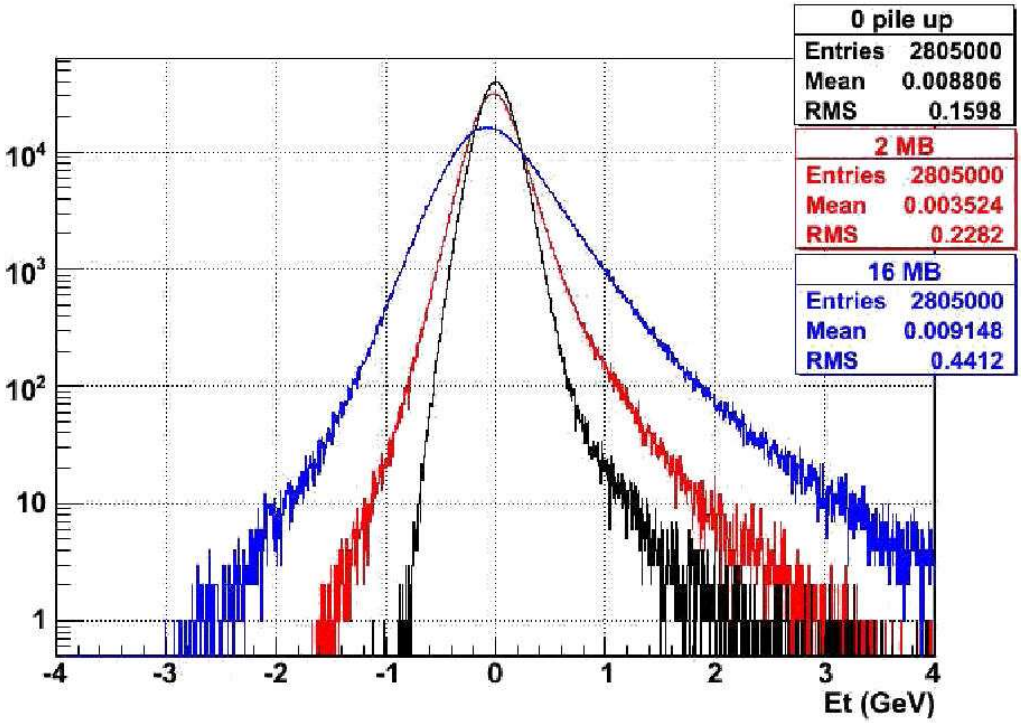

Figure 5.5: Total noise, expressed as the reconstructed transverse energy, in a 3x5 electromagnetic cluster in the barrel region of the calorimeter for different luminosity scenarios. [59]

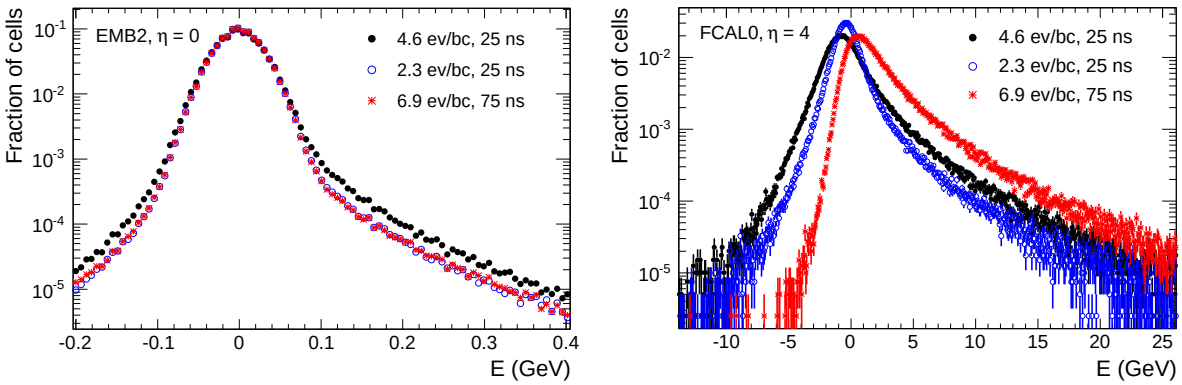

Figure 5.6: Total noise, expressed as the reconstructed energy, in a individual cells of the electromagnetic barrel middle layer (*left*) at $\eta = 0$ and the first FCal module (*right*) at $\eta = 4$ for different luminosity scenarios.

tile calorimeter there is no intrinsic cancellation of pileup due to the pulse shape as in the liquid argon calorimeter, but due to the significantly shorter pulse and the shielding by the liquid argon calorimeter the tile calorimeter is less affected by pileup.

5.4 Monte Carlo Datasets

For the study of the properties of cell noise distributions including pileup noise and for the determination of asymmetric cuts, datasets of simulated minimum bias events are used. Minimum bias datasets for three different luminosity scenarios were produced using ATLAS software release 14.2.25. The jet response is studied using centrally produced mc08 Monte Carlo for the QCD dijet and $t\bar{t}$ processes. All datasets used in this study are listed in table 5.1.

5.5 Average cell energies in minimum bias data with symmetric cuts

Due to the bipolar pulse shape [59] of the ATLAS LAr calorimeter, the average energy reconstructed for an event in a calorimeter cell remains 0 for any luminosity at a bunch spacing of 25 ns. Thus, large signals are reconstructed without a bias from noise. In calorimeter regions without signal energy deposits, two-sided symmetric cuts introduce a positive bias on the average cell and cluster energies due to the asymmetric shapes of the noise distributions in the presence of pileup [61, 62]. Figure 5.8 shows the average cell energy in the electromagnetic barrel middle layer and the first FCal module as a function of η in simulated single minimum bias events and in simulated minimum bias events for luminosity scenarios I and II. The average energy is close to 0 at the nominal bunch spacing of 25 ns. At a bunch spacing of 75 ns, the average energy is close to 0 in the electromagnetic barrel middle layer, however in the forward calorimeter the average cell energy is positive and several GeV above the average cell energy in single minimum bias events. Distributions for all layers of the liquid argon calorimeter are shown in appendix A. The average cell energy in luminosity scenario II is generally observed to be close to 0 in the central detector region and to increase with $|\eta|$.

Figure 5.9 shows the average cell energy after the application of two-sided symmetric 4σ[1] and

[1] Here and in the following, the letter σ is used to denote the RMS of the cell noise including pileup noise as returned by the CaloNoiseTool.

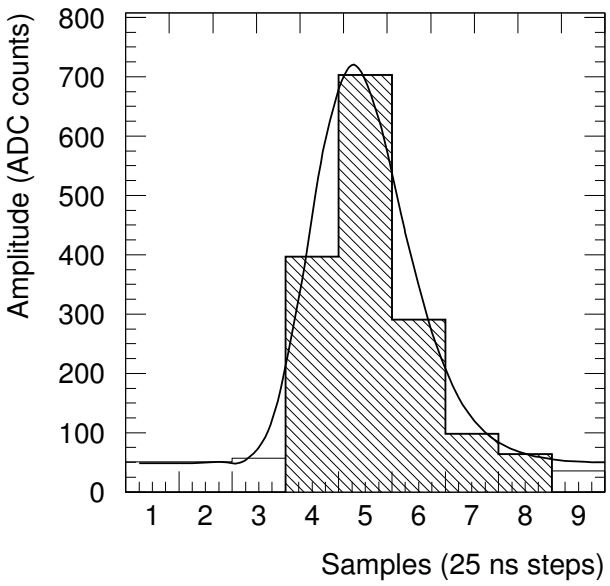

Figure 5.7: Pulse shape used for the digitization of simulated data in a cell of the tile calorimeter [60]. The histogram shows the sampled energies. The hatched area extends over the bins with the five largest entries. The line shows a fit of the pulse shape to the histogram.

Dataset	Process	$\sqrt{s}$ (TeV)	Luminosity scenario	Task ID	Events used
107499	Minimum Bias	10	4.6 events/bc, 25 ns	private	49 750
107499	Minimum Bias	10	2.3 events/bc, 25 ns	private	50 000
107499	Minimum Bias	10	6.9 events/bc, 75 ns	private	50 000
105012	QCD Dijet	10	4.6 events/bc, 25 ns	64886, 64887	376 472
105012	QCD Dijet	10	–	61101	355 784
105200	$t\bar{t}$	10	4.6 events/bc, 25 ns	41348	29 788
105200	$t\bar{t}$	10	6.9 events/bc, 75 ns	69466	119 419
105200	$t\bar{t}$	10	–	63975	42 467
105001	Minimum Bias	10	–	24528	500 000
005008	Cavern Background	–	–	28773	900 000

Table 5.1: Monte Carlo datasets used for the study of the topological cluster formation. The minimum bias datasets with non-zero luminosity were produced using the job transforms and job options available in release 14.2.25. The minimum bias and cavern background datasets 105001 and 005008 were used during the digitization step for the minimum bias samples with non-zero luminosity.

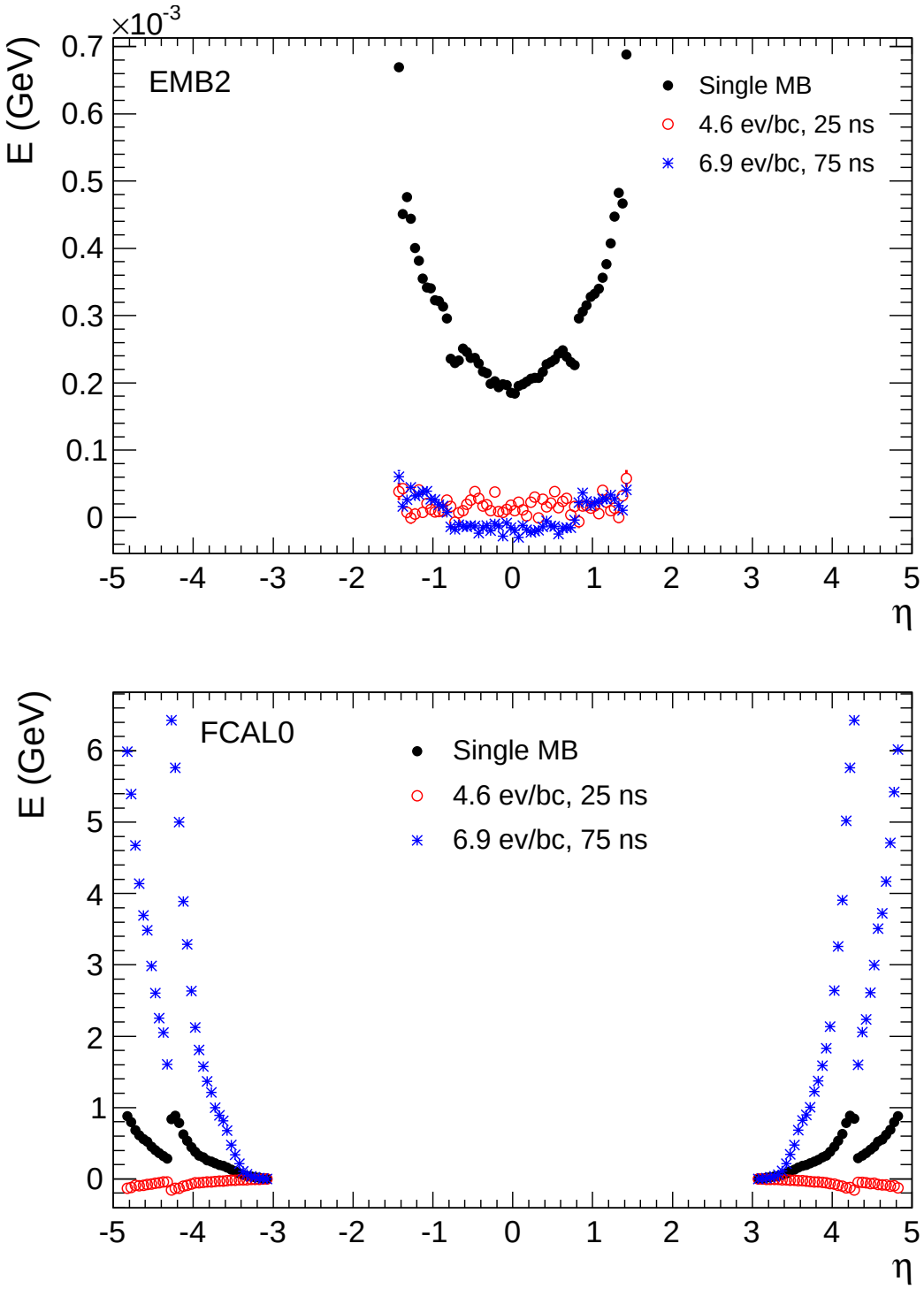

Figure 5.8: Average cell energy in simulated minimum bias events for luminosity scenarios I (*red*) and II (*blue*) in two exemplary layers of the LAr calorimeter. For comparison, the average energy in single minimum bias events (*black*) is shown.

2σ cuts as a function of η in the electromagnetic barrel middle layer and the first FCal module. For comparison, the average cell energy in minimum bias events without cuts and in single minimum bias events is shown. Distributions for all layers of the liquid argon calorimeter are shown in appendix B. Symmetric cuts are observed to introduce a positive bias due to the positive tails of the cell energy distributions. The bias is of the same order of magnitude as the average energy in single minimum bias events. In the central detector region, the ratio of the bias to the average energy in single minimum bias events is larger than in the endcaps and the forward calorimeter. In the liquid argon calorimeter, the bias introduced by the 2σ cut is larger than the one introduced by the 4σ cut.

5.6 Determination and application of asymmetric cuts

Asymmetric cuts that result in average cell energies of 0 are determined numerically from the cell energy distributions observed in simulated minimum bias data. The cut values are calculated separately for each calorimeter layer in 200 bins of the pseudorapidity η after the average cell energies in the same bins have been subtracted. The positive cut values are left unchanged at 4σ and 2σ and the negative cut values are adjusted separately for the 4σ and the 2σ cut in a way such that the average cell energies after the application of the cuts are 0. Figure 5.10 shows the average cell energies for 4 exemplary calorimeter layers after the application of the unmodified and the modified cuts.

The ratio of the positive cut values to the absolute value of the negative cut values is shown in figure 5.11. The ratio is shown for a luminosity scenario of 2.3 interactions per bunch crossing at 25 ns bunch spacing and for luminosity scenarios I and II. The ratio for the 4σ cuts is observed to be larger than the ratio for the 2σ cuts. Typical values for the ratio are between 1 and 3. The ratios generally increase with $|\eta|$ and reach values of up to 5 in the endcaps and the forward calorimeter. The η dependence changes with the luminosity. At a bunch spacing of 25 ns the difference for an increase of the luminosity from 2.3 to 4.6 events per bunch crossing is of the order 10%.

The average transverse energy of topological clusters at the EM scale constructed with symmetric cuts and with asymmetric cuts as a function of η is shown in figure 5.12. Both the average transverse energy per cluster and the average transverse energy in a circle in the η-ϕ plane with a radius of 0.4 are shown. With symmetric cuts, the largest average transverse energy per cluster is observed in the forward calorimeter. The largest average transverse energy in a fixed cone for a bunch spacing of 25 ns is observed in the central detector region. In luminosity scenario I, an average transverse energy in a cone with a radius of 0.4 in the central region of approximately 2 GeV is observed. The shape of the distribution of the average transverse energy in a fixed cone corresponds roughly to the expectations from the distribution of the transverse energy in single minimum bias events and the bias introduced by the symmetric cuts. For a bunch spacing of 75 ns, the average transverse energy in a fixed cone in the forward calorimeter is larger than for a bunch spacing of 25 ns due to the non-zero average of the cell energy in the forward region at that bunch spacing. Before the cluster formation, the average cell energies are determined and subtracted for each calorimeter layer and in the same bins of η as the asymmetric cuts. After the subtraction of the average cell energies and using asymmetric cuts for the cluster formation, the average transverse energy in clusters is observed to be close to 0.

The cluster multiplicity in a fixed cone with a radius of 0.4 is shown in figure 5.13 as a function of η. The multiplicity increases by a factor between 2 and 3 over a large fraction of the η distribution when using the asymmetric cuts.

Figure 5.14 shows the probability for individual cells to pass the asymmetric clustering cuts. The probabilities are observed to increase with $|\eta|$. In the forward region, the probability for cells to pass the negative 2σ cut reaches values significantly above 10% which leads to the reconstruction of large clusters.

The average cell energy in a given event is correlated with the number of minimum bias interac-

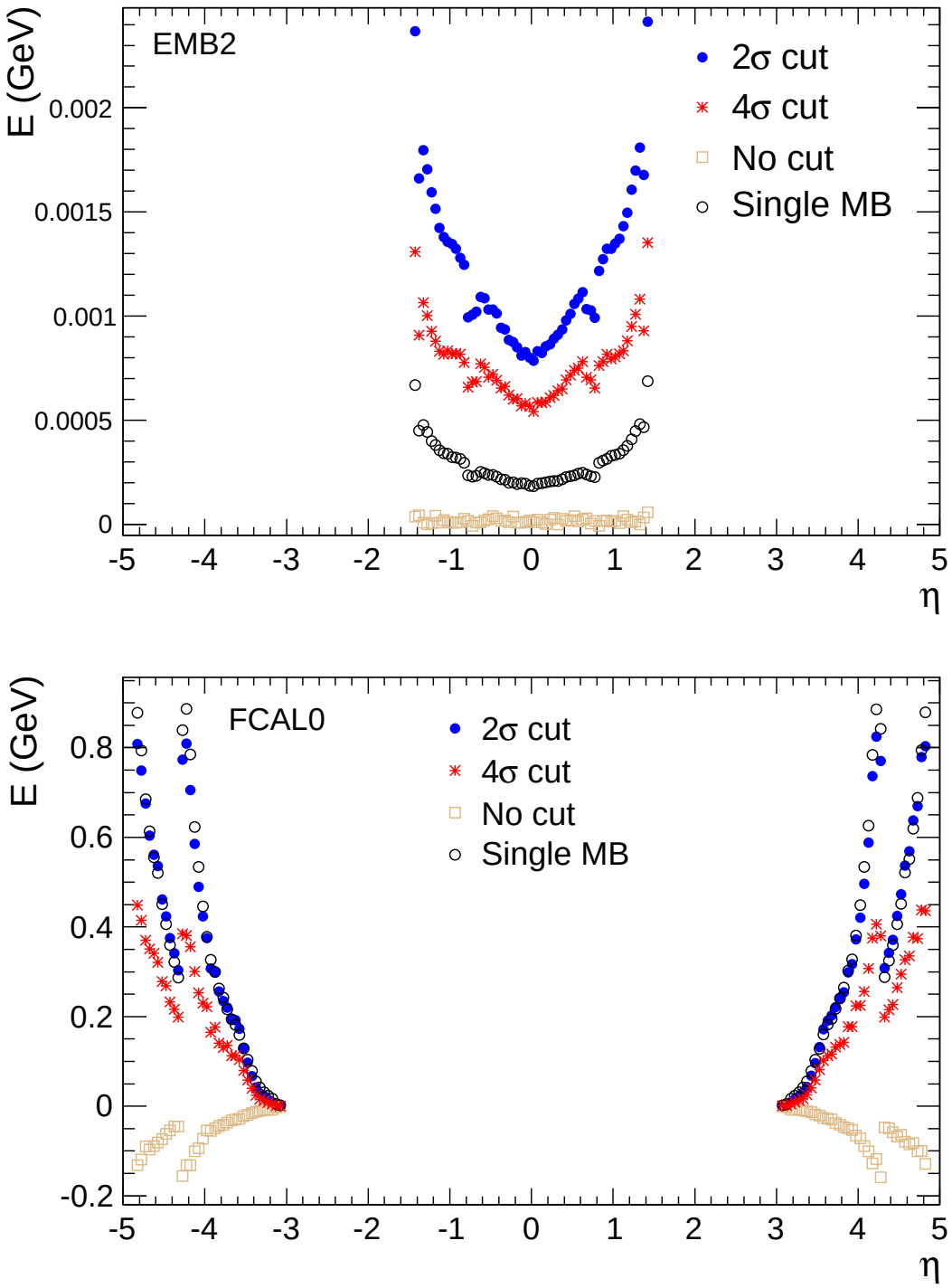

Figure 5.9: Average cell energy in simulated minimum bias data for luminosity scenario I after the application of two-sided symmetric cuts. For comparison, the average cell energy in minimum bias events without cuts and in single minimum bias events is shown.

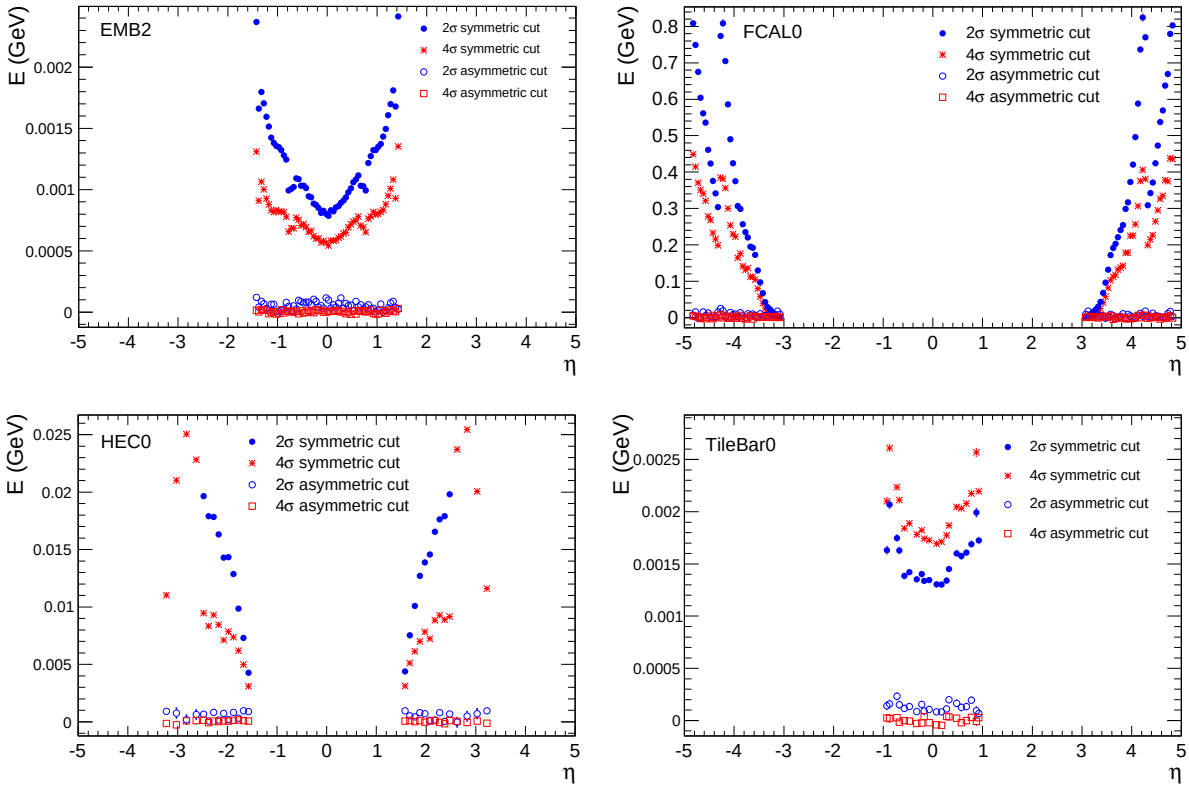

Figure 5.10: Average cell energy in simulated minimum bias events in luminosity scenario I after the application of cuts. Distributions are shown after the application of two-sided symmetric cuts (*solid markers*) and after the application of two-sided asymmetric cuts adjusted in a way such that the average energy vanishes (*open markers*). For the asymmetric cuts, the same positive cut value as for the symmetric cuts is used.

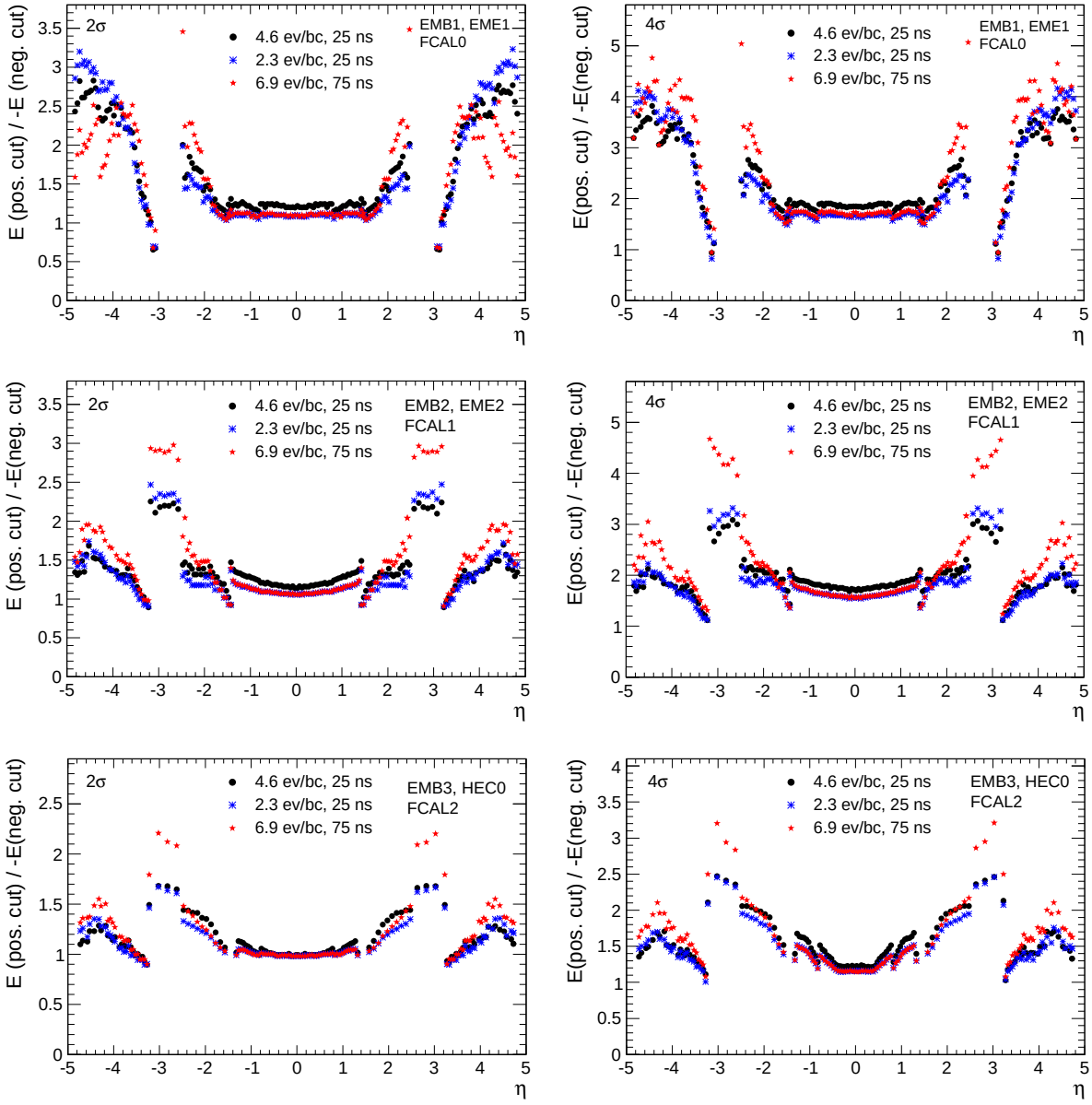

Figure 5.11: Ratio of the positive cut value to the absolute value of the negative cut for asymmetric $2\,\sigma$ (*left*) and $4\,\sigma$ (*right*) cuts in different LAr calorimeter layers. The ratio is shown for a luminosity scenarios of 2.3 events per bunch crossing at a bunch spacing of 25 ns and for luminosity scenarios I and II.

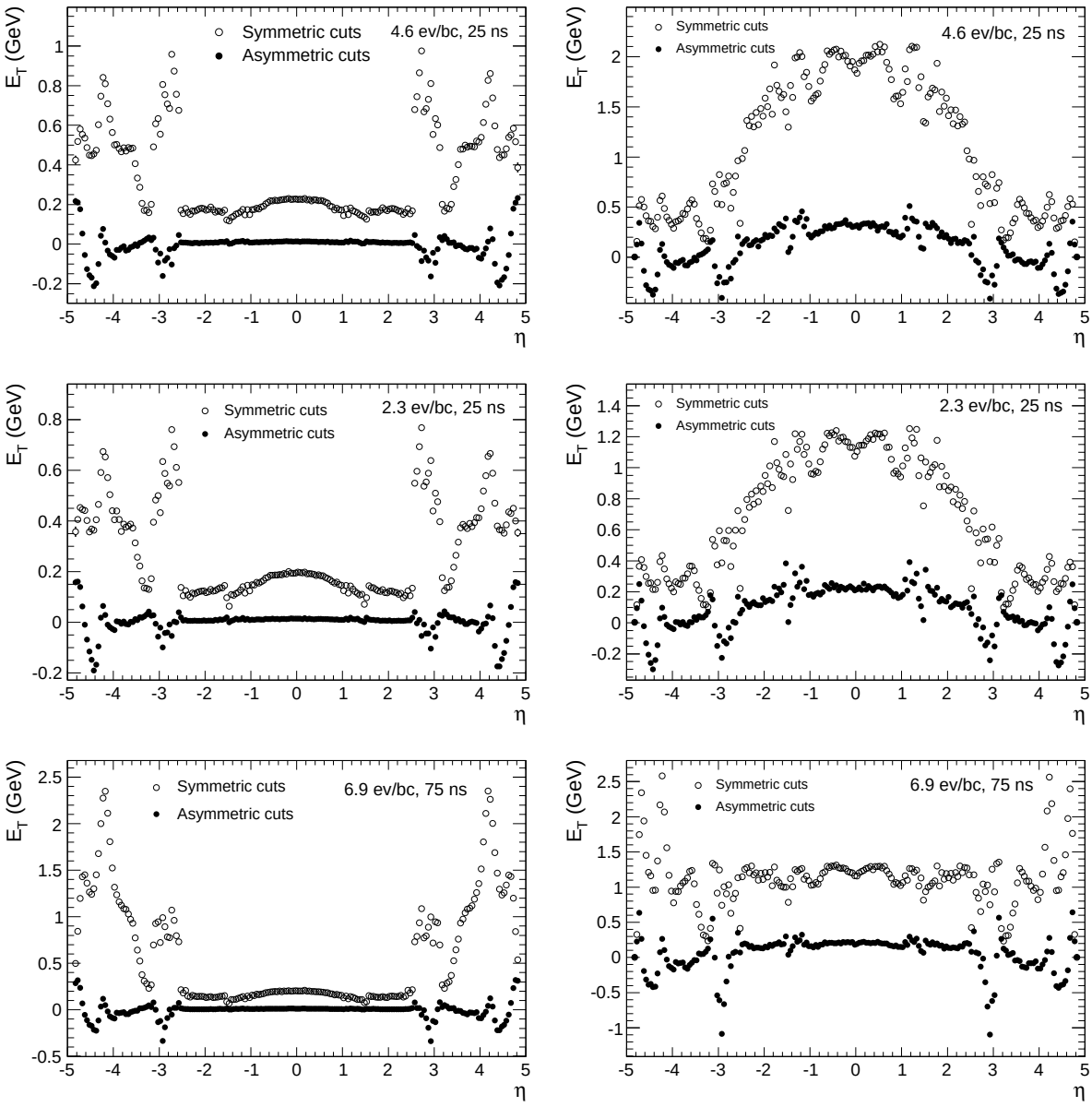

Figure 5.12: Average transverse energy at the EM scale of topoclusters constructed with symmetric (*white*) and asymmetric (*black*) cuts per cluster (*left*) and per circle in the η-ϕ plane with a radius of 0.4 (*right*).

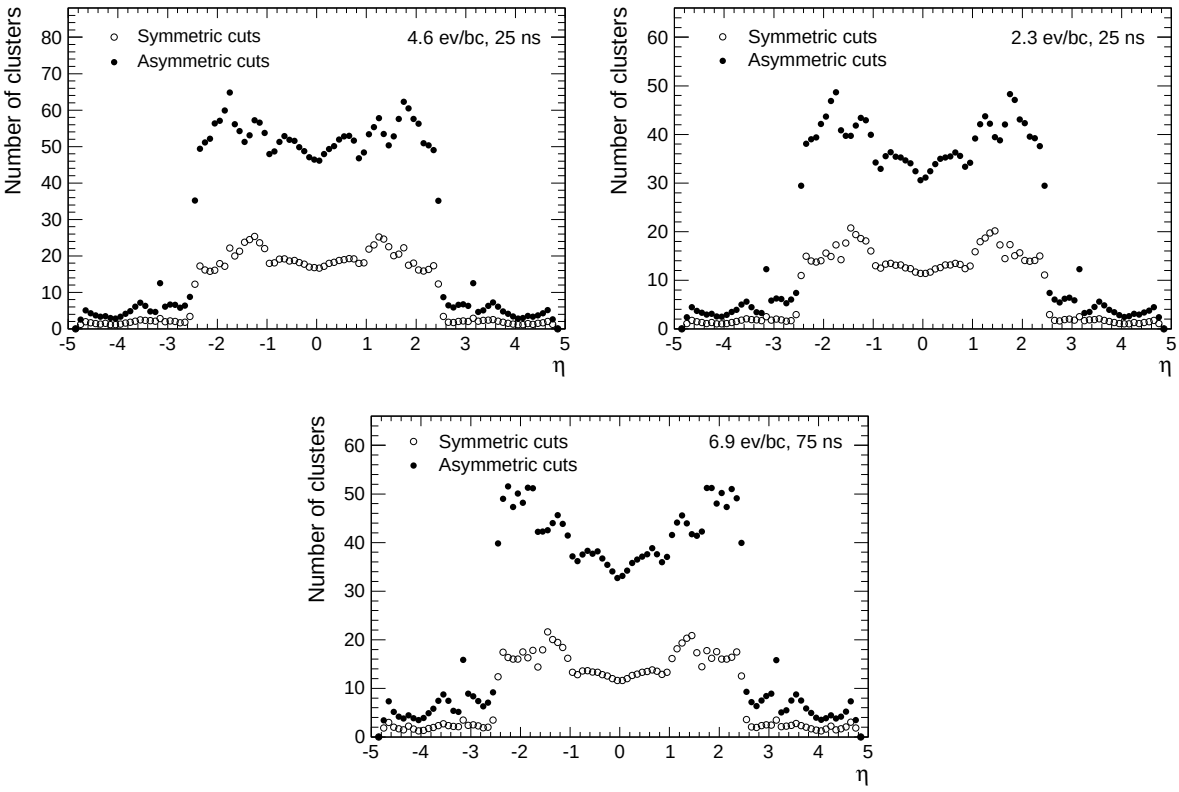

Figure 5.13: Cluster multiplicity per circle in the η-ϕ plane with a radius of 0.4 for a luminosity scenario with 2.3 events per bunch crossing at a bunch spacing of 25 ns and for luminosity scenarios I and II.

tions taking place in the triggered bunch crossing. Figure 5.15 shows typical cell energy distributions in simulated minimum bias events in luminosity scenario I in the central detector region and the forward calorimeter. To illustrate the dependence on the amount of energy from additional minimum bias interactions in the triggered bunch crossing, or in-time pileup, separate distributions are shown for events without primary vertices and with a number of primary vertices significantly above the average. In the central detector region mostly the positive tails are affected by in-time pileup while in the forward calorimeter due to the larger cell occupancy also a significant shift of the most probable value is observed.

The shift of the distributions in the forward calorimeter increases the probability for cells to pass the negative cuts if the number of interactions in the event is below average. The large probabilities to pass the negative 2σ cut in the forward region lead to large clusters that often cover a significant fraction of an FCal module. During the cluster splitting step, secondary maxima are identified and clusters are split between the maxima. A cell is required to have an energy of at least 500 MeV to be eligible as a local maximum. In the presence of pileup the total noise RMS in the forward region is significantly larger than 500 MeV, hence cells that pass the clustering cuts are generally eligible as local maxima and large noise clusters are split. However, the noise clusters created in this way may still contribute to the structure of the η distribution shown in figure 5.12.

5.7 Effect of asymmetric cell energy cuts on the jet response

The effect of asymmetric cuts applied during the cluster formation on the jet response is studied using jets reconstructed with the cone algorithm with a cone radius of 0.4 and H1 calibration. The H1 weights obtained in simulated data without pileup are used. They are expected to give a good approximation to the correct weights in the presence of pileup since the average cell energy density before the cluster formation is invariant under a variation of the luminosity as long as the average noise energy is fixed at 0. In the standard jet reconstruction, clusters are used as the input which are created using two-sided symmetric cuts with the thresholds at 4, 2 and 0. During the cluster formation, clusters with a negative seed cell energy and clusters with a negative energy are allowed. In the standard jet reconstruction, clusters with a negative energy are discarded. In order to achieve a reconstruction of the jet energy that is not biased by contributions from noise, including pileup noise, it is necessary to include the contributions from clusters with a negative energy. Hence, the jet reconstruction procedure is extended to include negative energy clusters in the determination of the jet energy. Clusters with a negative energy are not used for the determination of stable cones as described in section 4.2.3, however all clusters located inside stable cones are included in the calculation of the jet energy.

Figure 5.16 shows the jet response as a function of $|\eta|$ in two bins of the transverse energy in QCD dijet and $t\bar{t}$ events for luminosity scenarios I and II. The jet response is shown for standard jets reconstructed without considering clusters with a negative energy in events with and without pileup and for jets reconstructed in events with pileup taking into account clusters with a negative energy and using asymmetric cuts. For comparison, the jet response in QCD dijet events for jets reconstructed with the AntiKt algorithm with a radius parameter of 0.4 using H1-style calibration is shown in figure 5.17. The response for jets reconstructed with the AntiKt algorithm is observed to be smaller by several percent than the response for jets reconstructed with the Cone algorithm, but the shapes of the η distributions with symmetric and asymmetric cuts are similar to the shapes of the distributions for the Cone algorithm.

A significant positive bias is observed in figure 5.16 in the central detector region in the presence of pileup for jets reconstructed using the standard clustering procedure. The bias is absent in the distributions for jets reconstructed from clusters which are created using asymmetric cuts. The jet response with asymmetric clustering cuts in the presence of pileup is observed to be slightly smaller than the jet response for standard jets in events without pileup. The difference between the distributions with pileup and asymmetric cuts and without pileup increases with $|\eta|$. Such a difference in the jet response may be

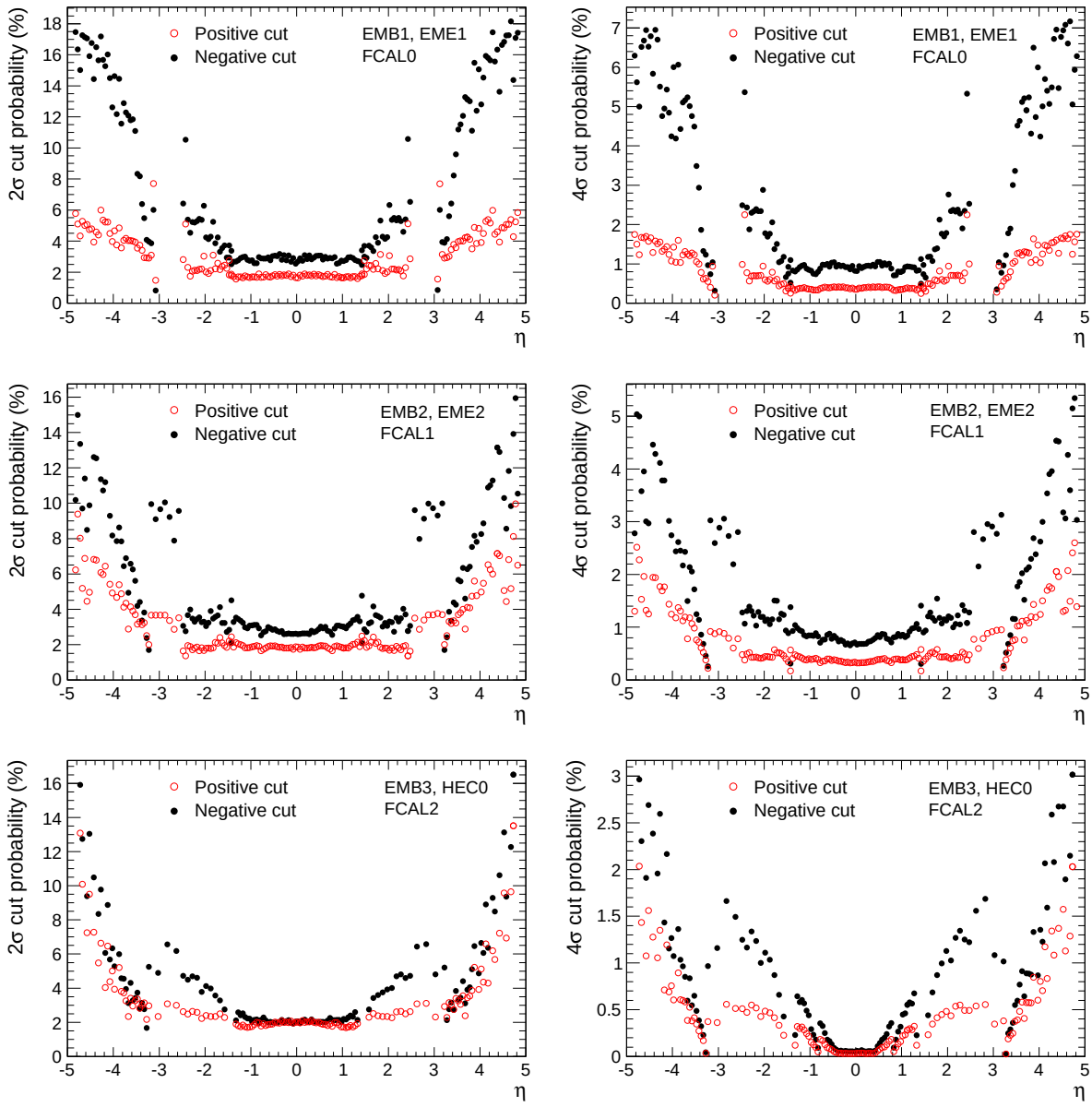

Figure 5.14: Probability for individual cells in a noise distribution including pileup noise to pass the asymmetric 2σ (*left*) and 4σ (*right*) cuts.

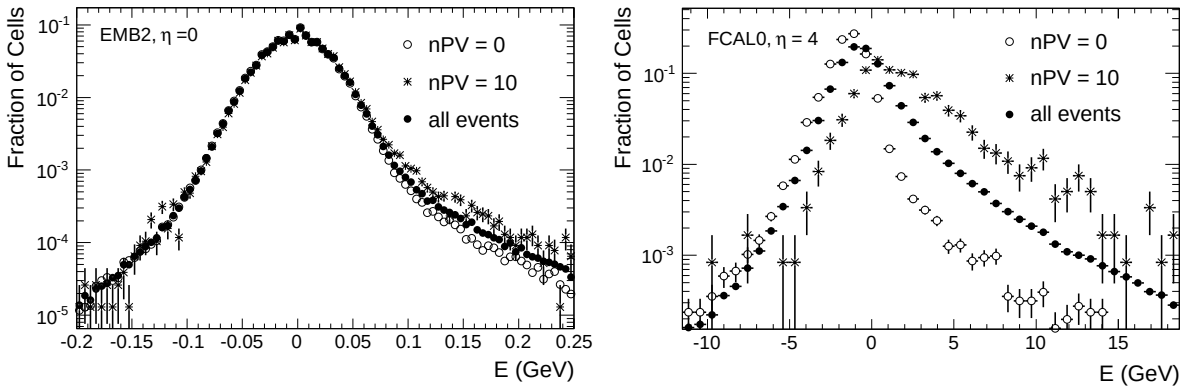

Figure 5.15: Cell energy in simulated minimum bias data in luminosity scenario I for two exemplary calorimeter layers and η bins. Distributions for all events and for events with a small and a large number of reconstructed primary vertices are shown to illustrate the effect of in-time pileup.

explained by the increase with $|\eta|$ of the noise RMS used to define the clustering cuts in the presence of pileup. Further studies would be needed to confirm this effect. The jet response in the forward calorimeter is not significantly affected by the change from symmetric to asymmetric cuts. For a bunch spacing of 75 ns a significant bias is observed in the forward region for standard jets in the presence of pileup. This bias is removed by the subtraction of the average cell energy before the cluster formation.

Figure 5.18 shows the resolution of the jet response in two bins of the transverse energy in QCD dijet events with pileup. The resolution is shown for jets reconstructed from clusters built with symmetric cuts and for jets reconstructed from clusters built with asymmetric cuts. For the case of symmetric cuts, distributions are shown for jets reconstructed using the standard procedure in which clusters with a negative energy are excluded. For the case of asymmetric cuts, clusters with a negative energy are included in the determination of the jet energy. For symmetric cuts, the resolution is observed not to be significantly affected by the inclusion of negative energy clusters in the determination of the jet energy. With asymmetric cuts, the resolution degrades by approximately 1.5% in the central detector region for jets with a transverse energy between 17 GeV and 35 GeV. Since the degradation is due to a constant contribution from noise its size decreases as the jet energy increases.

5.8 Summary and Conclusions

At non-vanishing luminosities the distributions of the calorimeter cell energies in randomly triggered events are asymmetric. The cell energies in randomly triggered events represent the total noise, including pileup noise, in the cells and the width of the distributions may be used to determine the cuts applied during the formation of topological clusters. During the standard cluster formation, symmetric cuts on the cell energy are applied which result in a bias on the cluster energy in calorimeter regions without significant signal energy deposits. In luminosity scenario I, an average energy in topological clusters in a cone in the η-ϕ plane with a radius of 0.4 of 2 GeV at the EM scale is observed in the central detector region. The average energy in topological clusters in a fixed cone is observed to be smaller in the forward region. It is shown that the bias can be reduced significantly by using asymmetric cuts during the cluster formation.

The positive average energy in topological clusters caused by the symmetric clustering cuts in signal-free calorimeter regions results in a corresponding bias of the jet response. The bias at the jet level is

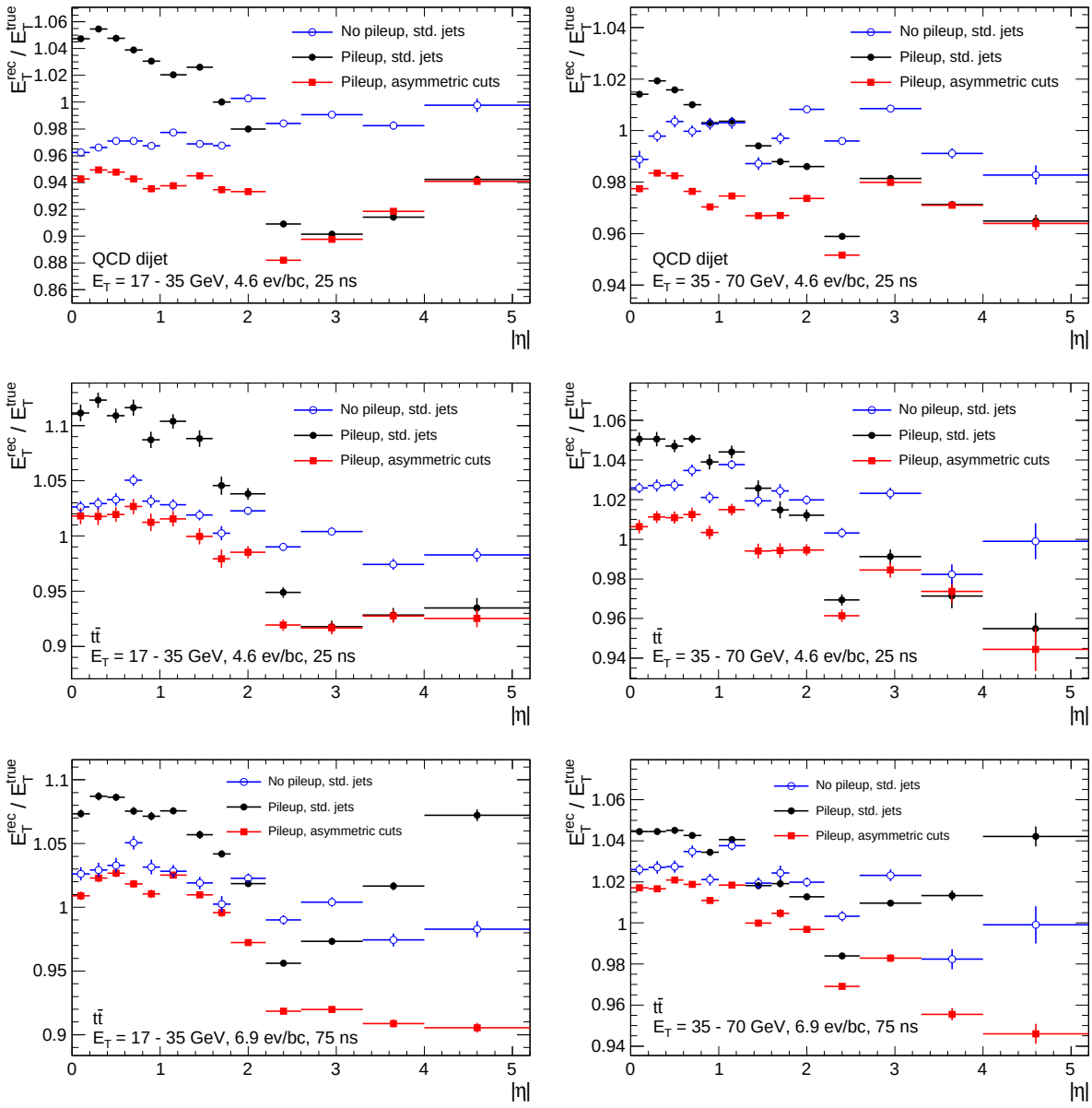

Figure 5.16: Jet response as a function of $|\eta|$ for cone jets with a radius of 0.4. The response is shown for jets reconstructed from clusters created with symmetric cuts and for jets reconstructed from clusters created with asymmetric cuts. Only for the case of asymmetric cuts clusters with a negative energy are included in the determination of the jet energy.

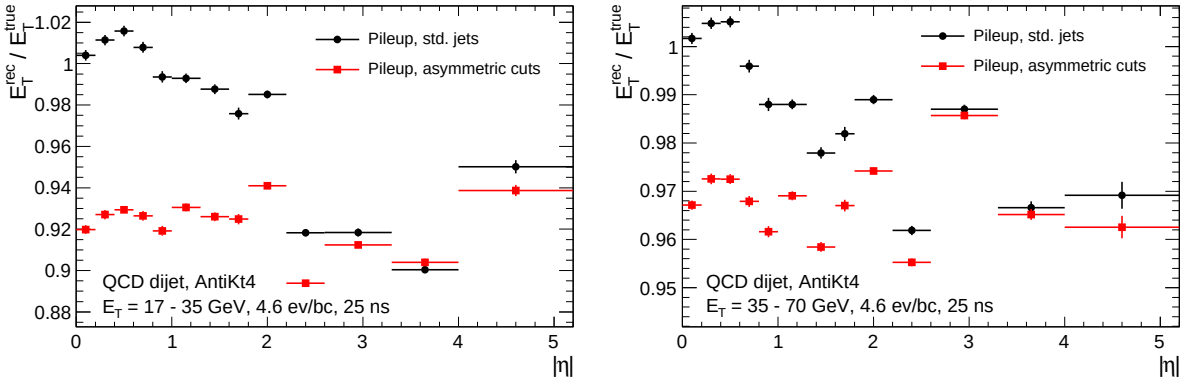

Figure 5.17: Jet response as a function of $|\eta|$ for AntiKt jets with a radius parameter of 0.4. The response is shown for jets reconstructed from clusters created with symmetric cuts and jets reconstructed from clusters created with asymmetric cuts. Only for the case of asymmetric cuts clusters with a negative energy are included in the determination of the jet energy.

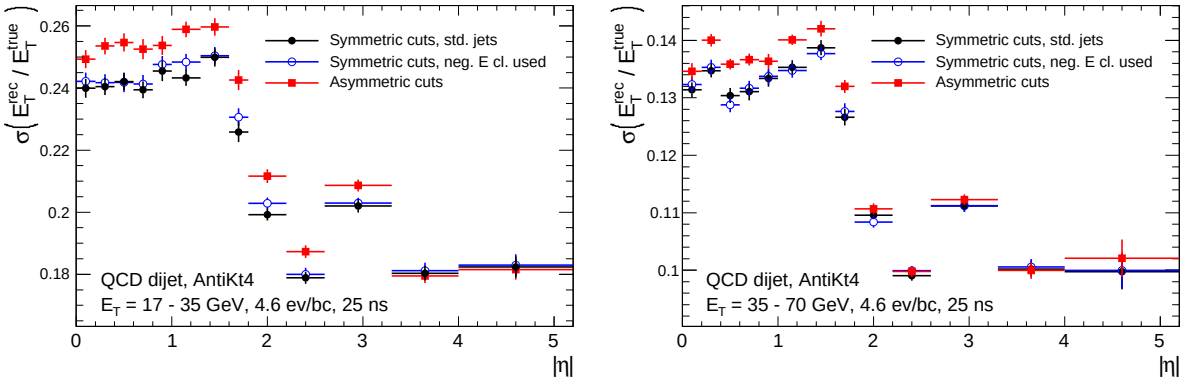

Figure 5.18: Resolution of the jet response as a function of $|\eta|$ for cone jets with a radius of 0.4. The resolution is determined as the σ of a Gaussian fitted to the central part of the jet response distribution. The resolution is shown for jets reconstructed from clusters built with symmetric cuts and for jets reconstructed from clusters built with asymmetric cuts. For the case of symmetric cuts distributions are shown for jets reconstructed using the standard procedure in which clusters with a negative energy are excluded and for jets reconstructed using a modified procedure in which clusters with a negative energy are included in the determination of the jet energy. For the case of asymmetric cuts clusters with a negative energy are included in the determination of the jet energy.

removed if asymmetric cuts are used during the cluster formation. At a bunch spacing of 75 ns an additional bias in the forward region is observed which originates from a non-zero average of the cell energies in that region due to an incomplete pileup cancellation from the bipolar LAr calorimeter pulse shapes. The bias is removed by subtracting the average cell energies before the cluster formation.

The cluster formation with asymmetric cuts is shown to result in larger average cluster multiplicities. An additional constant noise contribution to the resolution of the jet response is observed, resulting in a degradation of the resolution for jets with a transverse energy between 17 GeV and 35 GeV of approximately 1.5%.

The ratio of the positive cut to the negative cut is shown to depend weakly on the luminosity scenario. For an increase of the luminosity by a factor 2 a difference of the cut ratios of approximately 10% is observed. The difference between the ratios for different luminosity scenarios is observed to depend on $|\eta|$.

The method using asymmetric cuts during the cluster formation allows the determination of the jet energy in the presence of pileup without a bias from noise. The bias from noise that is observed if two-sided symmetric cuts or one-sided cuts are used during the cluster formation is expected to depend on the jet size and structure since only calorimeter regions without significant energy deposits are affected. By using asymmetric cuts, the bias is removed without knowledge of the jet size or structure. The method introduces an additional noise contribution to the jet energy resolution. For QCD dijets with a transverse energy between 17 and 35 GeV in luminosity scenario I, a bias of up to 2.7 GeV is removed while the jet transverse energy resolution degrades by approximately 0.3 GeV.

At the studied luminosities, the occupancy in the barrel calorimeter and most parts of the endcaps is sufficiently small to apply the method without modifications. In the forward calorimeter and some parts of the endcaps where the occupancy is larger, the method is still applicable, however it may be possible to improve the resolution by applying a cell energy correction depending on the amount of in-time pileup in a given event.

Chapter 6

Summary

The search for a Standard Model Higgs boson at small Higgs boson masses in the vector boson fusion channel with the decay $H \to \tau^+\tau^-$ is studied for the ATLAS experiment. Several ways to improve this search are found. In particular, some problems are identified which occur in the presence of pileup and improvements are developed.

The identification of hadronic τ lepton decays is improved by exploiting the significant average flight distance of τ leptons at the LHC. The large average flight distance leads to significant non-zero impact parameters of the decay products and a significantly displaced decay vertex. The performance of the reconstruction of the impact parameters and the transverse flight distance is studied in detail. The rejection of fake τ candidates can be increased by adding the impact parameter significance for 1-prong τ candidates and the transverse flight path significance for 3-prong τ candidates to the artificial neural network used by ATLAS for the τ identification. The rejection of 1-prong τ candidates from sources other than τ lepton decays in QCD dijet events is found to increase by more than 20% if the impact parameter significances are used. The rejection of fake 3-prong τ candidates in QCD dijet events is found to increase by more than a factor 2 if the transverse flight path significance is used.

The central jet veto applied in the search for a Standard Model Higgs boson at small Higgs boson masses in vector boson fusion is expected to be sensitive to the presence of pileup from minimum bias interactions. In a significant fraction of events, the additional proton-proton interactions produce dijets with sufficiently large transverse momenta to trigger the central jet veto. Additionally, the number of jets passing the transverse energy threshold for the central jet veto increases due to a degradation of the jet energy resolution in the presence of pileup and a positive bias of the jet energy caused by the current cluster formation method.

To reduce the effect of pileup on the central jet veto, a method is implemented that rejects jets not originating from the main proton-proton interaction. Tracks are used to link jets to the primary vertex. The fraction of the transverse momentum originating from the primary vertex is used as the discriminating observable. The same method is used at the D0 experiment and an alternate implementation exists in the ATLAS software. The implementation of the method for this study has led to an optimized track selection and a more efficient way to associate tracks with the primary vertex in the presence of pileup. Additionally, in the case of primary interactions with high-p_T leptons such as $H \to \tau^+\tau^- \to ll$ or $H \to \tau^+\tau^- \to lh$, the primary vertex is identified correctly in more than 99% of the events if the impact parameter of the leptons is exploited.

The use of jet-vertex association for the central jet veto is found to recover a large fraction of the efficiency for vector boson fusion signal events lost due to pileup jets. In a scenario with an average number of 4.6 interactions per bunch crossing at the nominal bunch spacing of 25 ns, the use of jet-vertex association leads to an improvement of the expected signal significance by 12% when considering the simplified case of a vector boson fusion signal with a purely $t\bar{t}$ background. In a luminosity scenario

with a larger track multiplicity and a smaller rate of jets caused by pileup for a bunch spacing of 75 ns, a recovery of the signal efficiency similar to the recovery in the scenario with a nominal bunch spacing is observed. Due to an increased rejection rate for jets from the main proton-proton interaction in $t\bar{t}$ events it is found preferable to modify the method in a way such that only jets with a transverse momentum from the primary vertex below a certain threshold are considered for rejection.

In the presence of pileup, the reconstructed energy of jets in the central region of the detector is observed to have a positive bias. In a luminosity scenario with an average number of 4.6 interactions per bunch crossing at a bunch spacing of 25 ns, a bias of approximately 2 GeV at the EM scale is observed. The bias is found to originate from the cell selection cuts applied during the cluster formation. The bias is significantly reduced by adjusting the cuts applied during the cluster formation in a way such that the average energy in individual cells after application of the cuts vanishes. The cluster multiplicity increases and an additional noise contribution to the jet energy resolution with a size of approximately 10% of the removed bias is introduced. The method using adjusted cuts in the cluster formation is independent of the jet algorithm, size and structure.

Appendix A

Average cell energy in simulated minimum bias data

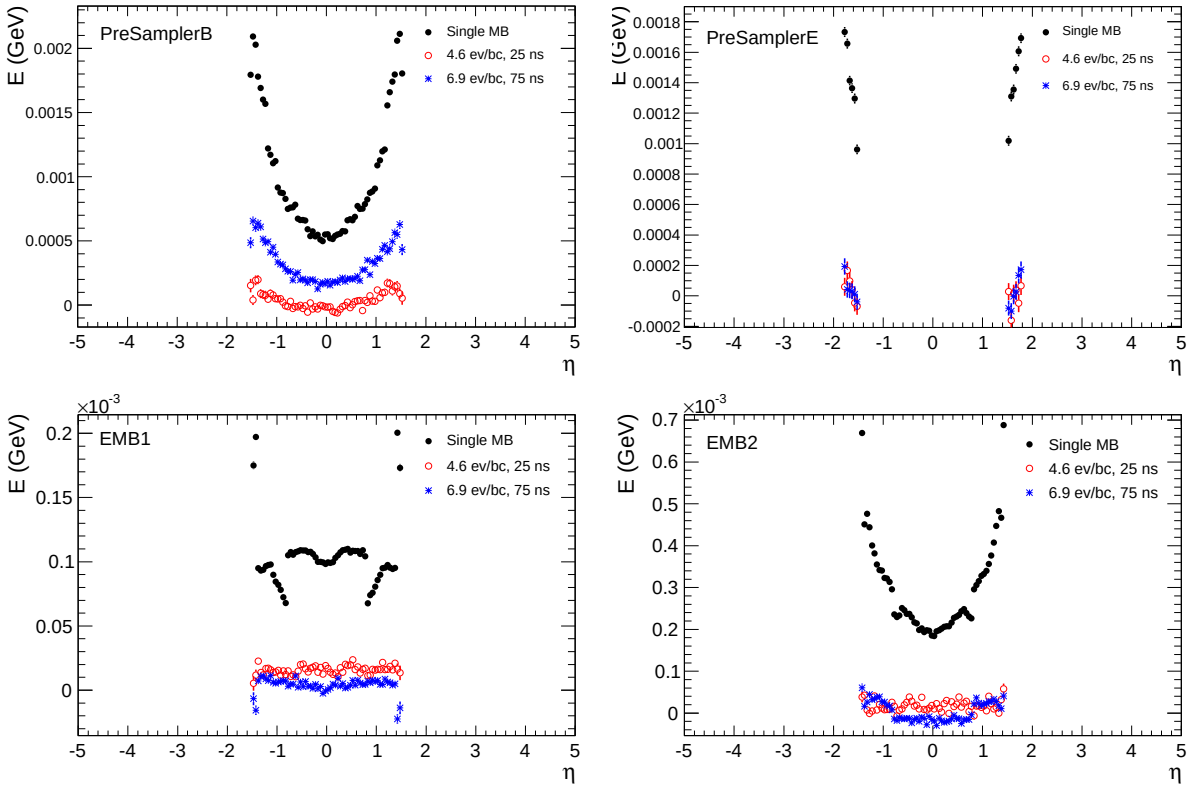

Figure A.1: Average cell energy in simulated minimum bias events with an average number of 4.6 events per bunch crossing at a bunch spacing of 25 ns (*red*) and 6.9 events per bunch crossing at a bunch spacing of 75 ns (*blue*) in different layers of the liquid argon calorimeter. For comparison the average energy in single minimum bias events (*black*) is shown.

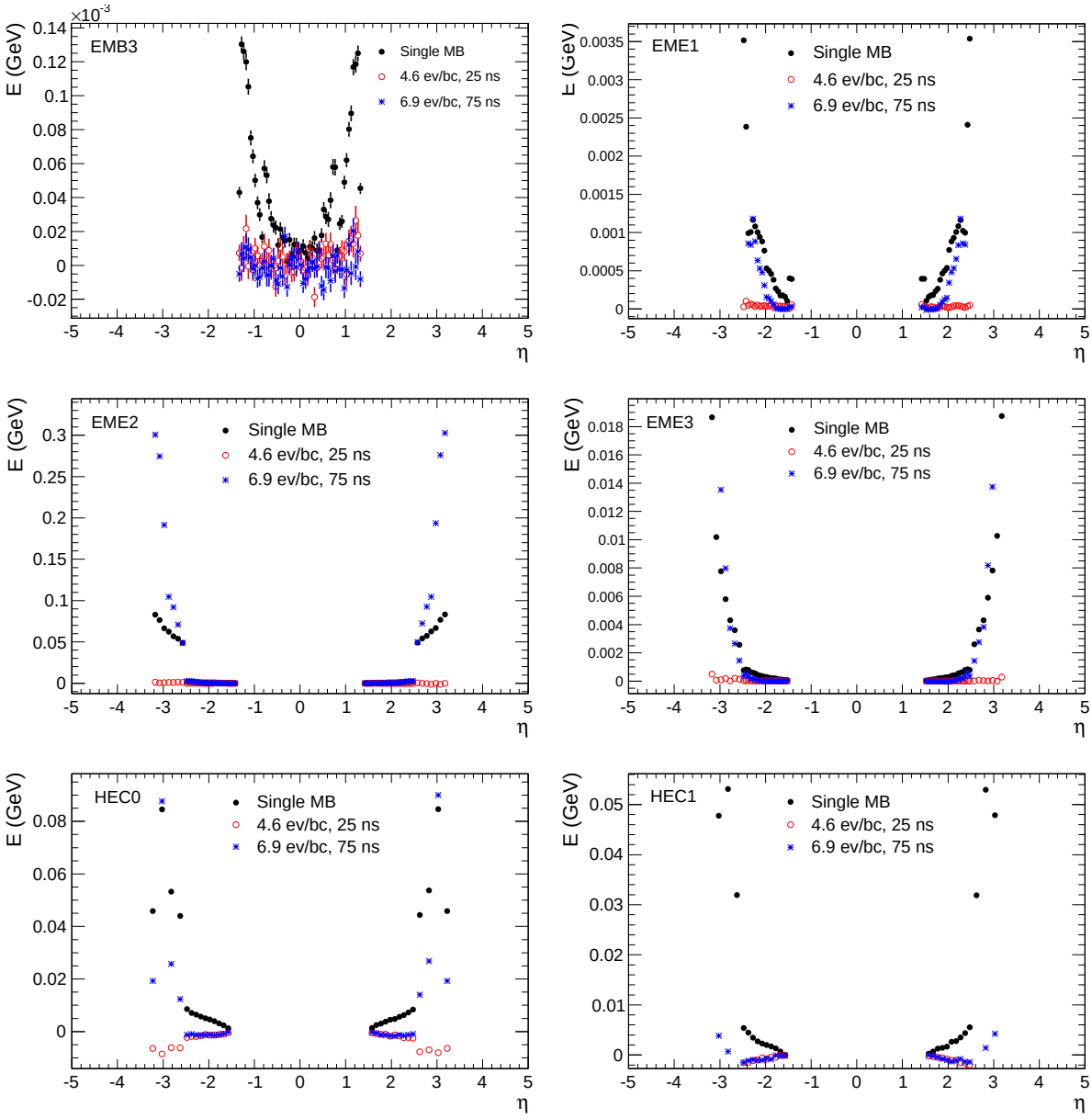

Figure A.2: Average cell energy in simulated minimum bias events with an average number of 4.6 events per bunch crossing at a bunch spacing of 25 ns (*red*) and 6.9 events per bunch crossing at a bunch spacing of 75 ns (*blue*) in different layers of the liquid argon calorimeter. For comparison the average energy in single minimum bias events (*black*) is shown.

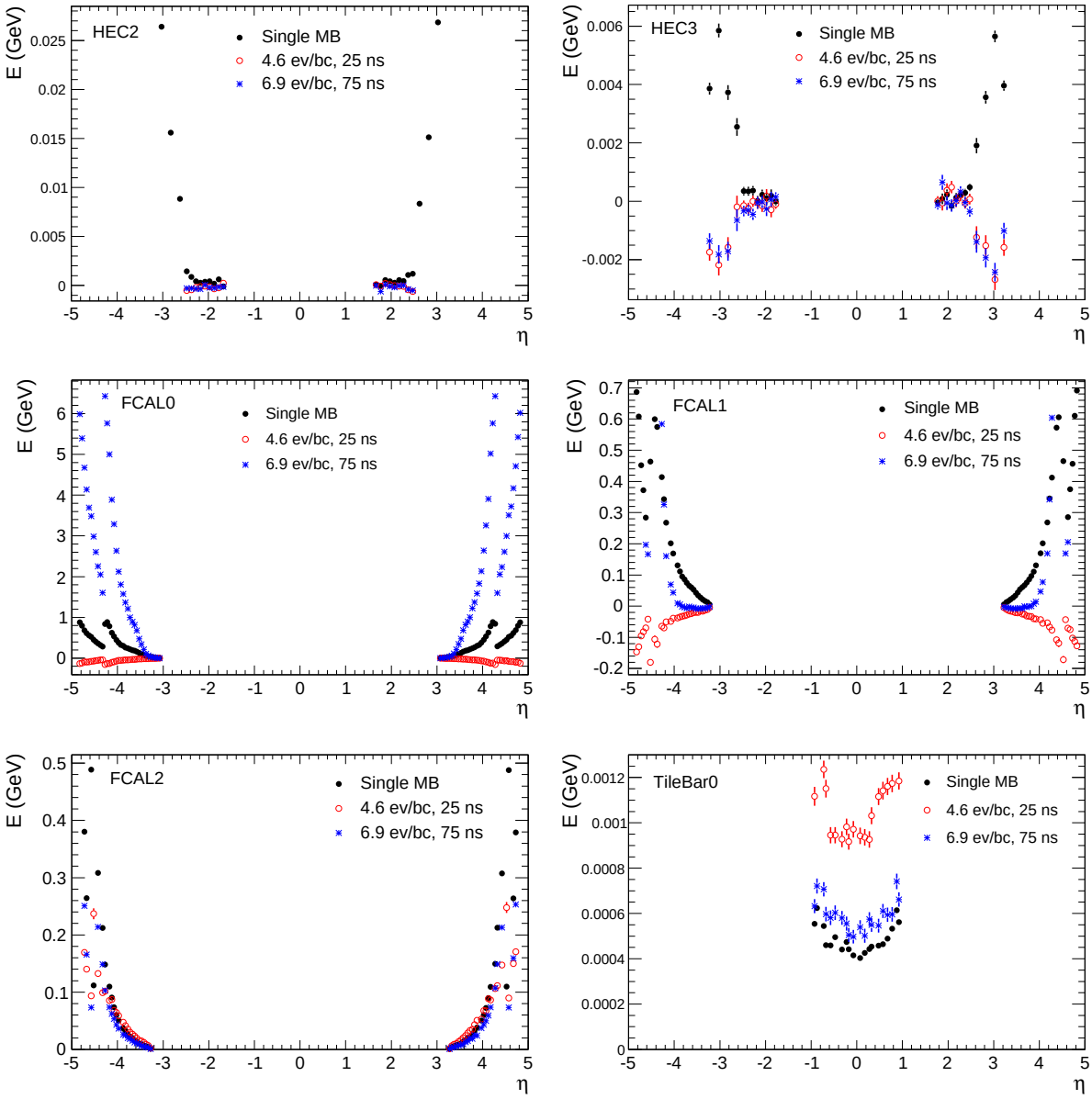

Figure A.3: Average cell energy in simulated minimum bias events with an average number of 4.6 events per bunch crossing at a bunch spacing of 25 ns (*red*) and 6.9 events per bunch crossing at a bunch spacing of 75 ns (*blue*) in different layers of the liquid argon calorimeter. For comparison the average energy in single minimum bias events (*black*) and distributions in the barrel section of the tile calorimeter are shown.

Appendix B

Average cell energy with two-sided symmetric cuts

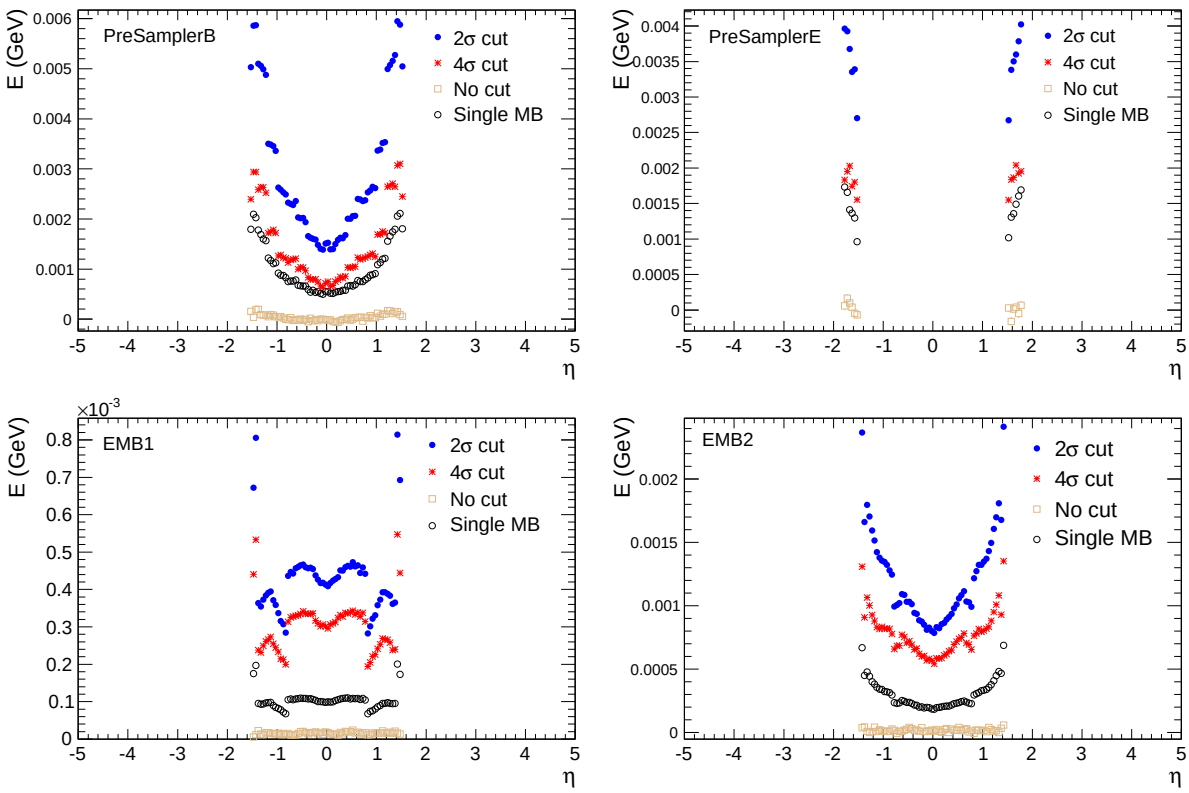

Figure B.1: Average cell energy in simulated minimum bias events with an average number of 4.6 events per bunch crossing at a bunch spacing of 25 ns (*red*) after the application of two-sided symmetric 2σ and 4σ cuts. Distributions without cuts and for single minimum bias events are shown for comparison.

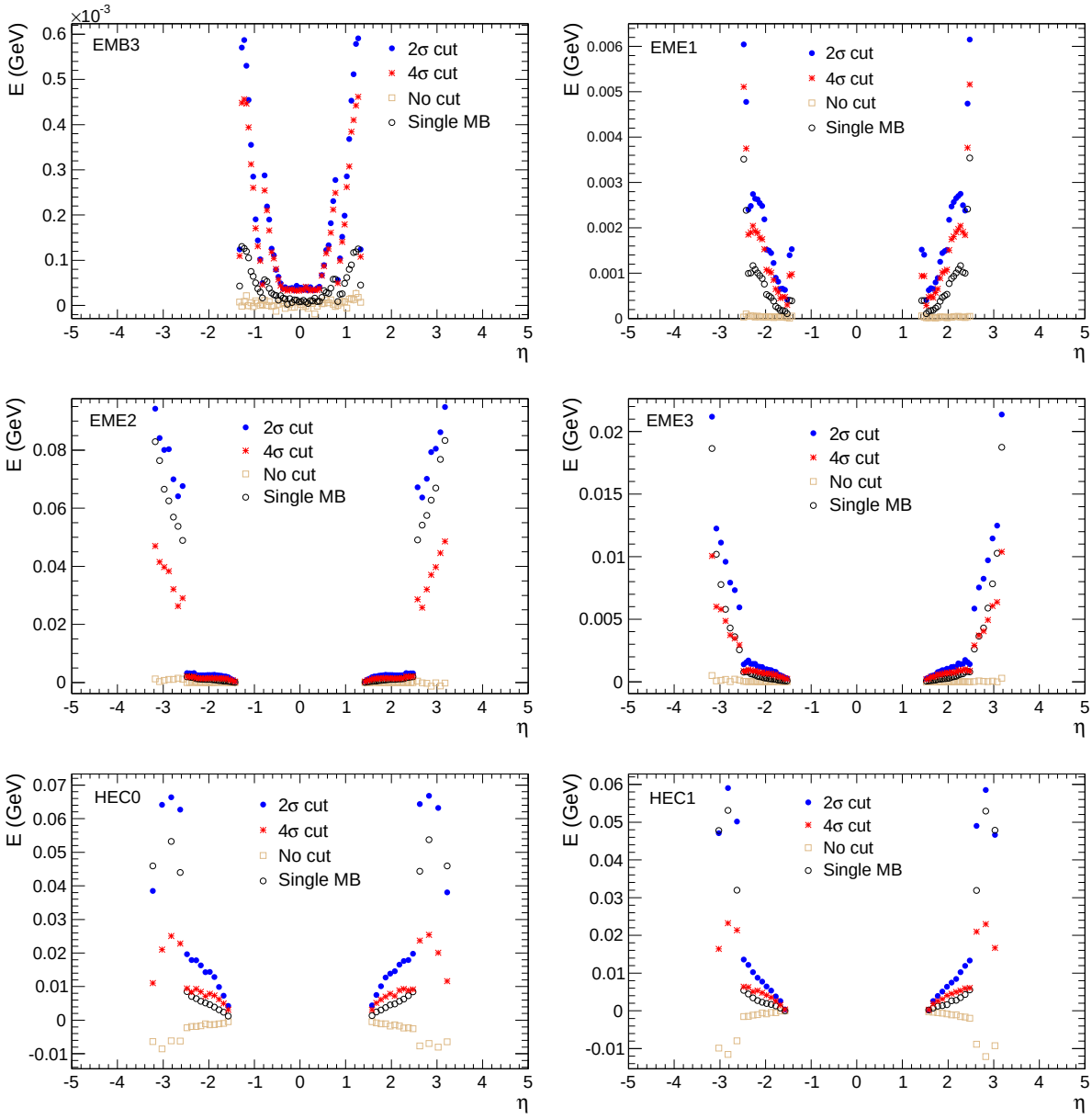

Figure B.2: Average cell energy in simulated minimum bias events with an average number of 4.6 events per bunch crossing at a bunch spacing of 25 ns (*red*) after the application of two-sided symmetric 2σ and 4σ cuts. Distributions without cuts and for single minimum bias events are shown for comparison.

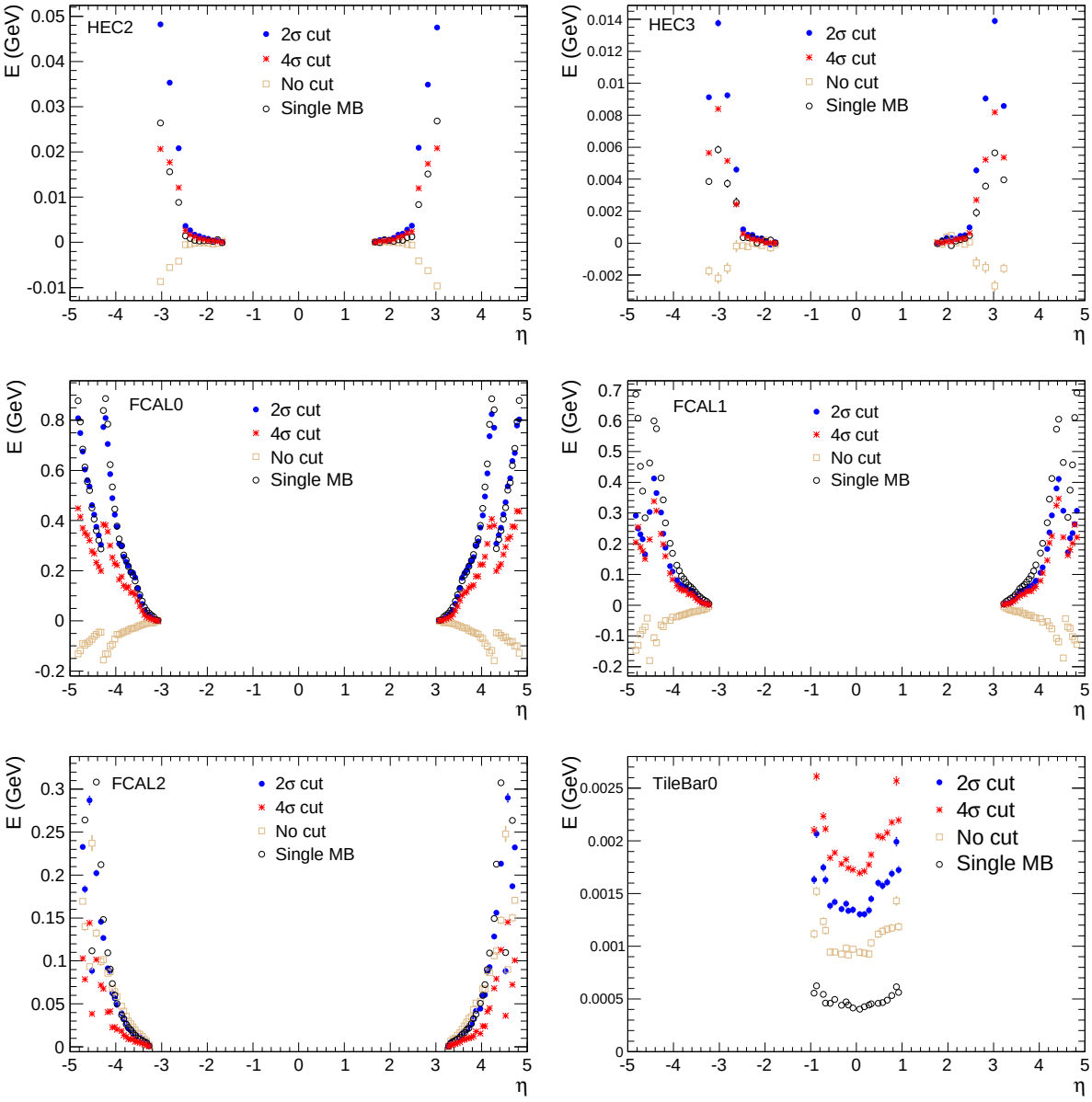

Figure B.3: Average cell energy in simulated minimum bias events with an average number of 4.6 events per bunch crossing at a bunch spacing of 25 ns (*red*) after the application of two-sided symmetric 2σ and 4σ cuts. Distributions without cuts and for single minimum bias events are shown for comparison.

Bibliography

[1] S. Asai *et al*, *Prospects for the search for a standard model Higgs boson in ATLAS using vector boson fusion*, Eur. Phys. J. C **32** (2003) 19–54.

[2] The ATLAS Collaboration, *Expected Performance of the ATLAS Experiment : Detector, Trigger and Physics*, CERN-OPEN-2008-020 (2008) .

[3] D.J. Griffiths, *Introduction to Elementary Particles*. John Wiley & Sons, 1987.

[4] M.E. Peskin, D.V. Schroeder, *An Introduction to Quantum Field Theory*. Westview Press, 1995.

[5] S.L. Glashow, *Partial Symmetries of Weak Interactions*, Nucl. Phys. **22** (1961) no. 4, 579–588.

[6] S. Weinberg, *A Model of Leptons*, Phys. Rev. Lett. **19** (1967) no. 21, 1264–1266.

[7] A. Salam in *Elementary particle theory: Relativistic Groups and Analyticity (Nobel Symposium No. 8)*, N. Svartholm, ed., p. 367. Almqvist and Wiksell, Stockholm, 1968.

[8] The ALEPH Collaboration *et al.*, *Precision Electroweak Measurements and Constraints on the Standard Model*, CERN-PH-EP/2009-023 (2009) .
{`http://lepewwg.web.cern.ch/LEPEWWG/`}.

[9] The TEVNPH Working Group, *Combined CDF and D0 Upper Limits on Standard Model Higgs-Boson Production with 2.1 - 5.4 fb^{-1} of Data*, FERMILAB-CONF-09-557-E (2009) .

[10] M. Spira, P.M. Zerwas, *Electroweak Symmetry Breaking and Higgs Physics*, Lect. Notes Phys. **512** (1998) 161–225.

[11] The ATLAS Collaboration, G. Aad *et al*, *ATLAS Sensitivity to the Standard Model Higgs in the HW and HZ Channels at High Transverse Momenta*, ATL-PHYS-PUB-2009-088 (2009) .

[12] *LHC Design Report*, CERN-2004-003-V-1 (2004) .

[13] The ATLAS Collaboration, G. Aad *et al*, *The ATLAS Experiment at the CERN Large Hadron Collider*, JINST **3** (2008) S08003.

[14] The CMS Collaboration, S. Chatrchyan *et al*, *The CMS experiment at the CERN LHC*, JINST **3** (2008) S08004.

[15] The ATLAS Inner Detector Community, *ATLAS inner detector : Technical Design Report, 2*, CERN-LHCC-97-017, ATLAS-TDR-005 (1997) .

[16] T. Cornelissen *et al*, *Concepts, Design and Implementation of the ATLAS New Tracking (NEWT)*, ATL-SOFT-PUB-2007-007 (2007) .

[17] D. Froidevaux, V.A. Mitsou, *Experimental prospects at the Large Hadron Collider*, J. Phys. Conf. Ser. **171** (2009) 012021.

[18] The ATLAS Muon Collaboration, *ATLAS muon spectrometer : Technical Design Report*, CERN-LHCC-97-022, ATLAS-TDR-010 (1997) .

[19] K. Hagiwara, D. Rainwater, D. Zeppenfeld, *Searching for $H \to \tau\tau$ in weak boson fusion at the CERN LHC*, Phys. Rev. D **59** (1998) 014037.

[20] C. Amsler *et al* (Particle Data Group), *Review of Particle Physics*, Phys. Lett. B **667** (2008) no. 1 and 2009 partial update for the 2010 edition. {`http://pdg.lbl.gov`}.

[21] H. Ma, F.E. Paige, S. Rajagopalan, *τ Reconstruction in Athena*, 2002. {`http://atlasinfo.cern.ch/Atlas/GROUPS/PHYSICS/JETS/TAUREC/taurec.ps.gz`}.

[22] E. Richter-Was, H. Przysiezniak, F. Tarrade, *Exploring hadronic τ identification with DC1 data samples: a track based approach*, ATL-PHYS-2004-030 (2004) .

[23] M. Heldmann, D. Cavalli, *An improved tau-Identification for the ATLAS experiment*, ATL-PHYS-PUB-2006-008 (2006) .

[24] T. Cornelissen *et al*, *Updates of the ATLAS Tracking Event Data Model*, ATL-SOFT-PUB-2007-003 (2007) .

[25] G. Piacquadio, K. Prokofiev, A. Wildauer, *Primary Vertex Reconstruction in the ATLAS Experiment at LHC*, J. Phys. Conf. Ser. **119** (2008) 032033.

[26] R. Frühwirth, W. Waltenberger, *Adaptive Multi-vertex fitting*, in *Computing in High Energy Physics and Nuclear Physics 2004 - CHEP 04*, CERN-2005-002 (2005) 280–282.

[27] A. Wildauer, *Primary Vertex Finding, b-Tagging and Analysis of the Channel $\mathrm{t\bar{t}H^0}$, $\mathrm{H^0 \to b\bar{b}}$ in the ATLAS Experiment*. PhD thesis, Leopold-Franzens-Universität Innsbruck, 2006.

[28] P. Billoir, R. Frühwirth, M. Regler, *Track element merging strategy and vertex fitting in complex modular detectors*, Nucl. Instr. and Meth. A **241** (1985) 115–131.

[29] R. Frühwirth, *Application of Kalman filtering to track and vertex fitting*, Nucl. Instr. and Meth. A **262** (1987) 444–450.

[30] P. Billoir, S. Qian, *Fast vertex fitting with a local parametrization of tracks*, Nucl. Instr. and Meth. A **311** (1992) 139–150.

[31] A. Zell, N. Mache, T. Sommer, and T. Korb, *The SNNS Neural Network Simulator*, in *GWAI*, T. Christaller, ed., vol. 285 of *Informatik-Fachberichte*, pp. 254–263. Springer, 1991.

[32] M. Wolter, T. Szymocha, *Comparison of multivariate methods in identification of hadronic decays of tau leptons*, ATL-PHYS-PUB-2006-012 (2006) .

[33] R.N. Cahn, S.D. Ellis, R. Kleiss, W.J. Stirling, *Transverse Momentum Signatures for Heavy Higgs Bosons*, Phys. Rev. D **35** (1987) 1626–1632.

[34] Yu.L. Dokshitzer, S.I. Troian, V.A. Khoze, *Collective QCD effects in the structure of final multi-hadron states*, Sov. J. Nucl. Phys. **46** (1987) 712–719.

[35] The ATLAS Collaboration, *ATLAS detector and physics performance : Technical Design Report, 2*, CERN-LHCC-99-015, ATLAS-TDR-015 (1999) .

[36] G. Corcella *et al*, *HERWIG 6: an event generator for hadron emission reactions with interfering gluons (including supersymmetric processes)*, JHEP **01** (2001) 010.

[37] M.L. Mangano *et al*, *ALPGEN, a generator for hard multiparton processes in hadronic collisions*, JHEP **07** (2003) 001.

[38] M.L. Mangano. {`http://mlm.home.cern.ch/mlm/talks/lund-alpgen.pdf`}.

[39] S. Jadach, Z. Was, R. Decker, J.H. Kuehn, *The tau decay library TAUOLA: version 2.4*, Comp. Phys. Commun. **76** (1993) 361.

[40] E. Barberio, Z. Was, *PHOTOS-A universal Monte Carlo for QED radiative corrections: version 2.0*, Comp. Phys. Commun. **79** (1994) 291.

[41] J.M. Butterworth, J.R. Forshaw, M.H. Seymour, *Multiparton interactions in photoproduction at HERA*, Z. Phys. C **72** (1996) 637–646.

[42] S. Agostinelli *et al*, *GEANT4 - a simulation toolkit*, Nucl. Instr. and Meth. A **506** (2003) 250–303.

[43] S. Frixione, B.R. Webber, *Matching NLO QCD computations and parton shower simulations*, JHEP **06** (2002) 029.

[44] T. Sjöstrand, S. Mrenna, P. Skands, PYTHIA *6.4 Physics and Manual*, JHEP **05** (2006) 026.

[45] W. Lampl *et al*, *Calorimeter Clustering Algorithms: Description and Performance*, ATL-LARG-PUB-2008-002 (2008) .

[46] G.P. Salam, G. Soyez, *A practical seedless infrared-safe cone jet algorithm*, JHEP **05** (2007) 086.

[47] M. Cacciari, G.P. Salam, *The anti-k_T jet clustering algorithm*, JHEP **04** (2008) 063.

[48] The ATLAS LARG Unit, *ATLAS liquid-argon calorimeter : Technical Design Report*, CERN-LHCC-96-041 (1996) .

[49] The ATLAS / Tile Calorimeter Collaboration, *ATLAS tile calorimeter : Technical Design Report*, CERN-LHCC-96-042 (1996) .

[50] T. Barillari *et al*, *Local Hadronic Calibration*, ATL-LARG-PUB-2009-001 (2008) .

[51] The ATLAS Cross-Section Task Force, S. Asai *et al*, *Cross-sections for Standard Model processes for the ATLAS CSC studies*, ATL-PHYS-INT-2009-003 (2009) .

[52] M. Honda *et al*, *Inelastic cross section for p-air collisions from air shower experiments and total cross section for p-p collisions up to* $\sqrt{s} = 24$ TeV, Phys. Rev. Lett. **70** (1993) no. 5, 525–528.

[53] The TOTEM Collaboration, V.Avati *et al*, *TOTEM Technical Design Report*, CERN-LHCC-2004-002 (2004) .

[54] The COMPETE Collaboration, J.R. Cudell *et al*, *Benchmarks for the Forward Observables at RHIC, the Tevatron-Run II, and the LHC*, Phys. Rev. Lett. **89** (2002) no. 20, 201801.

[55] R. Engel, J. Ranft, *Hadronic photon-photon interactions at high energies*, Phys. Rev. D **54** (1996) no. 7, 4244–4262.

[56] ATLAS wiki, https://twiki.cern.ch/twiki/bin/view/Atlas/PileupDigitization?rev=47, https://twiki.cern.ch/twiki/bin/view/Atlas/PileUpTimingResponses?rev=14 .

[57] D.W. Miller, A. Schwartzman, D. Su, *Jet-Vertex Association Algorithm*, ATL-COM-PHYS-2008-008 (2008) .

[58] W.E. Cleland, E.G. Stern, *Signal processing considerations for liquid ionization calorimeters in a high rate environment*, Nucl. Instr. and Meth. A **338** (1994) 467–497.

[59] W. Lampl *et al*, *Digitization of LAr calorimeter for CSC simulations*, ATL-LARG-PUB-2007-011 (2007) .

[60] P. Adragna *et al*, *Testbeam Studies of Production Modules of the ATLAS Tile Calorimeter*, ATL-TILECAL-PUB-2009-002 (2009) .

[61] K.S. Cranmer, *Searching for new physics: Contributions to LEP and the LHC*. PhD thesis, University of Wisconsin, Madison, 2005.

[62] D. Schouten, M. Vetterli, *In Situ Jet Calibration and the Effects of Pileup in ATLAS*, ATL-PHYS-INT-2007-011 (2007) .